INTERFACE AND ENERGY EFFICIENCY OF PHOTOVOLTAICS

INTERFACE AND ENERGY EFFICIENCY OF ORGANIC PHOTOVOLTAICS

By CINDY XINXIN ZHAO, B. ENG., M. A. SC.

A Thesis

Submitted to the School of Graduate Studies

in Partial Fulfillment of the Requirements

for the Degree

Doctor of Philosophy

McMaster University

Doctor of Philosophy (2013)	McMaster University
(Materials Science and Engineering)	Hamilton, Ontario

TITLE:	Interface and Energy Efficiency of Organic Photovoltaics
AUTHOR:	Cindy Xinxin Zhao, B. Eng. (Zhejiang University) M. A. Sc. (McMaster University)
SUPERVISOR:	Professor Gu Xu
NUMBER OF PAGES:	xvii, 135

PREFACE

THIS THESIS IS ORGANIZED IN A 'SANDWICH' STYLE BASED ON THE FOLLOWING PUBLICATIONS AS OF AUGUST 2013.

Paper 1

C. X. Zhao, X. Wang, W. Zeng, Z. K. Chen, B. S. Ong, K. Wang, L. Deng, and G. Xu, Organic photovoltaic power conversion efficiency improved by AC electric field alignment during fabrication, Appl. Phys. Lett. **99**, 053305 (2011).

Printed under license #3134270999969

Paper 2

C. X. Zhao, K. Wang, J. F. Britten, M. Zhi, X. Wang, Z. K. Chen, and G. Xu, Dual nanostructures in poly (3-hexylthiophene) based organic photovoltaics under alternative current electric field, Thin Solid Films **520**, 5770 (2012).

Printed under license #3134270523916

Paper 3

C. X. Zhao, L. L. Deng, M. Y. Ma, J. R. Kish, and G. Xu, Multiple-interface tracking of degradation process in organic photovoltaics, submitted for publication.

Paper 4

C. X. Zhao, L. L. Deng, and G. Xu, Space charge and dipoles in bilayer and bulk heterojunctions of organic photovoltaics, submitted for publication.

As the first author of the above publications, I analyzed the scientific/engineering problems, designed my own experiments, fabricated devices via solution process and vacuum deposition, carried out experimental measurements, interpreted experimental data, and wrote my research manuscripts. In all the cases, my supervisor Prof. G. Xu provided insightful suggestions and invaluable help, during the experimental setups, data analysis, and manuscript modification.

ABSTRACT

As a promising new technology, organic photovoltaics (OPVs) have been widely studied recently. To improve the device efficiency for commercial use of 10%, a number of attempts have been made in my research. The ultra-low frequency AC field was first employed, to align p/n polymers during fabrication. The resulting devices showed 15% increase in device efficiency, attributed to the optimized morphology and enlarged p/n interface. During the improvement process, dual nanostructures of the polymers were found, the highly oriented layer and the randomly distributed part, which provided a better understanding of the OPVs under the AC field alignment.

The OPV stability was then studied by impedance measurements, to track multi-interface degradation without breaking the device. It was found the degradation of p/n junction was attributed to the deteriorated morphology and oxidized polymers, whereas the semiconductor/metal interface changed by producing metal oxides as degradation products.

The dramatic contrast between the bilayer and bulk heterojunctions (BHJ) was at last investigated by capacitance measurements in vacuum. The existing models of the BHJs had difficulty explaining the higher overall capacitance, compared with that from the bilayer devices. The resulting puzzling charge density was clarified by separating the measured capacitance into two parallel components, one from the space charge of the proposed Schottky junction, and the other from the dark dipoles presumably formed spontaneously across the donor/acceptor interface.

ACKNOWLEDGEMENT

I am deeply grateful to my supervisor, Prof. Gu Xu, for continual and unwavering encouragement and guidance that made my work in this thesis possible. Thank you so much for offering me such a unique research opportunity, with a perfect combination of freedom and directions. You are trying your best to teach me everything you know, and make me a qualified independent researcher. Much appreciated your time and effort.

I would like to thank our collaborators, Dr. Beng Ong, Dr. Zhi-Kuan Chen, Dr. Xizu Wang, and Dr. Wenjin Zeng, from Institute of Materials Research and Engineering, Singapore, for invaluable discussion and insightful comments. I also wish to express my thanks to my supervisory committee members, Prof. Adrian Kitai and Prof. Joey Kish, for their constructive advices and inspiring discussion.

I really appreciate timely help and support from all the group members, Lulu Deng, Kewei Wang, Yiqun Ma, Han Yan, Sean Chen and Alice Mao. And also, I want to give my thankfulness to the technicians and staff members, Jim, Doug, Ed, Xiaogang, Diana, Nanci, and Jane, for their technical support and suggestions.

I am also indebted to my roommates, Lulu and Guozhen, for their friendship and encouragement all the time.

Last but not least, I would like to thank my dear parents in China, for encouraging me, and understanding any choice I made. Your influence can be found on every single page of this thesis, and I miss you so much.

CONTENTS

LIST OF FIGURES

LIST OF TABLES

Chapter 1. INTRODUCTION

1.1 SOLAR ENERGY AND PHOTOVOLTAICS

The ever-increasing worldwide use of fossil fuels is one of the most profitable yet injurious phenomena in modern society. The combustion of hydrocarbons, such as coal, oil and natural gas, upon which the world depends mostly for our energy demands, was adopted centuries before its capacity and environmental costs had been recognized. These reserves are limited in supply and will one day be depleted, since the natural formation processes took millions of years. As the largest contributor to the release of greenhouse gases, burning fossil fuels emits carbon monoxide, carbon dioxide and even nitrogen oxide, causing the poor air quality of many urban areas, intensifying the threat of global warming. Therefore, a major strategic shift is necessary, to develop other energy sources which are clean, efficient, and renewable.

As a most promising alternative, solar energy is as old as can be, which has long been harnessed for lighting and home heating since ancient times. Advanced technologies invented after industrial revolution, provide various means of solar energy utilization, including solar heating, solar thermal electricity, solar architecture, artificial photosynthesis and solar photovoltaics, which are hopeful to contribute to the most urgent energy crisis we are facing.

Considering the incoming solar radiation received on the ground, it is on the order of 10^3 Wm^{-2}, equivalent to $1.7*10^{17}$ W for the Earth's surface, which is approximately 10,000 times the global power consumption. In other words, the current energy needs can be fully met by covering 0.1% of the surface with photovoltaic panels of 10% efficiency. According to the data released on December 11, 2012, solar thermal and photovoltaics supplied a small portion of the US's energy, about 0.16 % of total energy (97.722 quadrillion Btu) and 2 % of renewable energy consumption (8.090 quadrillion Btu) [1]. Although contributing relatively little in total renewable energy consumption, solar energy use shows the highest growth rate among all the renewable sources. In Europe, solar photovoltaic electricity covers on a yearly basis close to 10% of the electricity demand; and the figure is expected to reach 25% in 2030 [2].

The photovoltaic is a timely technology that meets the environmental criteria, and indeed advances beyond fossil fuel combustion. Photovoltaics, also known as solar cells, can be referred to any devices which convert light energy directly/indirectly into electrical energy. According to quantum mechanics, light is a collection of light quanta, referred to photons, whose energy can only be determined by the frequency or the wavelength of the light. The hypothesis of light quanta was first proposed by Einstein dating back to 1905, in order to provide the explanation to the famous photoelectric effect as shown in **Figure 1.1a**, where the ultraviolet light liberates electrons from the surface of a metal. After absorbing the energy of photons, the electrons are able to jump from the ground state to a higher energy excited state within the material; however, the excited electrons normally return to a lower energy excited state or the ground state in a short time, with the energy emission in the form of photons or phonons. On the other hand, these excited electrons can be pulled away and fed to an external circuit before they relax. In a photovoltaic device (**Figure 1.1b**), there is some spatial asymmetry, such as dissimilar materials with different electronic properties, which generates a built-in electric field along the contact. The excited electrons are driven by this built-in field and forced into the external electrical load where their excess energy can be utilized to do electrical work.

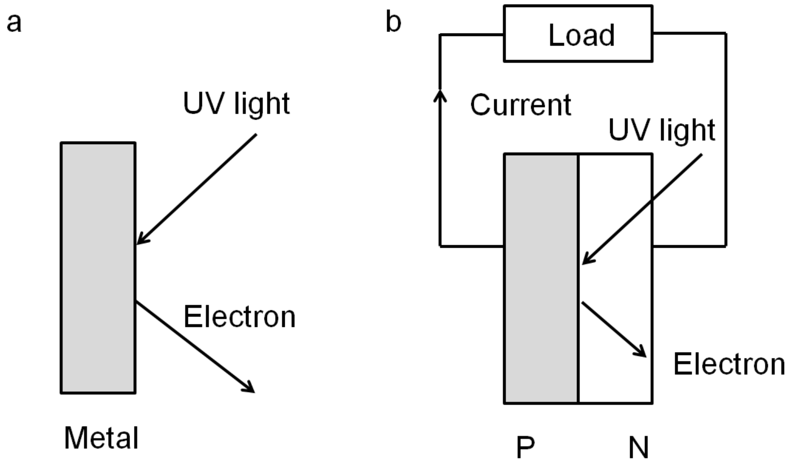

Figure 1.1 Comparison between the photoelectric effect (a) and photovoltaic effect (b).

1.2 BRIEF HISTORY OF PHOTOVOLTAICS

Photovoltaics, also known as solar cells, can be referred to any devices which convert light into electricity. The photovoltaic effect was first observed in 1839 by Alexandre-Edmond Becquerel in a liquid phase electrochemical cell, where an electric current was produced when light was shone on the silver coated platinum (Pt) electrode [3]. The first solid state photovoltaic device was reported by William Adams and Richard Day in 1876, when they discovered a photocurrent in a selenium (Se) sample with two Pt contacts [4]. This photovoltaic device of Pt/Se/Pt involved a rectifying junction between Se and Pt contact. Later, in 1894, Charles Fritts replaced the Pt metal contacts by gold and another metal, in order to fabricate large area devices. It is quite interesting that all of the early photovoltaics relied on the Schottky junction formed between the semiconductor and semitransparent metal; however, there was no supporting theory until 1930s, when Walter Schottky, and Neville Mott suggested a barrier should exist at the metal-semiconductor junction [5].

It is universally known that the electronic properties of semiconductors are extremely sensitive to impurity and crystallographic structure of materials, which limit their applications in the new solid state electronics. With the development of high quality silicon in the 1950s, it became easier to fabricate p/n junctions in silicon, and of course, silicon electronics. It was found that the p/n junction based devices showed better rectifying and photovoltaic behavior than Schottky junctions. The first silicon p/n junction photovoltaic was developed at Bell Laboratories by Daryl M. Chapin, Calvin S.

Fuller and Gerald. L. Pearson in 1954, with the power conversion efficiency of 6%, 10 times larger than selenium Schottky junction cells [6]. Since then, the paradigm of photovoltaics has begun to shift towards the p/n junction based devices, and the single p/n junction mono or polycrystalline silicon cells were referred as the first generation photovoltaics.

Also in the 1950s and 60s, more semiconducting materials were initially studied, for p/n junction photovoltaics with higher efficiencies, e.g., cadmium sulphide (CdS), gallium arsenide (GaAs), indium phosphide (InP), and cadmium teleride (CdTe). However, silicon remained the primary photovoltaic material, due to the many advantages it can provide in the microelectronics industry.

1970s can be regarded as the ‘golden age’ for photovoltaics, when these oil-dependent countries, driven by the energy crisis, started to seek alternative energy sources, and fund for research and projects in energy related areas. Photovoltaics fell right into the category, and became a focal point of research interest. The methodologies for photovoltaic manufacturing were largely developed during these days (**Figure 1.2** [7]). Low cost devices, known as the second generation photovoltaics, were created with moderately high efficiencies, based mainly on amorphous silicon, CdS/CdTe, copper indium gallium selenide (CIGS) and other thin film materials. The understanding of the science of photovoltaics can also be traced back to this period.

It was not until the 1990s, with a considerable drop of the production cost, that photovoltaics began to be embedded into the commercial applications and accepted as

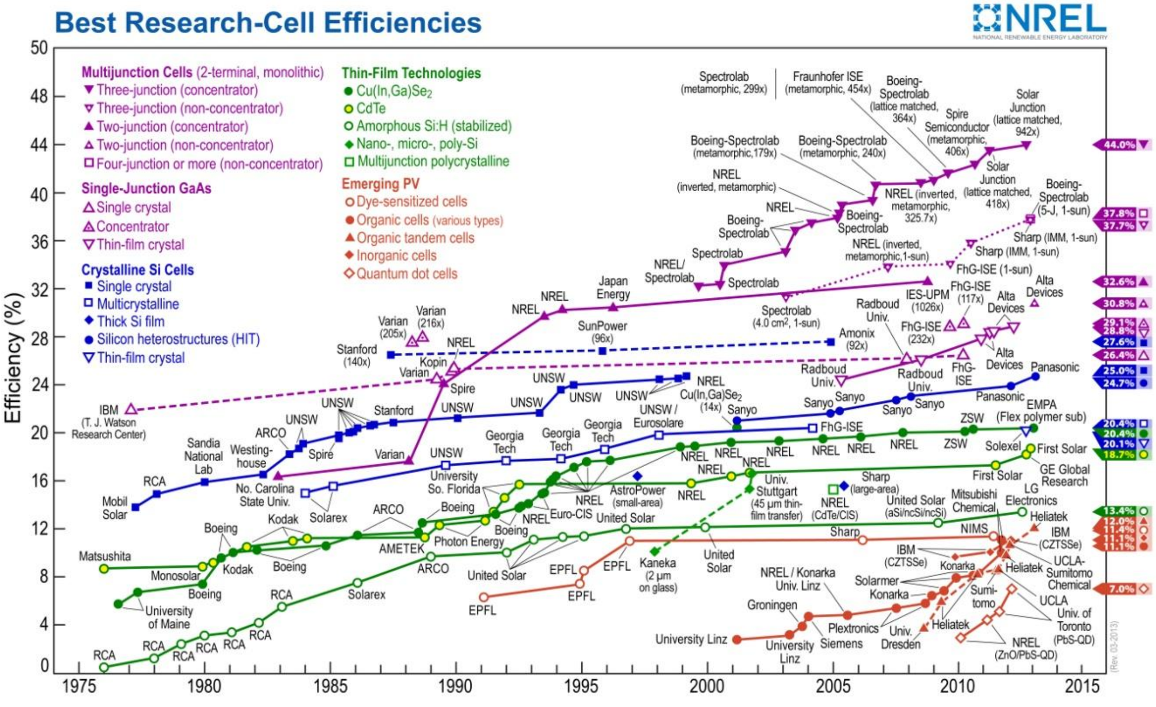

Figure 1.2 Best research-cell efficiencies recorded by the National Renewable Energy Laboratory, showing the methodology development since 1975 [7].

products for individual sale. Photovoltaics became more economic, especially in the areas where conventional electricity supply was expensive. Nowadays, the cost of power generation by photovoltaics is about 1 dollar per watt, hundred times lower than that of its first applications in space. The power conversion efficiency of silicon photovoltaics in lab is approaching the theoretical limit of 29% [8]; and that of the commercialized one has also reached 16%-19% [9]. New strategies and designs have been further explored, in order to overcome the Shockley-Queisser limit, including multi-layer tandem cells, organic photovoltaics, and quantum dot solar cells. These third generation photovoltaics contain a wide range of potential solar innovations, proposing new directions for more efficient devices with lower areal cost.

1.3 DEVELOPMENT OF ORGANIC PHOTOVOLTAICS

Organic photovoltaics, made from carbon-based organic semiconductors, have been widely studied in the last decade, due to so many advantages they can provide. Compared with the inorganic counterparts, organic semiconductors show high light absorption coefficients, and moderate charge transport properties even in an amorphous form with a higher degree of disorder. These organic semiconductors are either thermally evaporated at lower temperature, or solution processed at room temperature, making the manufacturing procedures easier and cheaper. The idea of fabricating photovoltaics on the portable thin plastic substrates by roll to roll printing becomes so attractive for high-volume production, driven by the demands for future displays and electronic devices.

Similar to inorganic devices, organic photovoltaics have a photoactive layer sandwiched by two electrodes. The device architectures have been developed from the single layer, the bilayer heterojunction, to the bulk heterojunction (BHJ), as shown in **Figure 1.3**. Generally, the efficient photoactive layer consists of two semiconducting materials with distinct electronic properties, the electron donor and electron acceptor, in order to separate the photogenerated excitons. According to the classification of organic molecules, organic photovoltaics have been divided into two main groups, polymer photovoltaics and small molecule photovoltaics. Therefore, two concepts have been developed based on the nature of materials: either soluble blends of p type conjugated polymers with n type fullerene derivatives, which allow for low-cost and large-area solution processing; or the combination of small molecular donors and acceptors, which can be thermally evaporated at relative low temperatures in a vacuum chamber. As a kind of hybrid devices, dye-sensitized solar cells are sometimes included in organic photovoltaics, due largely to the organic dye molecules involved in the device configuration.

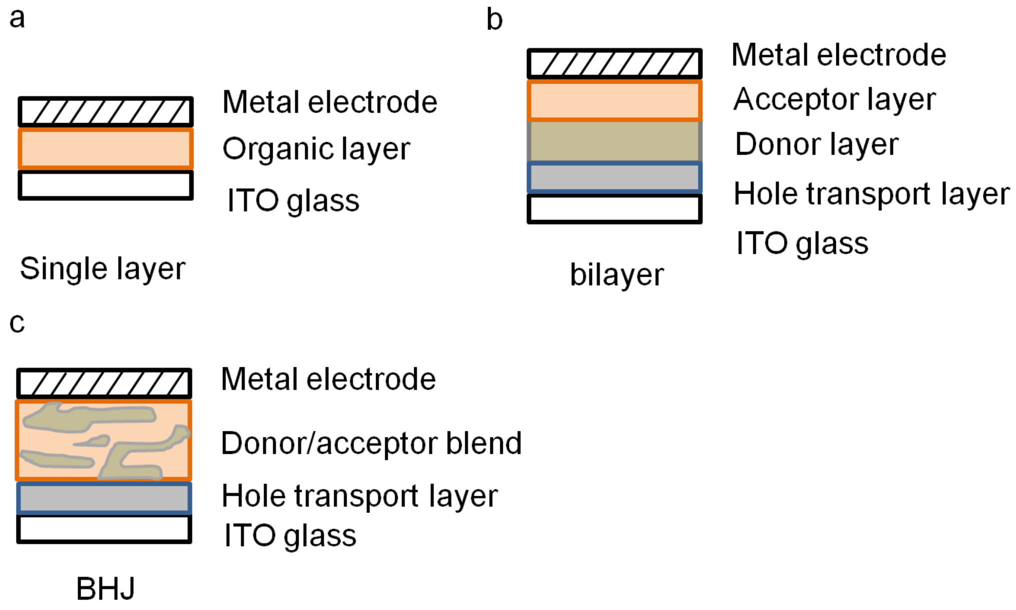

Figure 1.3 The development of device architectures from the single layer (a), the bilayer heterojunction (b), to the bulk heterojunction (c).

1.3.1 Polymer Photovoltaics

Inherently, organic polymers with carbon backbones are insulators which can be used as encapsulating materials, such as the coatings for cables and wires. The resistivity has been found to be reduced when polymers are mixed with carbon black or metal to make a composite. However, the conduction in the composite takes place via the carbon black and metal instead of the polymer, which only acts as a supporting matrix. In 1977, the first major breakthrough was obtained, when polyacetylene (**Figure 1.4**), a very poor conductor in its pure state, turned into a highly conductive polymer by reacting with iodine [10]. The resulting conductivity showed an increase of over 10^{10}, and the conduction was explained to be caused by the movement of electrons through the polymer itself. For the discovery and development of conducting polymers, Hideki Shirakawa, Alan G. MacDiarmid and Alan J. Heeger won the Nobel Prize for Chemistry in 2000.

Other polymers with similar characteristics, usually involve polyconjugated structures, which are insulators in the original forms but when treated with an oxidizing or a reducing agent can be convert into polymer salts with electrical conductivities comparable to metals. It is found that the conductivity in polymers is due to conjugation, the alternation of single and double bonds between the carbon atoms [11]. The band gap of polymers with fully saturated chains, such as polyethylene (**Figure 1.4**) is about 5 eV, and decreases to about 1.5 eV in the conjugated system polyacetylene. The ground state of a carbon atom is in the $1s^2 2s^2 2p^2$ configuration. In organic semiconductors, the *s* and *p* orbitals form 3 sp^2 orbitals, the σ bonds. The fourth orbital, p_z, perpendicular to the plane determined by the sp^2 orbitals, is referred as the π bond. In a polyconjugated system the π orbitals are assumed to overlap, leading to delocalization of the electrons, which is the origin of the conductivity in these polymers.

The first polymer solar cells were made by pure conjugated polymers, with power conversion efficiencies of 0.001 to 0.01% [12]. In 1992, the discovery of photoninduced charge transfer in composites of conjugated polymers and fullerene (C_{60}, **Figure 1.4**) or its derivatives, provided an effective approach to high efficiency photovoltaic conversion [13]. The observation of highly increased photoconductivities upon C_{60} addition to conjugated polymers, led to the development of polymer-fullerene bilayer heterojunction [14] and BHJ devices [15]. The concept of BHJ was introduced by mixing two polymers having donor and acceptor properties in solution. In order to fabricate BHJ devices by printing or spin-coating, C_{60} derivatives with enhanced solubility have been employed to prepare the polymer blend in a proper weight ratio. The prepared BHJ was represented in the ideal case as a bicontinuous network of donor and acceptor phases, thereby maximizing the interfacial area between the donors and acceptors.

From then on, the polymer photovoltaic development gained momentum. A significant progress has been made on the improvement of the power conversion efficiency of polymer BHJ devices, and the achieved efficiencies have evolved from less than 1% in the poly(phenylene vinylene) (PPV, **Figure 1.4**) system in the 1990s [14], to 3–5% in the poly(3-hexylthiphene) (P3HT, **Figure 1.4**) and [6,6]-phenyl-C_{61}-butyric acid methyl ester ($PC_{61}BM$, **Figure 1.4**) system in 2005 [16]. In 2009, Alan Heeger and his

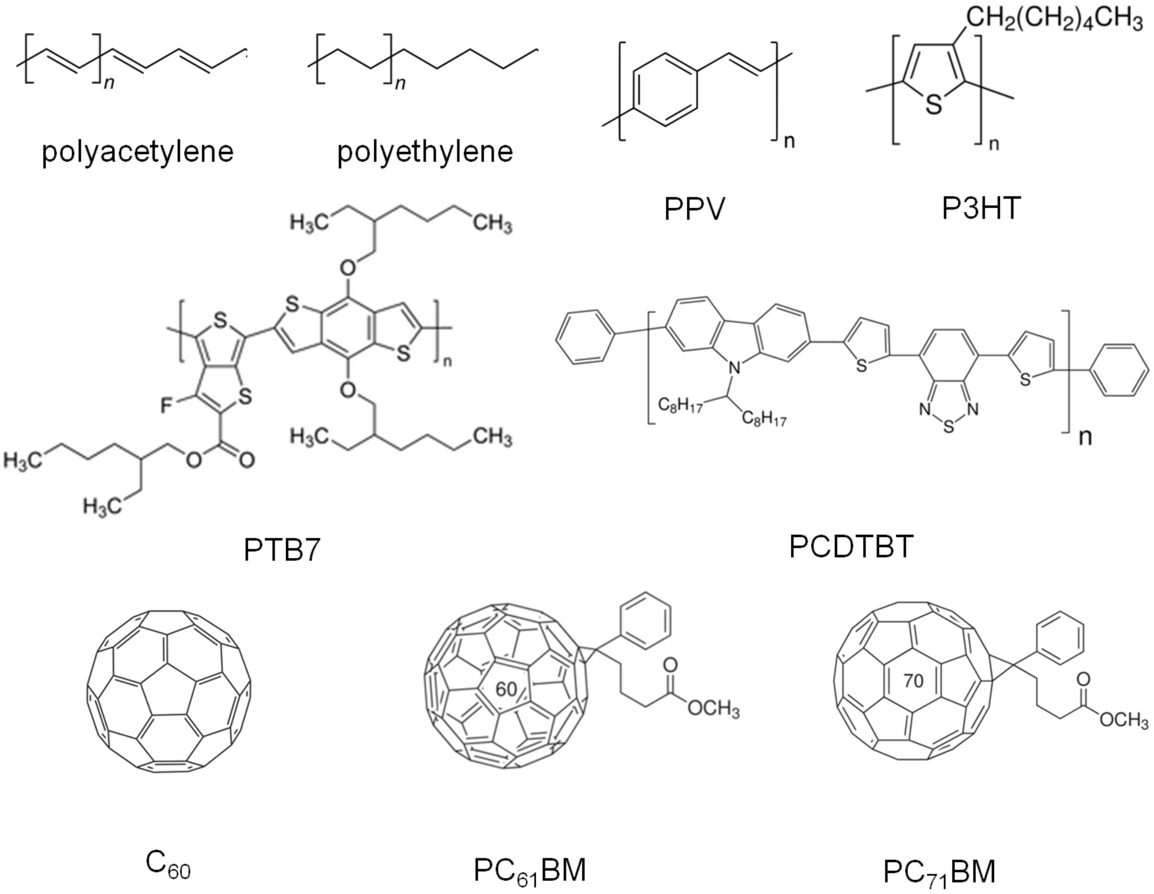

Figure 1.4 Several conjugated polymers and organic molecules well applied in polymer photovoltaics.

co-works reported the BHJ cells with internal quantum efficiency close to 100%, based on poly[N-9''-hepta-decanyl-2,7-carbazole-alt-5,5-(4',7'-di-2-thienyl-2',1',3'-benzothiadiazole) (PCDTBT, **Figure 1.4**) and [6,6]-phenyl-C_{71}-butyric acid methyl ester ($PC_{71}BM$, **Figure 1.4**) [17]. The first polymer photovoltaic with efficiency approaching double digits was prepared using poly[[4,8-bis[(2-ethylhexyl)oxy]benzo[1,2-b:4,5-b']dithiophene-2,6-diyl][3-fluoro-2-[(2-ethylhexyl)carbonyl]thieno[3,4-b]thiophenediyl]] (PTB7, **Figure 1.4**), invented by Luping Yu and co-workers in 2010 [18].

1.3.2 Small Molecule Photovoltaics

The story of small molecule photovoltaics started with the discovery of dark conductivity in halogen doped organic compounds in the mid 1950s [19], followed by the development of the charge transport properties of small molecules [20]. The first small molecule photovoltaics were reported in 1975 and 1976, based on a photoactive layer made of a single material, i.e., chlorophyll-a (**Figure 1.5**) as well as its metallic complexes [21]. Two dissimilar electrodes with different work functions were essential to provide the built-in electric field upon which the photovoltaic properties strongly relied. The power conversion efficiencies of the single layer cells were less than 0.01%, and their fill factor usually poor, attributed to both a larger series resistance associated with the insulating nature of organic material used, and the field-dependent charge generation process.

Great progress was made in 1986, when C. W. Tang fabricated a double layer heterojunction cell of 0.95% power conversion efficiency from copper phthalocyanine

(CuPc, **Figure 1.5**) and a perylene tetracarboxylic derivative (PV, **Figure 1.5**) [22]. Different from the single layer cells, the interface between these two thin organic layers is responsible for charge photogeneration; and the electrodes only provide ohmic contacts to the organic layers. Light is absorbed in the donor material, the hole conducting small molecule such as CuPc. The photogenerated electron-hole pairs, known as excitons, diffuse in the donor domains towards the interface to the acceptor, which is specially chosen to be more electronegative. The difference in energy levels of donor and acceptor provides energy for exciton separation. As a result, the electron can go to a lower energy state in the acceptor, whereas the hole remains in the donor molecules. The separated electrons and holes eventually hop towards the respective contacts, and generate a photocurrent.

Despite the novel idea of organic heterojunction, the bilayer configuration is still limited by the thicker photoactive layer, compared with the exciton diffusion length of about 10 nm in most of small molecules and polymers. Stephen R. Forrest and his co-workers prepared a tandem cell using silver layer as charge recombination centers in between two separated heterojunction cells, showing a more than doubled efficiency of 2.5% [23]. On the basis of the same donor, the group obtained an even higher efficiency of about 3.6%, using C_{60} as acceptor and 2,9-dimethyl-4,7-diphenyl-1,10-phenanthroline (BCP, **Figure 1.5**) as an exciton blocking layer [24]. In 2005, they mixed CuPc and C_{60} into a 1:1 blend, and introduced the mixed layer in between pure CuPc and C_{60} layers by co-evaporation. The power conversion efficiency of the resulting cell was increased to 5%, and this device has been regarded as the first BHJ in small molecule photovoltaics

[25]. In the following years, the conversion efficiency for solar energy has been improved steadily, due to the synthesis of new chemicals. In January, 2013, Heliatek GmbH, a world leading organic photovoltaic company, announced a record breaking 12.0% cell efficiency based on its patented small molecules [26].

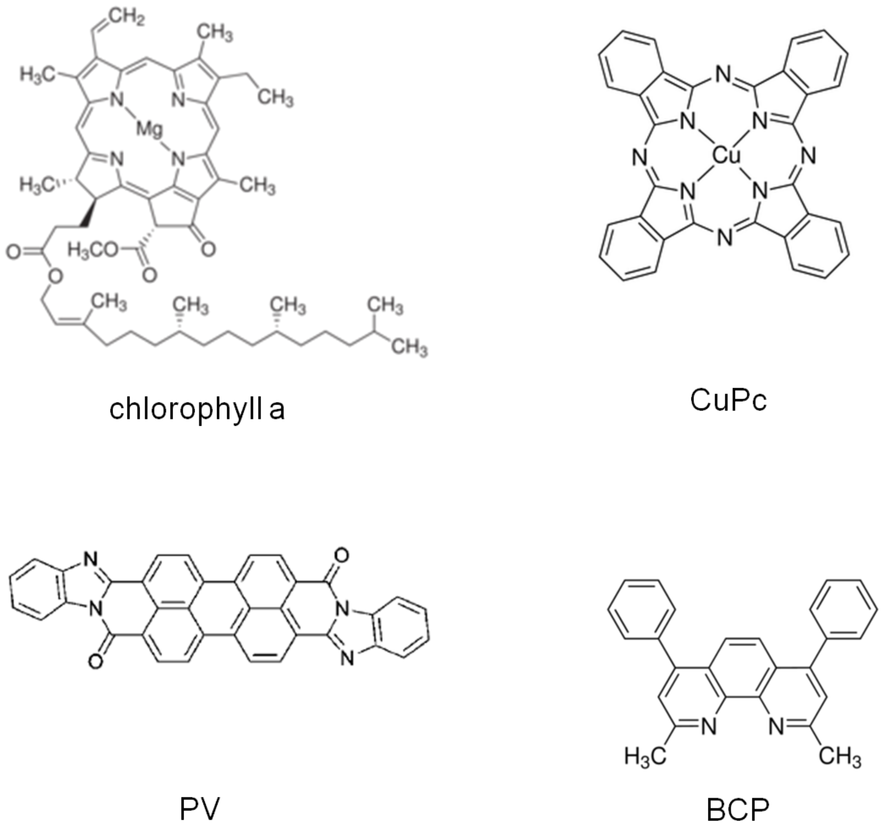
chlorophyll a

CuPc

PV

BCP

Figure 1.5 Some organic molecules commonly used in small molecule photovoltaics.

1.3.3 Dye-sensitized Solar Cells

Dye-sensitized solar cell (DSSC), also called the Grätzel's cell, is based on a porous semiconductor with a large band gap, to which a monolayer of dye molecules are attached by covalent bonding. DSSCs are good for their high conversion efficiencies, excellent stability, and easy fabrication processes in ambient air. The phrase 'dye-sensitized' indicates that the photons are mainly harvested by the loaded dye molecules on the surface of metal oxide thin film. It was first invented in 1988 by Brian O'Regan and Michael Grätzel, and later published with the power conversion efficiency of 7% in Nature in 1991 [27].

A typical DSSC consists of a photo-sensitized anode, a redox mediator, and a counter electrode as shown in **Figure 1.6**. There is an electrochemical junction at this semiconductor/electrolyte interface assisting the charge separation process. When light comes into the cell from the left side, passes through the transparent conducting glass, and finally reaches the porous metal oxide photo-sensitized anode. Photons with enough energy are absorbed by the dye molecules, exciting them into the excited states. These excited dye molecules will inject electrons into the conduction band of metal oxide, and become oxidized. Electrons move through the porous metal oxide layer and arrive at the transparent conducting glass working as the electrode. Meanwhile, the redox couples acts as a mediator which transfers negative charges from the counter electrode to oxidized dye molecules, and reduce them back to their original states. This provides the complete electron flow inside the DSSC. The theoretical maximum open circuit voltage of DSSC is determined by the difference of Fermi level between metal oxide and redox couple.

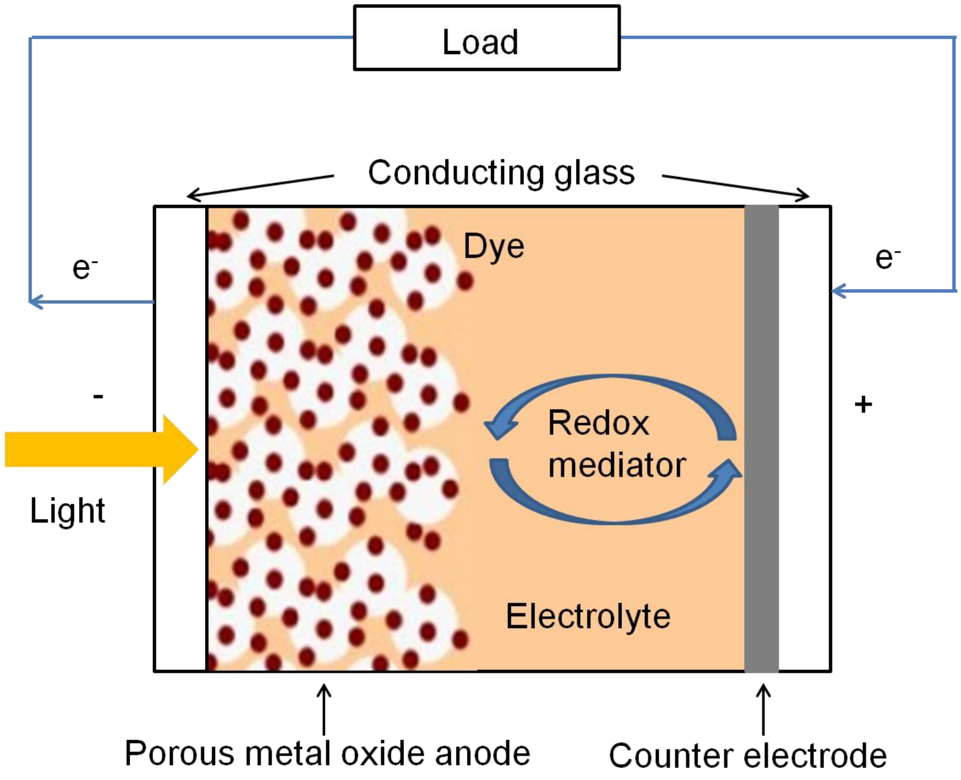

Figure 1.6 Typical structure of a dye-sensitized solar cell.

Within two decades, numerous attempts have been made to replace the parts of original Grätzel's cell, with various materials in the purpose of improving the device performance. The research and development focuses mainly on the wide band gap metal oxides, new dye molecules with broader absorption spectra and rapid charge injection rates, and new mediator which can be chemically and thermally stable at elevated temperature under illumination. So far, the power conversion efficiency of liquid state DSSC has been improved to exceed 12 %, with a custom synthesized donor-π bridge-acceptor dye molecule and cobalt (II/III)-based redox electrolyte [28]. Despite offering relatively high conversion efficiencies for solar energy, conventional DSSCs suffer from durability problems resulting from their use of organic liquid electrolytes, such as electrode corrosion and electrolyte leakage. Solid state DSSC has thus been demonstrated, with either inorganic or organic hole conductors, showing a power conversion efficiency up to 10.2% [29].

1.3.4 Future Applications

Compared with the silicon photovoltaics manufactured in vacuum chambers and well controlled clean rooms, organic photovoltaics are able to be processed in factories without special facilities, and high speed roll to roll printing which allows for large volume production. It becomes more attractive when the bulky and heavy cells can be got rid of, since organic photoactive layers can be printed directly on flexible plastic substrates without further protection from breakage. These plastic devices will be light-weight, portable, and able to generate clean energy from the sun, driving the cost of electricity production down to 12-15 cents/kWh and much less than 1 dollar per Watt.

Due to these unique characteristics, organic photovoltaics are being developed and combined into consumer applications. There is a huge potential market, such as solar-powered chargers for personal electronics and outdoor equipment. In 2009, G24i power announced the first commercial shipment of DSSC to Hong Kong based consumer electronics bag manufacturer (**Figure 1.7 a**) [30]. A conceptual lamp has been produced by Sony, in a form of a lantern powered by DSSC. The electricity is saved during the day, and later illuminates the lantern, projecting floral patterns on the floor in the night (**Figure 1.7 b**) [31]. Colorful and charming design, customizable shapes and sizes are just a few selling points of organic photovoltaic integrated products. Samsung came up with a bright idea of employing organic photovoltaics in building structures such as windows, skylights, roofs and walls (**Figure 1.7 c**) [32]. Buildings equipped with plastic solar panels may soon be available and affordable in the housing market.

1.4 REMAINING CHALLENGES OF ORGANIC PHOTOVOLTAICS

As a promising new technology, organic photovoltaics have been intensively studied for their peak and long-term device performance. Despite the development, a considerable gap still exists, compared with silicon solar cells with average efficiencies of 15% and lifespan of 20 years.

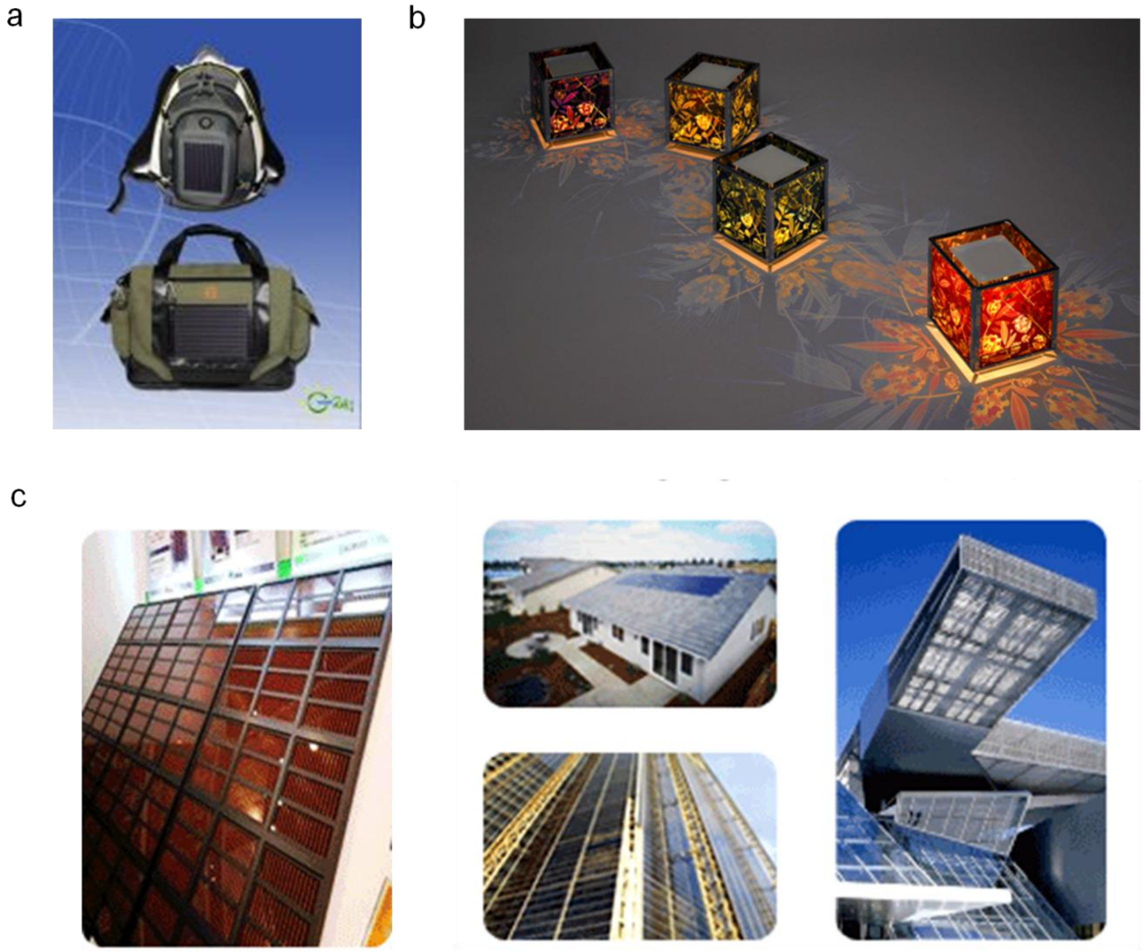

Figure 1.7 Applications of organic photovoltaics: (a) DSSC integrated bags [30]; (b) a conceptual lamp from Sony [31]; (c) DSSC attached windows, roofs and walls [32].

1.4.1 Power Conversion Efficiency

According to Shockley-Queisser theory, the efficiency limits of organic photovoltaics have been calculated to be about 23% [33]. The difference between the theoretical value and experimental data, 12%, indicates there is much room for further improvement. Solar energy conversion by photovoltaics relies on sequential steps from light absorption, and exciton harvesting, to charge extraction. It is evident that not all of these steps have a high efficiency. And the efficiency gap can be analyzed and identified by four main losses: optical losses, exciton losses, recombination losses and collection losses.

Optical losses describe only a portion of absorbed protons are involved in exciton generation. Although organic semiconductors have high light absorption coefficients, absorption behavior is still limited by the larger band gap and thus narrower absorption spectra of only few hundred nanometers.

Exciton losses are caused by ineffective exciton separation or insufficient transport of excitons to the donor-acceptor interface. Due to the covalent bonding in organic materials, the photogenerated excitons are localized, and their diffusion length only one tenth of that in silicon. Therefore, the effective working volume of exciton generation is smaller in organic photovoltaics, compared with inorganic counterparts involving the same structure.

Recombination losses mean a part of charge carriers recombine at the defects and interfaces. And collection losses are due to insufficient charge carrier mobilities, and thus only a part of the charge carriers can reach the contacts.

Various approaches have been made to these loss mechanisms, such as tandem devices; new chemicals with lower band gap; and better film morphologies with an optimum phase separation. In all cases, more research is needed, in order to find the most promising optimization methods and best device configurations.

1.4.2 Stability

As the power conversion efficiencies of organic photovoltaics approach commercial viability, degradation of device performance becomes one of the greatest obstacles that must be overcome before the final commercialization. Organic materials are by nature more susceptible to degradation than inorganic materials. The early PPV cells can only last for hours or days. However, in the last two decades, the lifetime of organic photovoltaics is being improved, by means of new chemical synthesis and various encapsulation techniques. In 2007, Frederik Krebs and Kion Norrman reported a device lifetime of up to 10000 hours [34]. Later, an outdoor testing was carried out by Jens Hauch and co-workers, showing the BHJ device of P3HT and fullerene derivative survived over one year without performance losses [35]. Improvements in device lifetime are undoubtedly encouraging; however, stability remains a serious concern.

To understand various degradation processes, there is a rough division between chemical and physical degradation occurring in organic photovoltaics. The chemical degradation involves both electrochemistry and photochemistry, focusing on the changes of materials mainly by oxygen, water, and light illumination; whereas physical degradation describes the morphological changes, such as metal atom diffusion and domain size growth.

1.5 THESIS OVERVIEW

To meet the remaining challenges of OPVs, the overall goal of the research, as well as the thesis objective thus becomes, to further improve the power conversion efficiency of OPVs, in the meantime to elucidate the mechanisms of the improvement and the degradation behavior of OPVs, and in particular to clarify the controversy of various device physics models developed in the literature.

Therefore, this thesis includes eight chapters. Chapter 1, *Introduction*, is the current chapter.

Chapter 2, *Literature Review*, provides a brief literature review in the fundamentals, and advanced topics in OPVs. This chapter is divided into six sections. The first two sections focus on the working principle and operational parameters of PVs, followed by the section showing the difference between PV and OPVs. The last three sections describe the development of the device architecture, morphology, and stability.

Chapter 3, *Experimental Procedure*, includes the details of device fabrication, power conversion efficiency measurement and related characterization techniques.

Chapter 4, *Improving the Efficiency*, presents a new method to increase the power conversion efficiency in OPVs. The resulting devices show 15% relative increase in efficiency by AC electric field alignment. This chapter contains one journal paper: Organic photovoltaic power conversion efficiency improved by AC electric field alignment during fabrication.

Chapter 5, *Studying the Nanostructure*, provides a more complete understanding of the energy efficiency improvement of OPVs by AC electric field alignment. Two distinguishable polymer nanostructures are found in the form of two separated layers, one of which is highly oriented and the other randomly distributed. This chapter contains one journal paper: Dual nanostructures in poly (3-hexylthiophene) based organic photovoltaics under alternative current electric field.

Chapter 6, *Tracking the Degradation*, presents multiple-interface tracking of degradation process in OPVs. Individual interface degradation is revealed by impedance measurements without breaking the device.

Chapter 7, *Investigating the Device Physics*, talks about the huge contrast in device physics between the bilayer and bulk heterojunctions in OPVs. The measured capacitance in BHJs is found to have two parallel components, one from the space charges of the Schottky junction, and the other from the dark dipoles formed spontaneously across the donor/acceptor interface.

Chapter 8, *Summary*, summarizes the key results of this work, and presents the most important conclusions.

REFERENCES

[1] U.S. Energy Information Administration, Trends in Renewable Energy Consumption and Electricity, 2012. (http://www.eia.gov/renewable/annual/trends/)

[2] European Photovoltaic Industry Association, Connecting the Sun, 2012. (http://www.connectingthesun.eu/)

[3] A. E. Becquerel, C. R. Hebd. Seances Acad. Sci. **9**, 561 (1839).

[4] J. Nelson, The Physics of Solar Cells, Imperial College Press, London, 2003.

[5] A. Goetzberger, C. Hebling, and H. W. Schock, Mater. Sci. Eng. R-Rep. **40**, 1 (2003).

[6] D. M. Chapin, C. S. Fuller, and G. L. Pearson, J. Appl. Phys. **25**, 676 (1954).

[7] National Renewable Energy Laboratory, US Department of Energy, Best Research Photovoltaic Cell Efficiencies, 2012. (http://www.nrel.gov/pv/)

[8] A. Blakers, Festkorperprobleme-Adv. Solid State Phys. **30**, 403 (1990).

[9] A. Luque, and S. Hegedus, Handbook of Photovoltaic Science and Engineering, Wiley, New York, 2011.

[10] H. Shirakawa, E. J. Louis, A. G. MacDiarmid, C. K. Chiang, and A. J. Heeger, J. Chem. Soc. Chem. Comm. **16**, 578 (1977).

[11] N. Hall, Chem. Comm. **1**, 1 (2003).

[12] S. Glenis, G. Horowitz, G. Tourillon, and F. Garnier, Thin Solid Films **111**, 93 (1984).

[13] N. S. Sariciftci, L. Smilowitz, A. J. Heeger, and F. Wudl, Science **258**, 1474 (1992).

[14] N. S. Sariciftci, D. Braun, C. Zhang, V. I. Srdanov, A. J. Heeger, G. Stucky, and F. Wudl, Appl. Phys. Lett. **62**, 585 (1993).

[15] G. Yu, J. Gao, J. C. Hummelen, F. Wudl, and A. J. Heeger, Science **270**, 1789 (1995).

[16] W. Ma, C. Yang, X. Gong, K. Lee, and A. J. Heeger, Adv. Funct. Mater. **15**, 1617 (2005).

[17] S. H. Park, A. Roy, S. Beaupre, S. Cho, N. Coates, J. S. Moon, D. Moses, M. Leclerc, K. Lee, and A. J. Heeger, Nature Photon. **3**, 297 (2009).

[18] Y. Liang, Z. Xu, J. Xia, S.-T. Tsai, Y. Wu, G. Li, C. Ray, and L. Yu, Adv. Mater. **22**, E135 (2010).

[19] H. Akamatsu, H. Inokuchi, and Y. Matsunaga, Nature **173**,168 (1954).

[20] M. Pope, and C. E. Swenberg. Electronic Processes in Organic Crystals and Polymers. Oxford University Press, USA, 1999.

[21] C. W. Tang, and A. C. Albrecht, J. Chem. Phys. **62**, 2139 (1975);

[22] C. W. Tang, Appl. Phys. Lett. **48**, 183 (1986).

[23] A. Yakimov, and S. R. Forrest, Appl. Phys. Lett. **80**, 1667 (2002).

[24] J. Xue, S. Uchida, B. P. Rand, and S. R. Forrest, Appl. Phys. Lett. **84**, 3013 (2004).

[25] J. Xue, B. P. Rand, S. Uchida, and S. R. Forrest, Adv. Mater. **17**, 66 (2005).

[26] Heliatek achieves 12% organic solar cell efficiency, 2013. (http://optics.org/news/4/1/36)

[27] B. O'Regan, and M. Grätzel, Nature **353**, 737 (1991).

[28] A. Yella, H.-W. Lee, H. N. Tsao, C. Yi, A. K. Chandiran, M. K. Nazeeruddin, E. W.-G. Diau, C.-Y. Yeh, S. M. Zakeeruddin, and M. Grätzel, Science **334**, 629 (2011).

[29] I. Chung, B. Lee, J. He, R. P. H. Chang, and M. G. Kanatzidis, Nature **485**, 486 (2012).

[30] http://www.g24i.com/press,g24i-ships-worlds-first-commercial-application-of-dssc,172.html

[31] http://www.sony.net/Fun/design/activity/sustainable/dssc.html

[32] http://www.samsungsdi.com/nextenergy/dssc-solar-cell-battery.jsp

[33] T. Kirchartz, K. Taretto, and U. Rau, J. Phys. Chem. C **113**, 17958 (2009).

[34] F.C. Krebs, and K. Norrman, Prog. Photovol. Res. Appl. **15**, 697 (2007).

[35] J. A. Hauch, P. Schilinsky, S. A. Choulis, R. Childers, M. Biele, and C. J. Brabec. Sol. Energy Mater. Sol. Cells **92**, 727 (2008).

Chapter 2. LITERATURE REVIEW

2.1 WORKING PRINCIPLE OF PHOTOVOLTAICS

The modern photovoltaic devices rely on the development of the semiconducting materials and their p/n junctions. The process of converting solar energy into electricity in the p/n junction based photovoltaics can be generally depicted as the following four steps: a) *light absorption* creating excitons; b) *exciton diffusion* to the interface between the p type donor and n type acceptor, where c) *charge separation* occurs; d) the *charge transport* to the anode (holes) and cathode (electrons), to provide a direct current for the external load.

2.1.1 P/n Junction and Built-in Electric Field

Let us consider the simplest case of p type and n type silicon brought together to form a p/n junction. Determined by the band diagram, p type silicon has a large concentration of holes and few electrons by doping group III atoms; whereas the converse is true for n type silicon doped with group V atoms (**Figure 2.1**).

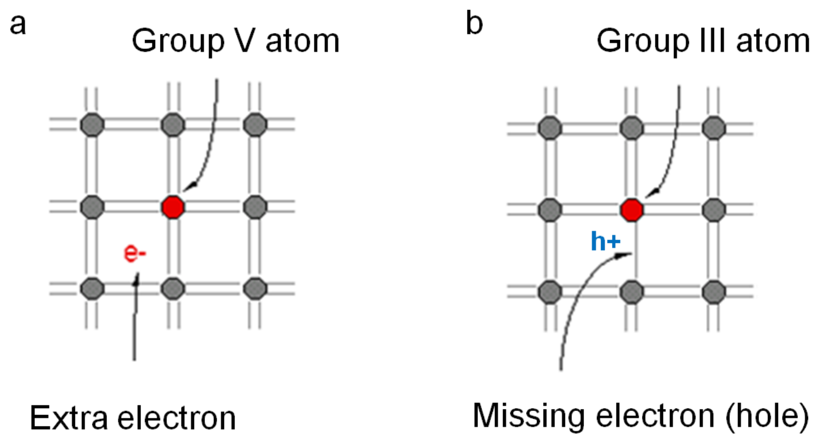

Figure 2.1 N doped silicon (a) and p doped silicon (b).

When two pieces of materials are joined, holes are expected to diffuse from the p type silicon to n type and electrons from n type to p type, due to the charge carrier concentration gradients at the junction, as shown in **Figure 2.2a**. The resulting diffusion current is directed from the p type silicon to n type. The uncompensated ions left behind, acceptors in the p type silicon and donors in the n type, develop a negative space charge region near the p side of the junction, and a positive charge region near the n side. The built-in electric field generated by these space charges is in the opposite direction to the diffusion current, creating a drift current from the n type silicon to p type.

When equilibrium state is attained, the drift current originated from the built-in electric field should cancel the diffusion current. And this electric field builds up to the point where the net current is zero at equilibrium. At the same time, the built-in electric field causes an equilibrium electrostatic potential difference (V_{bi}) across the region where it appears. The region is called as depletion zone (W), and the potential difference across the depletion zone works as a built-in potential barrier, which is necessary to the maintenance of equilibrium condition at the p/n junction. When this potential energy (qV_{bi}) is superimposed onto the band diagram, the Fermi levels of p type and n type silicon get aligned (**Figure 2.2b**).

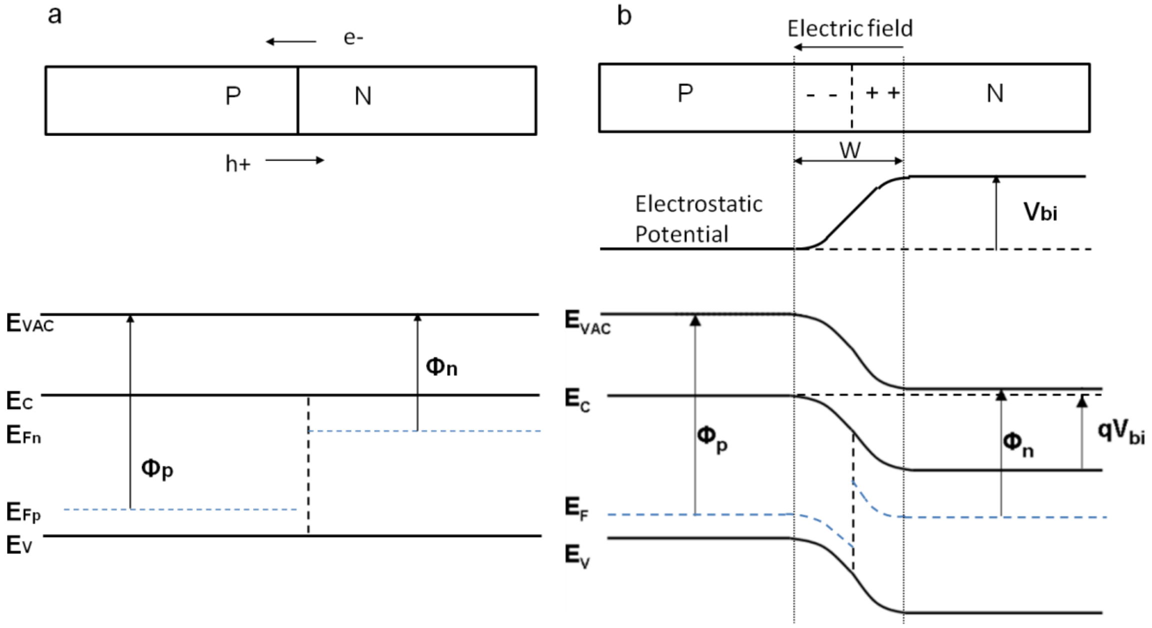

Figure 2.2 Properties of a p/n junction: (a) Materials are joined and charges begin to diffuse; (b) an equilibrium p/n junction, showing space charge in the depletion zone (W), the resulting electric field, the built-in potential (V_{bi}), and the energy bands. E_{VAC}, E_C, E_{Fn}, E_{Fp}, and E_v stand for the vacuum level, conduction band, Fermi level of the n type silicon, Fermi level for the p type silicon, and valence band, respectively.

2.1.2 Light Absorption

The light absorption of photovoltaics, mainly ranged from near-infrared to ultraviolet, is due to band-to-band transitions in semiconductors. It is apparent that photons with energies greater than the band gap of a semiconductor can be absorbed, while photons with less energies are transmitted. The band structures of inorganic semiconductor crystals, such as silicon, arise from valence electrons of each atom in the outer orbit shared by its four neighbors. When the atomic orbitals are overlapped head-to-head, σ bonds are formed that hold the atoms together. When a photon is absorbed, its energy is transferred to an electron in silicon, which is then excited from the valence band to the conduction band in a σ – σ* transition (where *denotes the excited state), leaving an empty state in the valence band referred to as a hole. An electron-hole pair is thus created known as an exciton.

The electron jumping to the conduction band by photon adsorption may initially have more energy than is common for conduction band electrons (**Figure 2.3a**); however, it will give up energy to the lattice by scattering events until its velocity reaches the thermal equilibrium velocity of other electrons in the conduction band (**Figure 2.3b**). If the electron-hole pair cannot be separated within its lifetime, the electron in the conduction band will eventually recombine with the hole in the valence band, giving off a photon or phonon (**Figure 2.3c**). However, in a photovoltaic device, the exciton is separated, and the resulting charge carriers are fed to an external circuit.

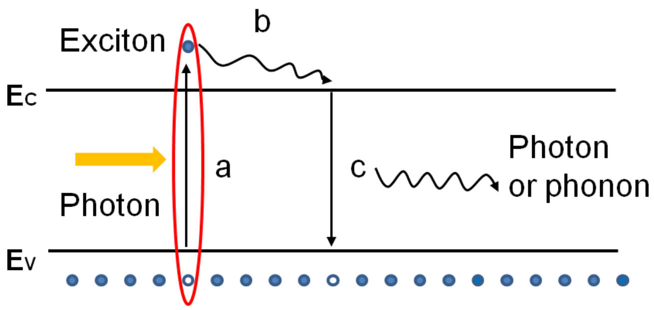

Figure 2.3 Excitation and recombination mechanisms.

2.1.3 Exciton Diffusion and Charge Separation

The key feature of a photovoltaic is that it has an interface that separates electrons and holes so they can be collected by respective electrodes before recombination, and travel through the external circuit. This indicates that all photovoltaics must be diodes, accomplished by p/n junctions in efficient devices, where current can only flow in one direction. The photogenerated electron-hole pairs in inorganic semiconductors are highly delocalized, with a radius covering several lattice constant distance [1]. These excitons diffuse to the p/n interface, and then dissociate (**Figure 2.4**).

It has been realized that the dielectric properties of materials influence the charge separation process. Inorganic semiconductors are highly polarizable, with larger dielectric constants compared to the organic ones. The dielectric constant of crystalline silicon is about 11.9, while in crystalline carbon, such as diamond, is 5.7 [2]. There is an electrochemical analogy about the dielectric constant and its electrostatic effects: the ionic electrolyte added to a solvent to screen electric field only works for solvents with a dielectric constant above about $\varepsilon = 8$ [3]; below that, the anions and cations in the electrolyte are so strongly bound to each other by the Coulombic attraction that they cannot dissociate. Likewise, this large dielectric constant ensures that charges can be screened from each other in inorganic semiconductors. And in inorganic photovoltaics, the electron-hole pairs created by light absorption are delocalized, which can easily be separated into electrically charged free carriers, by the thermal energy of 26meV at room temperature.

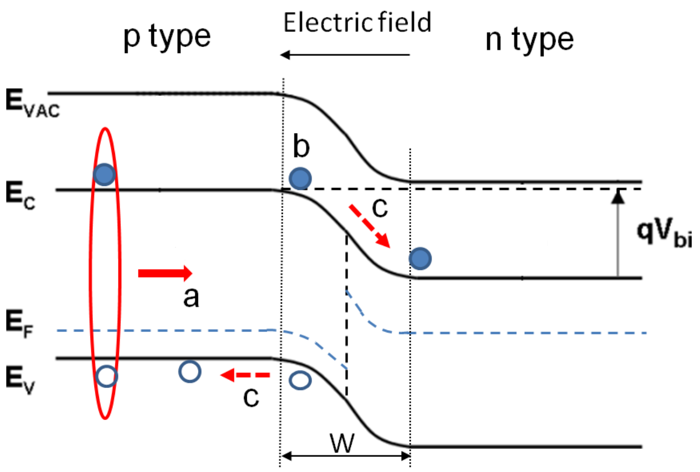

Figure 2.4 Exciton diffusion (a), dissociation (b) and charge transport (c) finally to the electrodes. E_{VAC}, E_C, E_{Fn}, E_F, and E_v stand for the vacuum level, conduction band, Fermi level, and valence band, respectively.

2.1.4 Charge Transport

Once excitons are separated into electrons and holes, these free charge carriers must move through the bulk and finally to the respective electrodes, in order to be utilized to do electrical work. Charges transport via two main mechanisms, drift and diffusion.

Drift describes the charge flow under an electric field and is characterized by

$$v = \mu E \qquad \text{(Eq. 2.1),}$$

where v is the average drift velocity, μ the charge carrier mobility, and E the electric field strength. The drift current is the net motion of these charges due to the electric field:

$$J_{Drift} = q\mu\rho(x)E(x) \qquad \text{(Eq. 2.2),}$$

where J_{Drift} is the drift current density, q the elementary charge, and $\rho(x)$ the charge carrier density distribution [4]. The total drift current is the sum of the contributions due to electrons and holes.

When free carriers are created nonuniformly, the electron and hole concentrations vary with position. Any such distribution results in a net motion of the carriers, defined as diffusion, from high concentration to low concentration. Diffusion current is given by:

$$J_{Diffusion} = qDd\rho(x)/d(x) \qquad \text{(Eq. 2.3),}$$

where D is the diffusion coefficient of electron or hole, and $d\rho(x)/d(x)$ the flux density [4]. Similarly, electron and hole diffusion currents should be counted into the overall current.

In an inorganic photovoltaic, the built-in electric field exists across the depletion zone of the p/n junction; while there is no electric field outside. An electron-hole pair created near the junction on the p side provides a minority electron in the p type material. If this electron-hole pair is within the diffusion length, the electron can diffuse to the junction and be swept down the barrier to the n side by drift (**Figure 2.4**). However, the free charges migration through the bulk is mainly by diffusion.

2.2 POWER CONVERSION EFFICIENCY OF PHOTOVOLTAICS

The photovoltaic can be regarded as a power source in an electric circuit. In the dark it does nothing; however, it generates a current under illumination. The maximum current obtained when the nodes are connected together is the short circuit current, I_{sc}. The maximum voltage available when the nodes are isolated is called the open circuit voltage, V_{oc}. For any load resistance in between, the current and voltage relationship is determined by the current-voltage characteristic of the photovoltaic under illumination. Since the current is proportional to the illuminated area, the short circuit current density J_{sc} is more useful to make comparison. These quantities are defined to describe the performance of a photovoltaic.

2.2.1 Photocurrent and Quantum Efficiency

The photocurrent generated by a photovoltaic under illumination is dependent on the incident light spectrum at short circuit condition. Their relationship can be revealed by the device's external quantum efficiency, EQE, via:

$$J_{sc} = qA^{-1}\int\Phi(\lambda)EQE(\lambda)d\lambda \qquad \text{(Eq. 2.4),}$$

where A is the device area, $\Phi(\lambda)$ the incoming photon flux at each wavelength λ, and $EQE(\lambda)$ the ratio of charges collected at electrodes over the number of incident photons, showing the probability that a photon of energy hc/λ will produce one electron in the external circuit. The integral starts from $\lambda=0$ to the cut-off wavelength determined by the band gap of the semiconductor [5]. *EQE* relies on the absorption coefficient of the semiconductor, the efficiencies of charge separation and the charge transport in the photovoltaic; however, it is independent of the incident light spectrum. **Figure 2.5** shows a typical EQE and Air Mass 1.5 Global (AM1.5G) photon flux spectra. It is desirable to have a high EQE at wavelengths where the photon flux is large.

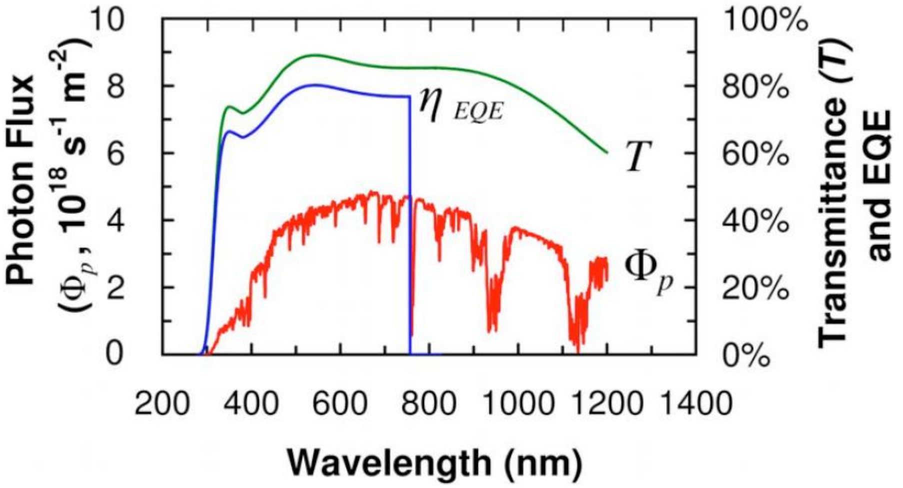

Figure 2.5 AM1.5G photon flux, the optical transmittance, and EQE (for the bandgap of 1.5 eV) spectra [5].

2.2.2 Dark Current and Open Circuit Voltage

Photovoltaics behave like diodes, due to the p/n junctions in efficient devices, where current can only flow in one direction. In the dark, the device shows the rectifying behavior, allowing a much larger current under forward bias ($V > 0$) than under reverse bias ($V < 0$). For an ideal diode the dark current density $J_{dark}(V)$ is given by:

$$J_{dark}(V)=J_o(e^{qV/KT}-1) \qquad \text{(Eq. 2.5),}$$

Where J_o is a constant, dominated by leakage charge generation and tunneling, K is Boltzmann's constant and T absolute temperature [6].

The overall current varies with applied voltage, and its current-voltage characteristic can be estimated to be the sum of the short circuit current and dark current (**Figure 2.6**). Although the reverse current which flows in the opposite direction under illumination is not formally equal to the dark current, this superposition approximation is well-accepted for many inorganic photovoltaics. The resulting net current density in the device is [6]:

$$J(V) = J_{dark}(V) - J_{sc} \qquad \text{(Eq. 2.6).}$$

Therefore, the expression for an ideal diode becomes:

$$J(V) = J_o(e^{qV/KT}-1) - J_{sc} \qquad \text{(Eq. 2.7).}$$

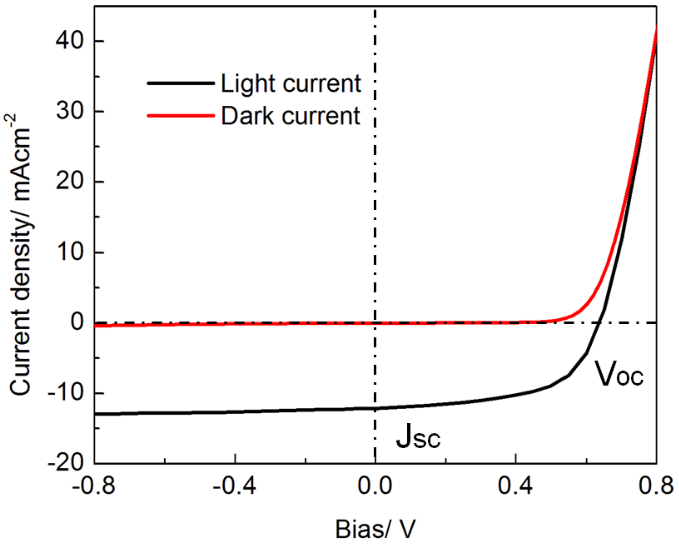

Figure 2.6 Current density-voltage characteristic of a photovoltaic in the light and the dark.

As discussed, in the open circuit condition, the device has its maximum voltage output, V_{oc}, which is equivalent to the situation of zero net current, when the dark current cancels out the short circuit current. Thus,

$$V_{oc} = KT \ln(1+J_{sc}/J_o)/q \qquad \text{(Eq. 2.8).}$$

2.2.3 Fill Factor and Power Conversion Efficiency

It should be noted that the photovoltaic generates power when the voltage is between 0 and V_{oc}. The power density of photovoltaics is given by the product of current density and voltage, and the maximum power density, P_{max}, is obtained when the product reaches its maximum. This optimum operating condition is marked in **Figure 2.7**, with the voltage V_m and corresponding current density J_m. The fill factor, *FF*, is then given by:

$$FF = J_m V_m / J_{sc} V_{oc} \qquad \text{(Eq. 2.9)},$$

which describes the squareness of the current-voltage characteristic curve [6].

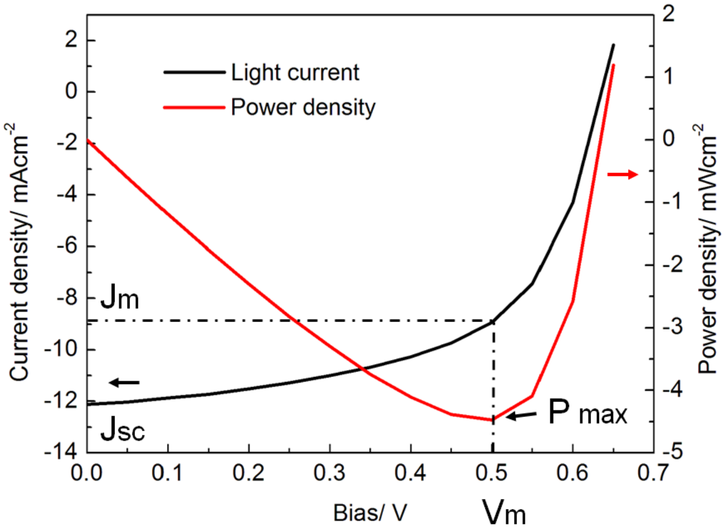

Figure 2.7 Current density-voltage and power density-voltage characteristics of a photovoltaic. Power density reaches a maximum (P_{max}) at a bias of V_m and current density of J_m.

The power conversion efficiency, *PCE,* is defined as the ratio of the maximum power density generated at this optimum operation condition over the incident light power density, P_{in},

$$PCE = J_m V_m / P_{in} \qquad \text{(Eq. 2.10).}$$

PCE can also be given by:

$$PCE = J_{sc} V_{oc} FF / P_{in} \qquad \text{(Eq. 2.11).}$$

J_{sc}, V_{oc}, *FF*, and *PCE* are the most important quantities of a photovoltaic [6].

2.2.4 Ideal Diode Model and Resistances

To further understand the significance of these quantities, the photovoltaic can be modeled electrically as a current generator in parallel with an ideal diode, and the corresponding current-voltage characteristic can also be explained by this ideal diode model. In the real devices, the device performance is lowered by the existence of all kinds of resistances and current leakage. The origins of loss have been taken into consideration, by adding series and parallel resistances into the equivalent circuit (**Figure 2.8**). The series resistance (R_s) includes the resistance of the bulk material and contacts, acting as a hindrance especially at high current densities; while parallel resistance (R_p) arises from the leakage of current from the sides and edges of the device, which is a particular problem in poorly rectifying devices.

Accordingly, the diode equation is modified to include the resistances [6]:

$$J(V) = J_o(e^{q(V-JARs)/KT}-1)-(V-JAR_s)/R_p - J_{sc} \qquad \text{(Eq. 2.12).}$$

Series and parallel resistances can also reduce fill factor in difference ways as shown in **Figure 2.9**. In order to obtain an efficient photovoltaic, R_s should be as small and R_p as large as possible.

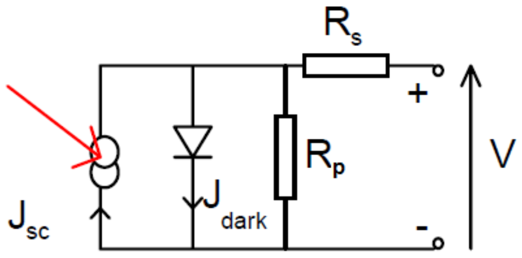

Figure 2.8 Equivalent circuit including series (R_s) and parallel (R_p) resistances.

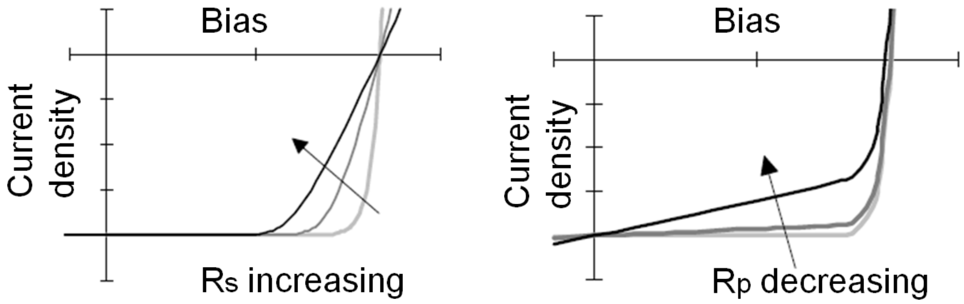

Figure 2.9 Effects of increasing series (R_s) and reducing parallel (R_p) resistances. The direction of the increase or decrease is expressed by the arrow.

2.3 FROM INORGANIC TO ORGANIC PHOTOVOLTAICS

Since the development of conducting polymers in 1970s, organic photovoltaics have attracted both scientific and economic interest due to a rapid increase in power conversion efficiencies. Their working principle is schematically similar to that of inorganic cells. However, there are some important features of organic semiconductors, making organic photovoltaics different from their inorganic counterparts.

Due to the large band gap in organic semiconductors, the harvesting of light spectrum is limited in organic photovoltaics, and only a small number of the incident photons can be absorbed. For example, the polymer having the band gap of 2 eV is capable of absorbing about 30% of the incident light; whereas Si with a band gap of 1.1 eV can absorb incoming solar photons up to 77% [7]. On the other hand, organic semiconductors have relatively high absorption coefficients of more than 10^5 cm^{-1}, indicating that about 100 nm thick photoactive layer is enough for strong absorption, compared with several micrometers in inorganic devices.

Another difference from crystalline inorganic semiconductors lies in the electronic and dielectric properties of organics. Though partly balanced by the thin device structure, the low charge carrier mobility limits the device applications at high current densities. As compared to Si, the valence electrons of carbon atoms are more tightly bound to the nucleus, and in most organic materials, the dielectric constant is from 3.5 to 5.5 [8]. Consequently, the photoexcitations in organic photovoltaics do not directly lead to free charge carriers, but to coulombically bound electron-hole pairs. It was reported that only

10% of the excitons generate free charge carriers in conjugated polymers [9]. The thermal energy at room temperature is now insufficient to separate these photogenerated excitons, and strong electric fields are needed for charge separation. Photoinduced charge transfer can occur when the exciton has reached an interface, where the change of potential energy provides strong local built-in electric field. Since the excitons are localized with a shorter exciton diffusion length of 10-20 nm [7], the donor and acceptor domains should be at the same order of magnitude as the diffusion length. Otherwise, bound electron-hole pairs will recombine before reaching the interface.

2.4 DEVICE ARCHITECTURES

As discussed in **Section 1.3**, the early development of organic photovoltaics was driven mainly by the breakthroughs in device architectures. In two decades, organic photovoltaics evolved from simple single layer structures placed between electrodes with different work functions, to more complex, phase-separated BHJs with an interpenetrating 3D network.

2.4.1 Single Layer

The first organic photovoltaics were based on single organic layers sandwiched in between two dissimilar metal electrodes. As shown in **Figure 2.10**, the metal-insulator-metal (MIM) model is depicted to understand device rectifying behavior [2]. In this model, the intrinsic organic semiconductor layer is regarded as a piece of insulator of several nanometers thick, and electron can tunnel through it. The metals are plotted by their Fermi levels, and the organic semiconductor is represented by the lowest unoccupied molecular orbital (LUMO) and highest occupied molecular orbital (HOMO), corresponding to the conduction and valence bands in inorganic semiconductors. Under short circuit condition (a), the built-in electric field is evenly distributed across the device, resulting from the electron tunneling from one metal to the other. Under illumination, separated charge carriers can drift in this electric field to the respective electrodes. At the open circuit condition (b), also known as the flat band condition, the applied voltage cancels out the built-in field, and there is no driving force for charge carriers.

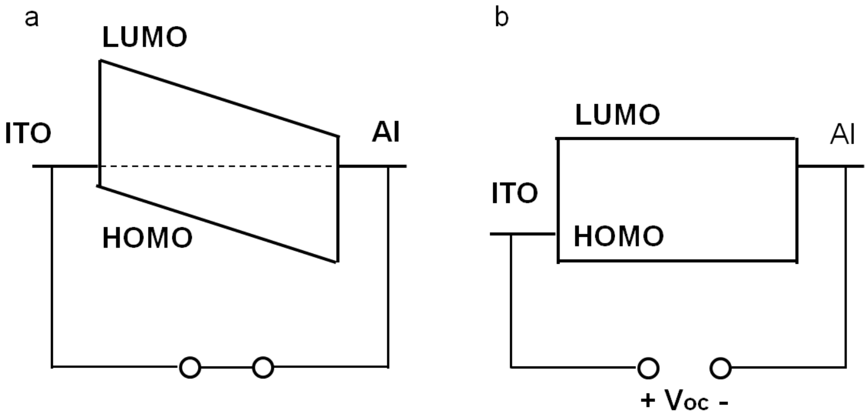

Figure 2.10 Metal-insulator-metal (MIM) model of the single layer organic photovoltaics: (a) short circuit condition, and (b) open circuit condition.

Later, it was found that the organic semiconductors can easily be p-doped by oxygen and moisture [10], and thus a Schottky barrier was formed between the p-type organic layer and the low work function metal [2]. Accordingly, the MIM model is modified with a Schottky junction at the aluminum contact in **Figure 2.11**. Near the contact, there is a band bending in the depletion region, where excitons can be separated. Limited by the diffusion length, only excitons generated within the 10-20nm from the contact can finally lead to the photocurrent. The power conversion efficiencies of these single layer devices were usually below 1% [11].

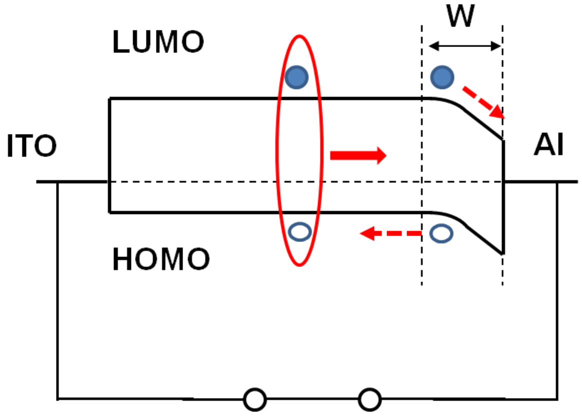

Figure 2.11 Schematic of a single layer device with a p type Schottky contact at the aluminum electrode. Photogenerated excitons can only be separated in the depletion zone (W).

2.4.2 Bilayer Heterojunction

A bilayer heterojunction device consists of a planar interface between the donor and acceptor materials. At the interface, charge separation occurs, with the help of the potential drop between the donor and acceptor. Ideally, the bilayer is sandwiched between two electrodes with difference work functions, matching the donor HOMO level and acceptor LUMO level, for good hole and electron collection, respectively. The bilayer model [12] is depicted in **Figure 2.12**, where any possible band bending due to the energy level alignment is neglected. Since photogenerated excitons can only be dissociated in a thin layer near the interface, the bilayer device is exciton diffusion limited.

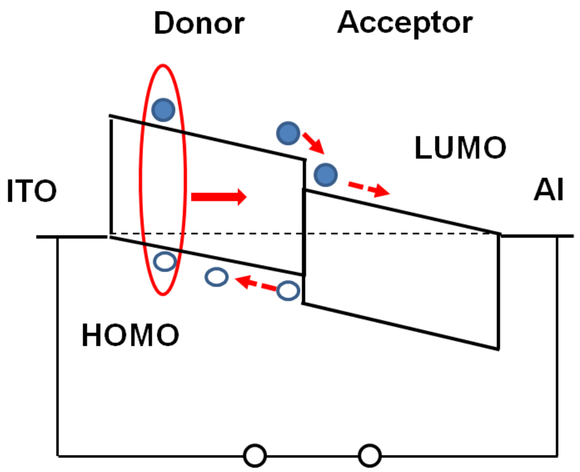

Figure 2.12 Schematic of a bilayer heterojunction organic photovoltaic. Any possible band bending due to the energy level alignment has been neglected.

Compared with the single layer device, the advantage of bilayer structure is its monomolecular charge transport. When the excitons are separated at the interface, the electrons travel through the acceptor domains and holes through donor domains. Thus, holes and electrons are separated from each other, and recombination of charges is reduced.

2.4.3 Bulk Heterojunction

In a BHJ device, the donor and acceptor materials are mixed intimately in the bulk so that the excitons are never too away from the interface. Therefore, all the photogenerated excitons are expected to be dissociated into charges at any place within their lifetime, and the BHJ device is no longer exciton diffusion limited. In order to achieve efficient hole and electron collection at both electrodes, the donor and acceptor materials should form a three-dimensional interpenetrating bicontinuous network, which is highly related to the nanoscale morphology of the active layer.

As shown in **Figure 2.13**, there are two main models describing BHJs in the literature, the MIM BHJ model and the Schottky junction BHJ model. The MIM BHJ model (**Figure 2.13 a**) treats the undoped organic active layer as an insulator, and thus this model is similar to the MIM model [12, 13]. Largely based on the photoconduction in insulators, the model applies well in the explanations of exciton dissociation and device open circuit voltage, by the separation of HOMO and LUMO levels in the polymer and fullerene [13]; Whereas the Schottky junction BHJ model [14] involves a p-type Schottky junction at the Al electrode (**Figure 2.13 b**), which assumes that the active layer is not an insulator, rather it contains holes as the majority carrier, with a characteristic density of 10^{15}–10^{17} cm^{-3}, originated from the p-doping of the polymer when exposed to air or water moisture, or caused by the structural defects induced during processing [15]. It has been used to analyze the charge carrier distribution, transport properties, and lifetime in BHJs [16].

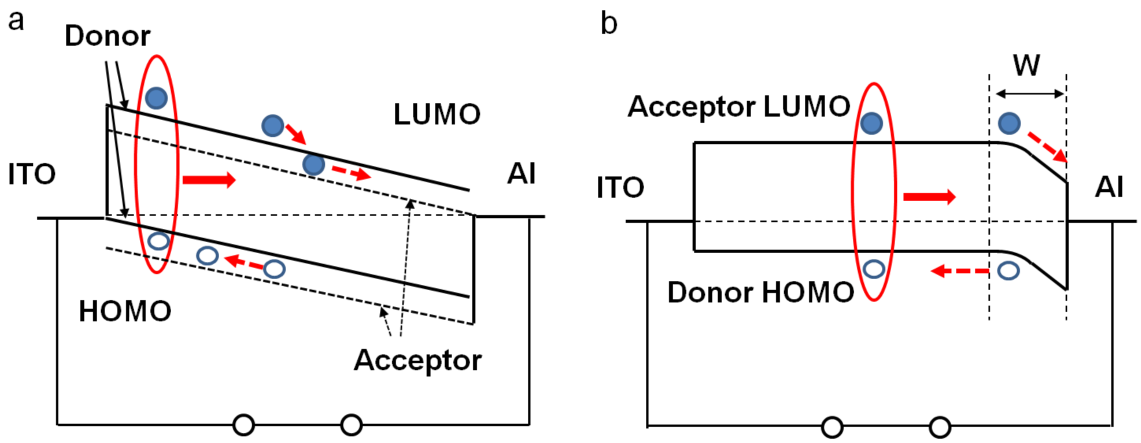

Figure 2.13 The models of a bulk heterojunction device: (a) based on the metal-insulator-metal model and (b) on the Schottky junction.

2.4.4 Diffuse Bilayer Heterojunction

The diffuse bilayer heterojunction is proposed conceptually in between the bilayer and BHJ structures, which involves the benefits of both architectures, an enlarged donor-acceptor interface where exciton separation can be maximized, and continuous pathways of electrons and holes for efficient charge collection at the corresponding electrodes. In literature, the diffuse bilayer structure can be processed in various ways. In 2011, Alan J. Heeger and his co-workers spin-coated a second layer from the solvent that partially dissolved the bottom polymer layer, and controlled the interdiffusion between fullerene molecules and polymer domains by annealing [17]. The resulting devices showed similar energy conversion efficiencies to the BHJ devices of about 3.6% [17].

2.5 NANOSCALE MORPHOLOGY

The performance of organic photovoltaics depends largely on the physical interaction of the donor and acceptor materials, although the open circuit voltage of the device is mainly determined by the band diagram of the components. The ideal BHJ device is designed as a bicontinuous network, with an enlarged donor-acceptor interface for maximized exciton separation, and a finer domain size comparable to the exciton diffusion length of about 10 nm. Both donor and acceptor domains are expected to be phase segregated to a certain extent, in order to form the hole and electron pathways for effective charge transport to the electrodes. In other words, a balance between the mixing and de-mixing of donor and acceptor components should be obtained, for optimal nanoscale morphology and the resulting performance.

The morphology of the active layer is based upon many intrinsic and extrinsic variables. The intrinsic factors include the crystallinity and miscibility of these two materials; whereas the extrinsic properties involve all possible external influences during the whole device fabrication, such as the solvent choice, concentration, deposition method, temperature, and annealing condition. Their effects may vary, according to different selection of materials.

The P3HT/$PC_{61}BM$ system is a well studied polymer-fullerene combination, with efficiencies of 3-5% [18-21]. Several optimization methods have been applied in the most efficient P3HT/$PC_{61}BM$ BHJ devices. It was found that a 1:1 [19] or 1:0.8 [18, 20] blend of polymer to fullerene can give the device with a better performance, which is associated with the degree of miscibility between P3HT and $PC_{61}BM$. Chlorobenzene and 1,2-dichlorobenzene are widely used [18-20], since both P3HT and $PC_{61}BM$ are soluble in these two solvents. An energy conversion efficiency of below 1% was obtained from a solution of 10mg mL^{-1} P3HT and 8mg mL^{-1} $PC_{61}BM$ in chlorobenzene, and the as-cast film showed little phase segregation over several nanometers [18]. The poor performance of the as-cast device was explained by the homogenous composite active layer, rather than the desired bicontinuous network with well-developed charge carrier pathways [18].

A number of methods have been proposed to obtain a better morphology from the as-cast film. The most successful treatment is the thermal annealing [22]. Heating the active layer to a temperature greater than the glass transition temperature of P3HT [23], would allow the polymer chains to reorganize, and at the same time the fullerene molecules is free to diffuse in a more thermodynamically favorable way. **Figure 2.14** shows that how the thermal annealing leads to the development of a nanoscale phase separation in a1:1 blend of P3HT and $PC_{61}BM$ device [24]. The domain size of P3HT and $PC_{61}BM$ can be tuned by different annealing temperatures at short annealing times. Once a highly ordered bicontinuous network of P3HT and $PC_{61}BM$ has been formed by thermal annealing, the energy efficiency rises to 3-5%, which is also the best efficiency for this system.

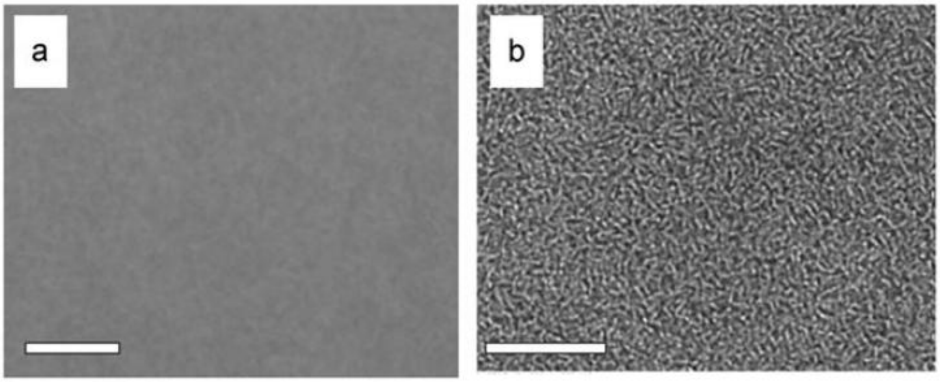

Figure 2.14 TEM images of the P3HT/$PC_{61}BM$ film: (a) the 1:1 blend of P3HT and $PC_{61}BM$ before annealing; (b) the same sample after annealing at 150 ^{o}C for 30 mins. The scale bars are both 0.5 µm [24].

Similar enhancements in device performance have also been reported with other techniques such as solvent annealing. Yang Yang and his co-workers first used this technique to control the solvent evaporation from the cast film of a 1:1 blend of P3HT and $PC_{61}BM$ [19, 25]. When the as-cast film was placed in a covered petri dish over 20 mins before electrode deposition, an energy efficiency of 3.52% was obtained without further thermal annealing [25]. The experiment suggests that the solvent molecules play an important role in the phase reorganization, which is comparable to that obtained by thermal annealing.

2.6 DEVICE STABILITY

As a final concern before the commercialization of organic photovoltaics, the stability of devices needs to be optimized. Stability is evaluated in various ways under different conditions, and in general, it can be divided into ambient and thermal stability.

The ambient stability is mainly affected by the influences of water and oxygen. As depicted in **Figure 2.15**, organic materials and metal electrodes are susceptible to the reactions with water and oxygen [26]. While polymers suffer from the photo-oxidation [27], the hole transport layer (PEDOT:PSS) can take up water and thus increase the device resistance [28]. The hygroscopic nature of PSS allows the absorption of water that facilitates etching of the ITO layer [29]. In order to protect devices from water and oxygen, encapsulation has been widely accepted and ambient stability may be realized by this technique.

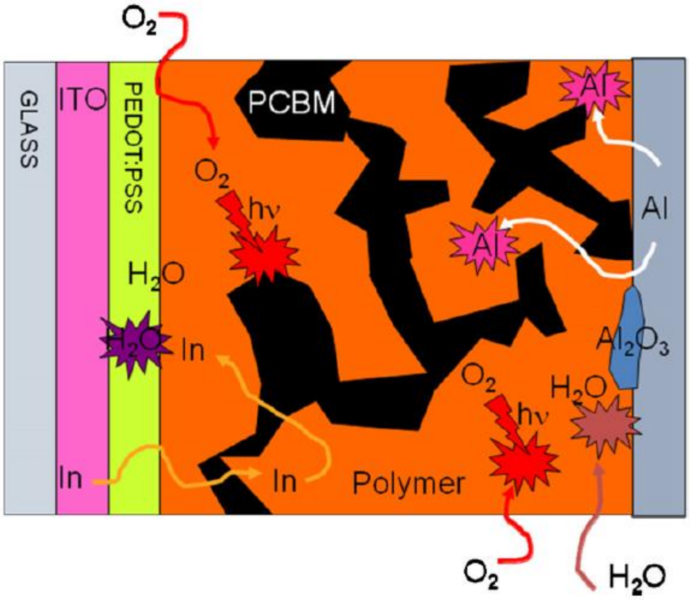

Figure 2.15 A schematic illustration of some degradation processes that take place in a typical bulk heterojunction device [26].

Thermal stability is more critical, since it is well-documented that the phase instability of organic photovoltaics makes them unstable to long-term exposure to the sun light or elevated temperatures [30]. Compared with the PPV/PC$_{61}$BM system, BHJ devices based on P3HT/PC$_{61}$BM show better thermal stability due to the intrinsic miscibility. It has also been found that the regioregularity of the polymer acts as a driving force for crystallization, and thus enhances phase separation with PC$_{61}$BM [24]. In order to improve the thermal stability and reduce phase separation, there are two main methods, either adding compatibilizers as the additive, or introducing cross-linkable functional groups. When diblock copolymer functionalized with P3HT and fullerene on each block was added into a 1:1 blend of P3HT and PC$_{61}$BM at a weight ratio of 17%, the efficiency of the device remained at the same level during 10 hour annealing at 140 °C [31]. When $PC_{61}BM$ was functionalized with the epoxide, and then blended with P3HT, the resulting film showed greater phase stability and no phase separation was observed at the annealing condition [32].

REFERENCES

[1] S. R. Forrest, Chem. Rev. **97**, 1793 (1997).

[2] S. M. Sze, Physics of Semiconductor Devices, Wiley Interscience, New York, 1981.

[3] A. J. Bard, and L. R. Faulkner, Electrochemical Methods, Wiley & Sons, New York, 1980.

[4] B. Streetman, and S. K. Banerjee, Solid state electronic devices, Pearson Prentice-Hall, New York, 2009.

[5] J. D. Servaites, M. A. Ratner, and T. J. Marks, Appl. Phys. Lett. **95**, 163302 (2009).

[6] J. Nelson, The Physics of Solar Cells, Imperial College Press, London, 2003.

[7] J. M. C. R. Nunzi, Physique **3**, 523 (2002).

[8] K. Walzer, B. Maennig, M. Pfeiffer, and K. Leo, Chem. Rev. **107**, 1233 (2007).

[9] P. B. Miranda, D. Moses, and A. J. Heeger, Phys. Rev. B **64**, 81201 (2001).

[10] A. K. Gosh, D. L. Morel, T. Feng, R. F. Shaw, and C. A. Rowe, J. Appl. Phys. **45**, 230 (1974).

[11] A. K. Gosh, and T. Feng, J. Appl. Phys. **49**, 5982 (1978).

[12] H. Hoppe, and N. S. Sariciftci, J. Mater. Res. **19**, 1924 (2004).

[13] C. Deibel, and V. Dyakonov, Rep. Prog. Phys. **73**, 096401 (2010).

[14] G. Garcia-Belmonte, A. Munar, E. M. Barea, J. Bisquert, I. Ugarte, and R. Pacios, Org. Electron. **9**, 847 (2008).

[15] S. Hoshino, M. Yoshida, S. Uemura, T. Kodzasa, N. Takada, T. Kamata, and K. Yase, J. Appl. Phys. **95**, 5088 (2004).

[16] F. Fabregat-Santiago, G. Garcia-Belmonte, I. Mora-Sero, and J. Bisquert, Phys. Chem. Chem. Phys. **13**, 9083 (2012).

[17] J. S. Moon, C. J. Takacs, Y. Sun, and A. J. Heeger, Nano. Lett. **11**, 1036 (2011).

[18] W. Ma, C. Yang, X. Gong, K. Lee, and A. J. Heeger, Adv. Funct. Mater. **15**, 1617 (2005).

[19] G. Li, V. Shrotriya, J. Huang, Y. Yao, T. Moriarty, K. Emery, and Y. Yang, Nat. Mater. **4**, 864 (2005).

[20] M. Reyes-Reyes, K. Kim, and D. L. Carroll, Appl. Phys. Lett. **87**, 083506 (2005).

[21] K. Kim, J. Liu, M. A. G. Namboothiry, and D. L. Carroll, Appl. Phys. Lett. **90**, 163511 (2007).

[22] F. Padinger, R. S. Rittberger, and N. S. Sariciftci, Adv. Funct. Mater. **13**, 85 (2003).

[23] Y. Kim, S. A. Choulis, J. Nelson, D. D. C. Bradley, S. Cook, and J. R. Durrant, Appl. Phys. Lett. **86**, 063502 (2005).

[24] K. Sivula, C. K. Luscombe, B. C. Thompson, and J. M. J. Frechet, J. Am. Chem. Soc. **128**, 13988 (2006).

[25] V. Shrotriya, Y. Yao, G. Li, and Y. Yang, Appl. Phys. Lett. **89**, 063505 (2006).

[26] M. Jorgensen, K. Norrman, and F. C. Krebs, Sol. Energy Mater. Sol. Cells **92**, 686 (2008).

[27] M. S. A. Abdou, F. P. Orfino, Y. Son, and S. Holdcroft, J. Am. Chem. Soc. **119**, 4518 (1997).

[28] K. Kawano, R. Pacios, D. Poplavskyy, J. Nelson, D. D. C. Bradley, and J. R. Durrant, Sol. Energy Mater. Sol. Cells **90**, 3520 (2006).

[29] M. P. de Jong, L. J. van Ijzendoorn, and M. J. A. de Voigt, Appl. Phys. Lett. **77**, 2255 (2000).

[30] X. Yang, J. K. J. van Duren, R. A. J. Janssen, M. A. J. Michels, and J. Loos, Macromolecules **37**, 2151 (2004).

[31] K. Sivula, Z. T. Ball, N. Watanabe, and J. M. J. Frechet, Adv. Mater. **18**, 206 (2006).

[32] M. Drees, H. Hoppe, C. Winder, H. Neugebauer, N. S. Sariciftci, W. Schwinger, F. Schaffler, C. Topf, M. C. Scharber, Z. Zhu, and R. Gaudiana, J. Mater. Chem. **15**, 5158 (2005).

Chapter 3. EXPERIMENTAL PROCEDURES

3.1 DEVICE FABRICATION

The organic photovoltaics were prepared on the commercial ITO patterned glass substrates (thickness of ITO ~150 nm, sheet resistance ~12Ω/square). The ITO substrates were subsequently sonicated in acetone, isopropanol and de-ionized water bath, then blow dried with N_2 gas and stored in an oven at 80 ℃ over night.

The substrates were subject to ozone plasma treatment for 10 minutes before use, followed by spin-coating a 40 nm thick film of poly(3,4- ethylenedioxythiophene): polystyrenesulfonate (PEDOT:PSS, Sigma-Aldrich). The PEDOT:PSS conducting layer was dried at 120 ℃ for 10 minutes in a N_2 filled glove box. A prepared polymer blend, consisting of P3HT/$PC_{61}BM$, or PTB7/ $PC_{71}BM$ (1-Materials), which were dissolved separately in 1,2-dichlorobenzene solution in a designed weight ratio, was then spin-coated on top.

The active layer was allowed to dry under various experimental conditions. They were then annealed at 120℃ for another 10 minutes. Finally, a metal cathode was deposited onto the half-finished device by a vacuum evaporation system. The experimental setups are depicted in **Figure 3.1**.

Figure 3.1 The experimental setups: (a) a N_2 filled glove box; (b) a spin coater for solution processing; (c) a power supply in the glove box, to control the drying condition under electric field; and (d) a vacuum evaporation system with a copper feed-through.

3.2 DEVICE CHARACTERIZATIONS

The organic photovoltaics are mainly evaluated by measuring the current density-voltage (J-V) characteristics (**Figure 3.2a**). A J-V characteristic is a relationship between the current through a device and the corresponding voltage across it. The J-V characteristics were carried out under AM1.5G illumination at 100 mW/cm^2 (SAN-EI Electric XEC-301S solar simulator, 300W Xe Lamp JIS Class AAA; beam size: 4 inch diameter). The operational parameters of organic photovoltaics, such as open circuit voltage, short circuit current, fill factor, and power conversion efficiency, can all be obtained from the measurements.

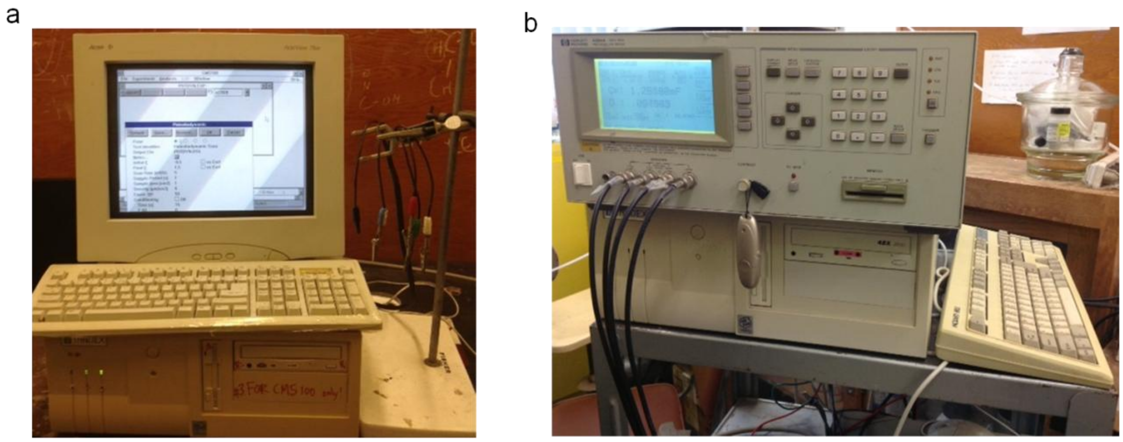

Figure 3.2 The measurement systems: (a) for the current density-voltage characteristic, and (b) for impedance spectroscopy.

Other characterization techniques, such as impedance spectroscopy (**Figure 3.2b**), atomic force microscopy, transmission electron microscopy, and x-ray diffraction, are used to examine the nanoscale morphological changes of the active layers, in order to support the enhanced device performance.

Chapter 4. IMPROVING THE EFFICIENCY

4.1 INTRODUCTION

OPV devices have been actively studied for better device performance. Although a number of treatments have been tested by empirical trial-and-error, the question still remains whether they offer optimized performance. Beyond these treatments, the application of a DC field was employed. However, the performance improvement was found to be less than satisfactory, due possibly to the fact that the non-polar structures are not responding effectively to DC field. These led us to propose the PCE enhancement by AC field, to align the p/n polymers during the device fabrication.

4.2 PAPER 1: EFFICIENCY IMPROVED BY AC FIELD (APPL. PHYS. LETT. 99, 053305 (2011))

Organic photovoltaic power conversion efficiency improved by AC electric field alignment during fabrication

Cindy X. Zhao,[1] Xizu Wang,[2] Wenjin Zeng,[2] Zhi K. Chen,[2] Beng S. Ong,[2,3,4] Kewei Wang,[1] Lulu Deng,[1] and Gu Xu[1,a)]

[1]*Department of Materials Science and Engineering, McMaster University, Hamilton, Ontario, Canada L8S4L7*

[2]*Institute of Materials Research and Engineering, Singapore 117602*

[3]*Institute of Manufacturing Technology, Agency for Science, Technology and Research, Singapore*

[4]*School of Chemical and Biomedical Engineering, Nanyang Technological University, Singapore*

a) Electronic mail: xugu@mcmaster.ca

(Received 8 April 2011; accepted 16 July 2011; published online 4 August 2011)

Ultra-low frequency AC field was employed to align p/n polymers during organic photovoltaic device fabrication. The resulting devices show 15% increase in power conversion efficiency and four-fold increase in parallel resistance. Supported by the transmission electron microscopy and atomic force microscopy images, the performance enhancement is attributed to the optimized morphology and enlarged p/n interface by AC field, which is more effective than DC, possibly explained by the argument of better mixing via back-and-forth shaking than a single swing. *©2011 American Institute of Physics.* [doi:10.1063/1.3623477]

Organic photovoltaic (OPV) devices have been actively studied due to the possible advantages of large area fabrication and low cost solution processing.[1,2] Among them, bulk heterojunction (BHJ) based polymer solar cells, made of poly (3-hexylthiophene) and [6,6]-phenyl-C61-butyric acid methyl ester (P3HT:PCBM) blend, have been well investigated and reached reasonable level of power conversion efficiency (PCE).[3] To obtain better PCE values, it is the best to arrange the p-type donor and n-type acceptor to form an interpenetrating bicontinuous network, which maximizes the p/n interfacial areas.[4] However, this is found to be difficult to achieve, since there is phase segregation of the polymer blend in the lateral and perpendicular directions.[4,5] Therefore, it is crucial to find an effective way of controlling the blend morphology, to in turn enhance the PCE of polymer solar cells.

Although a number of treatments have been tested, such as the choice of solvents,[6,7] control of drying,[8] thermal annealing,[9,10] and vapor annealing,[11] the question still remains whether they offer optimized performance. Beyond these treatments, the application of a DC field was employed during the spin-coating process,[12–14] involving a field strength up to 10^3 V/cm. However, the performance improvement was found to be less than satisfactory, due possibly to the fact that the non-polar structures are not responding effectively to DC field. In addition, it is too early for the polymers to form desired structure during the spin-coating process. Post-production DC electric field treatment, which has also been suggested,[15–17] needs to be performed at elevated temperatures, which severely limits the application to certain electrode systems not affected by the heating.

These led us to propose the PCE enhancement by AC field, to align the p/n polymers during the device fabrication. The rationale is, for non-polar structures, AC field has been found to be much more effective than the DC, which was applied to similar systems found in, e.g., proton exchange membrane fuel cells.[18,19]

It is therefore the purpose of this report to investigate BHJ devices aligned by AC electric field, with a “floating” electrode during the drying stage, right after the spin-coating process. Much higher field strength, up to 10^5 V/cm was used, while ultra-low frequency, down to a few minutes per cycle, was employed. It is found that the AC field aligned devices show about 15% increase in PCE, and among other improved parameters, four-fold increase in parallel resistance defined for the equivalent circuit model is the most noticeable. The performance enhancement obtained is attributed to the more optimized blend morphology and enlarged p/n interfacial areas, which is directly supported by the transmission electron microscopy (TEM) and atomic force microscopy (AFM) images.

The devices were prepared on ITO patterned glass substrates (thickness of ITO~150 nm). The ITO substrates were cleaned, and then blow dried. The substrates were subject to ozone plasma treatment for 10 min, followed by spincoating a 40 nm thick film of poly(3,4-ethylenedioxythiophene):polystyrenesulfonate (PEDOT:PSS, Baytron P). The PEDOT:PSS conducting layer was dried at 120 ^{o}C for 10 min in a glove box. A prepared polymer blend, consisting of P3HT (Rieke Metals) and PCBM (Nano-C) which were dissolved separately in 1,2-dichlorobenzene (DCB) solution with a weight ratio of 1:0.8, was then spin-coated on top.

The active layer was allowed to dry under the normal condition (2 h, N_2 atmosphere) or under AC electric field (~10^5 V/cm for 1 h, followed by zero field for another hour, N_2 atmosphere). They were then annealed at 120 ^{o}C for another 10 min. Finally, a Ca/Ag bilayer cathode was deposited onto the half-finished device by a vacuum evaporation system. The overall device structure thus becomes ITO/PEDOT:PSS/ P3HT:PCBM/Ca(10 nm)/Ag(100 nm), with an active area of 3×3 mm^2. As shown in **Figure 4.1**, comparison was made by the adjacent pixels with and without AC electric field on one single substrate, where an extra "floating" electrode made of the ITO glass was used to create an electric field up to 10^5 V/cm. The AC field was obtained by a bi-polar switch (**Figure 4.1**) manually operated, via a DC power supply of 165 V, which is applied to a gap of about 20–30 μm, sandwiching the p/n polymers. Ultra-low frequency of 10^{-3} Hz was used, due to the slow response of organic semiconductors in the solvent-containing environment.

The current density–voltage (J-V) characteristics were measured by AM1.5G illumination at 100 mW/cm^2 (SAN-EI Electric XEC-301S solar simulator). And half-finished devices without the cathode deposition, involving AC field alignment, were also used for TEM (Philip CM12) and AFM imaging (Multimode Digital Instruments). In particular, the specimens for TEM were prepared by floating the photoactive layer on water surface and transferring to a TEM grid.[20]

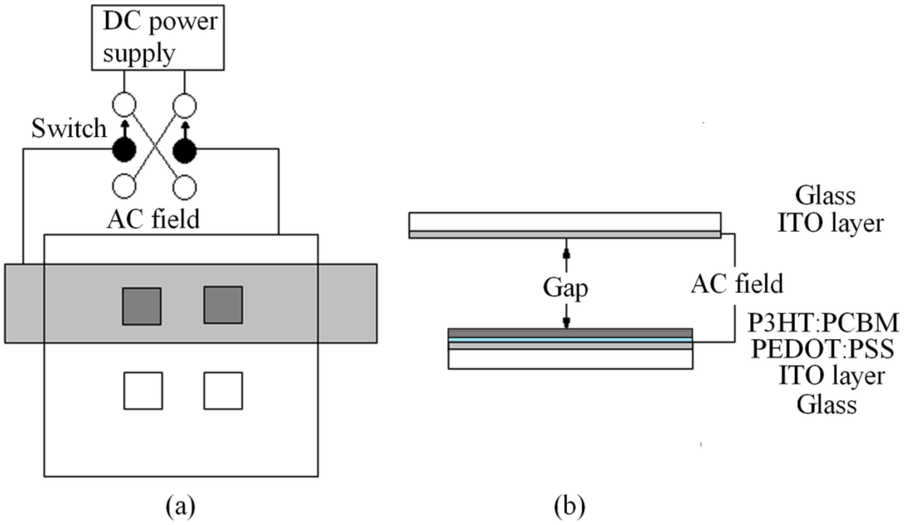

Figure 4.1 (a) OPV devices with and without AC field alignment, on a single substrate during the drying stage. (b) Cross-sectional view of AC aligned devices.

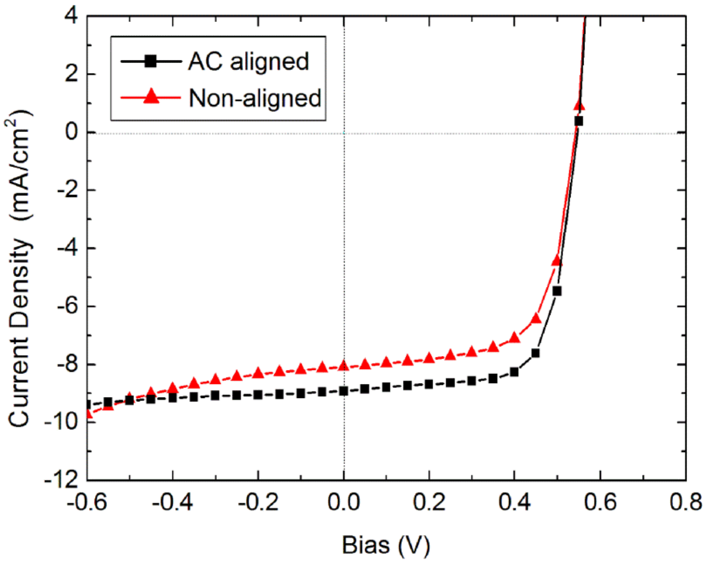

Figure 4.2 Experimental J-V characteristics for both devices with (squares) and without (triangles) AC field alignment under illumination.

Figure 4.2 shows the J-V characteristics under illumination for both devices with (squares) and without (triangles) AC electric field alignment. The squares are found to be located outside the triangles, indicative of a larger output, which gives obvious evidence that the AC aligned device out-performs the non-aligned. For the non-aligned device, the PCE was found to be 2.89%. Although not the best achieved before, it is within the typical range of P3HT:PCBM based devices.[6–11] For the AC electric field aligned device, however, a 15% increase of PCE to 3.41% was obtained. Correspondingly, compared with the non-aligned device, the short circuit current density (J_{sc}) increased from 8.08 mA cm^{-2} to 8.91 mA cm^{-2}, whereas the open circuit voltage (V_{oc}) stayed more or less the same level. These results were found to be repeatable by duplicated experiments.

According to the literature,[21] the overall performance of an OPV is reflected by PCE (η), which is given by

$$\eta = P_m/P_s = (J_m \times V_m)/P_s \qquad \text{(Eq. 4.1),}$$

where P_m is the maximum power output, P_s the incident light power density under standard test conditions, and J_m and V_m are the corresponding current density and voltage, respectively, at the maximum output. Since, in our case, the current density of the AC aligned device is larger, whereas the voltage is almost the same, the PCE enhancement found in the AC aligned device should mainly be attributed to the increased current density. Following the equivalent circuit analysis,[22] which consists of an ideal diode, a constant current source, a parallel resistor (R_p), and a series resistor (R_s), increase in parallel resistance or decrease in series resistance will both result in an increased current density. Data fitting was therefore performed, and the estimates of R_s and R_p were obtained from the inverse slopes of the forward and reverse characteristics, respectively.[23] The resulting coefficient of determination (R^2) was found to be larger than 0.95, showing excellent agreement between the experimental and fitting values, which are summarized in **Table 4.1**. For the AC field aligned device, the series resistance is smaller than that of the non-aligned, whereas the parallel resistance is 4 times larger. Both give rise to a higher current density for the AC field aligned.

Table 4.1 Summary of operational parameters for OPV devices with and without AC field alignment.

	Voc (V)	Jsc (mA/cm^2)	FF (Fill Factor)	PCE (%)	Rs (Ω cm^2)	Rp (Ω cm^2)
Non-aligned	0.54	8.08	0.66	2.89	1.68	296
AC aligned	0.55	8.91	0.70	3.41	1.47	1231

To answer the question of why the AC field alignment increases the current density, thus improving the device performance, morphological studies on the P3HT:PCBM active layer were carried out using TEM and AFM. Bright-field (BF) TEM images of P3HT:PCBM films with and without AC field alignment are shown in **Figure 4.3(a) and 3(b)**. P3HT crystals are relatively brighter in contrast to the background, due to its lower density (1.10 g/cm^3) compared to that of PCBM (1.50 g/cm^3).[24,25] Both the images show the PCBM-rich domains, recognized as the dark regions.[26] However, in the sample of AC field alignment, the area of dark regions becomes smaller, resulting from the better dispersed PCBM throughout the film. The difference between the two images suggests that a more uniform structure is formed under the AC alignment, which lowers the internal energy loss, caused by the recombination of charges, thus increasing the parallel resistance.[22,27] As shown by **Figure 4.4**, the 3D image of the AC field aligned device show a smoother surface with mounds and valleys of smaller width compared to the non-aligned. In the mean time, the roughness of the AC aligned is much smaller. For the AC aligned device, the decrease in series resistance is also attributed to the smoother morphology, which increases the contact area between cathode and active layer, thus providing better conduction path.[28,29] Furthermore, a smoother surface results in a larger effective area for the AC aligned polymeric active layer, which implies that the AC field may align the p/n polymers to enlarge the p/n interface. This is critical during the photocurrent generation. A photon is absorbed to create an exciton which then diffuses to the p/n interface, followed by exciton separation achieved by the internal electric field.

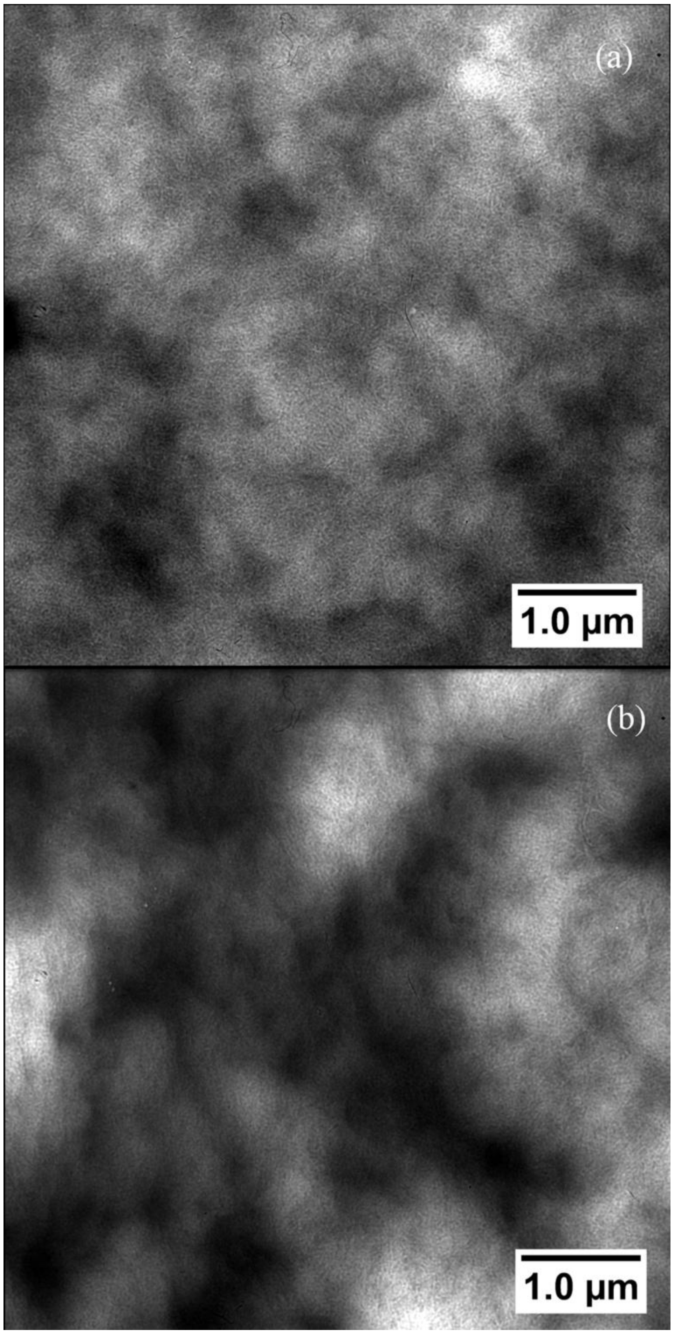

Figure 4.3 TEM images of P3HT:PCBM films with (a) and without (b) AC field alignment. The scale bars on the bottom right are 1 μm for both images.

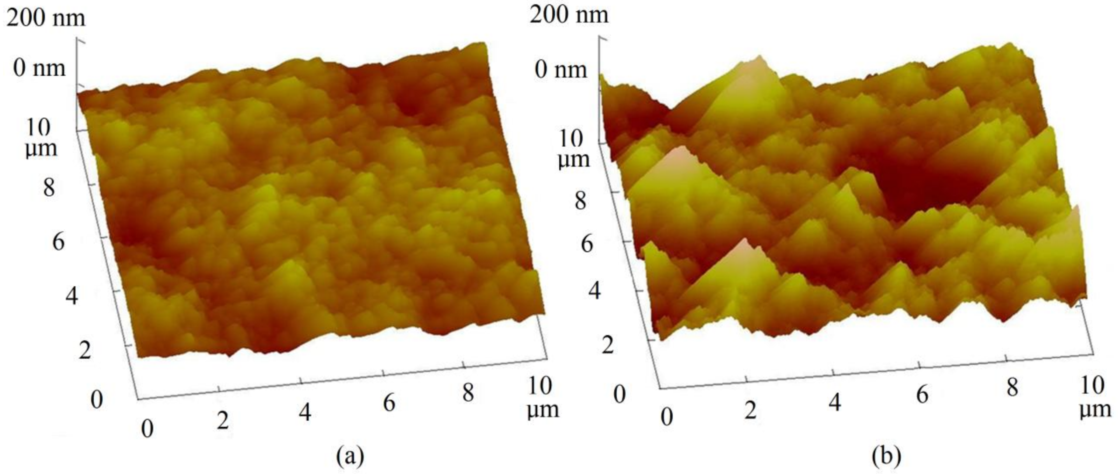

Figure 4.4 Effect of AC field alignment on the morphology of the OPV active layer. 3D AFM images of P3HT:PCBM films with (a) and without (b) AC field alignment show a 10 µm × 10 µm surface area.

Finally, the separated holes or electrons transport through donor or acceptor phase to the electrodes instead of recombination. Following this analysis, an enlarged p/n interfacial area helps to enhance excition separation and charge generation, leading to an increased current density. The TEM and AFM images thus provide support to the more evident PCE increase obtained by the AC field alignment, compared with the DC field. This may be understood by the following argument: a better mixing is achievable by shaking a stick-containing box back-and-forth, than by a single swing. In the meantime, the frequency should be low enough for the sticks to follow the shake. Therefore, AC field is more effective than DC in our case, where the resulting distribution of aligned polymers becomes more uniform and p/n interfacial area gets enlarged. Further optimization may still be needed to achieve better enhancement results.

To conclude, ultra-low frequency AC electric field has been found to improve the device performance by aligning the p/n polymers, to optimize blend morphology and enlarge the p/n interfacial areas. Among the operational parameters, the four-fold increase in parallel resistance by AC alignment is the most noticeable, which lowers the internal energy loss caused by recombination and increases the current density, and thus enhances the device efficiency. Moreover, it has been shown that AC field is more effective in aligning p/n polymers than the DC, which hopefully offers an alternative to further enhance the OPV device efficiency.

REFERENCES

[1] N. S. Sariciftchi and H. Hoppe, J. Mater. Res. **19**, 1924 (2004).

[2] T. L. Benanti and D. Venkataraman, Photosynth. Res. **87**, 73 (2006).

[3] W. Ma et al., Adv. Funct. Mater. **15**, 1617 (2005).

[4] Z. Xu et al., Adv. Funct. Mater. **19**, 1227 (2009).

[5] M. Campoy-Quiles et al., Nature Mater. **7**, 158 (2008).

[6] G. Yu et al., Science **270**, 1789 (1995).

[7] Y. Kim et al., Appl. Phys. Lett. **86**, 063502 (2005).

[8]G. Li et al., Nature Mater. **4**, 864 (2005).

[9]H. Hoppe and N. S. Sariciftchi, J. Mater. Chem. **16**, 45 (2006).

[10]D. Chirvase et al., Nanotechnology **15**, 1317 (2004).

[11]Y. Zhao et al., Appl. Phys. Lett. **90**, 043504 (2007).

[12]H. Jin et al., Solid State Commun. **140**, 555 (2006).

[13]Q. Shi et al., Chem. Phys. Lett. **425**, 353 (2006).

[14]T. L. Lim et al., Chem. Phys. Lett. **432**, 564 (2006).

[15]Y. Li et al., Synth. Met. **158**, 190 (2008).

[16]A. K. Pandey et al., Org. Electron. **8**, 396 (2007).

[17]F. Padinger et al., Adv. Funct. Mater. **13**, 85 (2003).

[18]Z.-T. Wang et al., J. Power Sources **186**, 293 (2009).

[19]E. Middelman, Fuel Cells Bull. **2002**, 9 (2002).

[20]W. Ma, C. Yang, and A. J. Heeger, Adv. Mater. **19**, 1387 (2007).

[21]J. Nelson, The Physics of Solar Cells (Imperial College, London, 2003).

[22]S. Yoo, B. Domercq, and B. Kippelen, J. Appl. Phys. **97**, 103706 (2005).

[23]S. Choi et al., J. Appl. Phys. **106**, 054507 (2009).

[24]C. W. T. Bulle-Lieuwma et al., Appl. Surf. Sci. **547**, 203 (2003).

[25] X. Yang et al., Macromolecules **37**, 2151 (2004).

[26] X. Yang et al., Nano Lett. **5**, 579 (2005).

[27] P. Junsangsri and F. Lombardi, Electron. Lett. **46**, 21 (2010).

[28] A. Kumar et al., Nanotechnology **20**, 165202 (2009).

[29] W. J. Potscavage et al., Acc. Chem. Res. **42**, 1758 (2009).

Chapter 5. STUDYING THE NANOSTRUCTURE

5.1 INTRODUCTION

The nanostructure changes in OPVs by AC electric field alignment need to be investigated, in order to have a complete understanding of the energy efficiency improvement in OPVs. Although TEM and AFM were able to offer a 2D view over the thin film device, it is not possible to assess the nanostructure in 3D, since in-situ TEM observation cannot be performed without substrate removal, and AFM can only show the surface morphology. Therefore, 2D X-ray diffraction has been proposed, to track the nanostructures of the polymers in 3D.

5.2 PAPER 2: DUAL NANOSTRUCTURES (THIN SOLID FILMS 520, 5770 (2012))

Dual Nanostructures in Poly (3-hexylthiophene) based Organic Photovoltaics under AC Electric Field

Cindy X. Zhao[a, *], Kewei Wang[a], James F. Britten[b], Matthew Zhi[a], Xizu Wang[c], Zhi K. Chen[c] and Gu Xu[a, *]

[a] *Department of Materials Science and Engineering, McMaster University, 1280 Main Street West, Hamilton, Ontario, Canada L8S4L7*

[b] *Department of Chemistry and Chemical Biology, McMaster University, 1280 Main Street West, Hamilton, Ontario, Canada L8S4M1*

[c] *Institute of Materials Research and Engineering, Singapore 117602*

Two-dimensional X-ray diffraction was employed, to provide a complete understanding of the energy efficiency improvement of organic photovoltaics by AC electric field alignment. Two distinguishable poly (3-hexylthiophene) (P3HT) nanostructures were found in the form of two separated layers, one of which is highly oriented and the other randomly distributed. The finding helps to analyze the crystallite arrangements not only in the interface in the bulk heterojunction, but also those closer to the substrate. The highly oriented P3HT layer, although located near the substrate, was found to enhance the device efficiency, by increasing the short circuit current and decreasing the series resistance.

Keywords: X-ray Diffraction, Organic Photovoltaic Device, Nanostructure

* Corresponding authors. Tel.: +1-905-525-9140 ext.27341.
E-mail addresses: zhaox8@mcmaster.ca (C. X. Zhao), xugu@mcmaster.ca (G. Xu).

1. Introduction

Organic photovoltaic devices (OPVs) have been widely studied over the past two decades, due to the possible advantages they provide, such as large area fabrication, lightweight construction and low cost solution processing [1, 2]. Among the existing OPV architectures, bulk heterojunction (BHJ) based polymer solar cells, consisting of a blend of poly (3-hexylthiophene) (P3HT, $(C_{10}H_{14}S)_n$) and [6,6]-phenyl-C61-butyric acid methyl ester (PCBM, $C_{72}H_{14}O_2$), have been extensively investigated, and become the most popular system, due largely to the reasonable level of power conversion efficiency (PCE) [3]. In order to further improve the PCE values, approaching that of the silicon based photovoltaics, it has been suggested to construct a three dimensional (3D) interpenetrating bicontinuous network of the electron donors and electron acceptors, to maximize the p/n interfacial areas and thus optimize charge extraction from the device [4]. However, this optimized morphology is difficult to achieve, since in the active layer there exists phase segregation of both components, the scale of which is much larger than the exciton diffusion length, jeopardizing the total exciton harvesting [4, 5]. Therefore, it is very necessary to find an effective way of controlling the bulk morphology and interfacial areas, in order to promote the PCE of polymer solar cells. Although improvement has been made by varying the combinations of materials, processing methods and other parameters [6-11], the PCE is still far behind that of Si-based photovoltaics. Therefore, the question still remains with respect to the optimal p/n interfacial structure in order to achieve better energy efficiency.

As an attempt to answer the question, electric field alignment has been utilized during device fabrication, and the effect on the film nanostructure and device properties such as mobility was observed [12, 13]. The application of the electric field has led to an enhanced room temperature mobility by eliminating nanometer-sized crystal formation [12, 13]. It was found recently that the BHJ devices aligned by AC electric field during fabrication, may provide up to about 15% increase in PCE, derived from the short circuit current (J_{sc}) increase and parallel resistance (R_p) increases, as well as the drop of series resistance (R_s) [14]. That PCE enhancement was attributed to a more uniform structure and enlarged p/n interfacial areas obtained under AC electric field alignment, based on the transmission electron microscopy (TEM) and atomic force microscopy (AFM) observations [14]. Although these methods were able to offer a two dimensional (2D) view over the thin film device, it is not possible to assess the nanostructure in 3D, since in-situ TEM observation cannot be performed without substrate removal, and AFM can only show the surface morphology.

To resolve these issues, 2D X-ray diffraction (XRD) has been proposed, to track the P3HT nanostructures in 3D. Previous examples of using XRD in a related setting can be found from, e.g., the work by Ober et al. [15], which provided clear images of how the structure and orientation of the liquid crystals changed under AC electric field. XRD has also been used in OPV studies, e.g., to obtain P3HT crystallinity, the increase of which was found to be responsible for the PCE improvement, based on certain processing methods [8, 16-18]. Both scattering intensities of P3HT and PCBM have then been taken into account, but the discussion about their correlation has been limited to the J_{sc} so far

[19]. Similar work has also been done in the area of the organic thin film transistor, where the effect of PCBM weight ratio on the molecular orientation and electrical performance of the P3HT/PCBM thin film was examined by XRD [20].

It is therefore the purpose of this report, to study the nanostructure and orientation of the polymers using XRD, for the P3HT/PCBM based OPVs. In particular, comparison will be made for the nanostructures with and without AC electric field alignment. Two distinguishable P3HT nanostructures were found to be distributed as two separated layers, which were not observed by TEM or AFM. One is highly oriented, located right on top of the pre-coated indium tin oxide (ITO) substrate, and the other randomly distributed, forming the bulk network with PCBM: the BHJ. The finding helps to analyze the arrangements of P3HT and PCBM crystallites, not only in the interfacial areas in the BHJ, but also those closer to the substrate. Combined with TEM and AFM results, the XRD experiments provide a complete explanation of why the device performance improves under AC electric field alignment. The highly oriented P3HT layer played an important role, in enhancing the device efficiency, via J_{sc} increase and Rs drop.

2. Experimental details

The samples were prepared on pre-cleaned ITO patterned glass substrates (thickness of ITO ~150 nm, sheet resistance ~12Ω/square), which were subject to ozone plasma treatment for 10 minutes before the solution process. A 40 nm thick conducting layer, made of poly(3,4- ethylenedioxythiophene):polystyrenesulfonate (PEDOT:PSS, Baytron P), was spin-coated first, and dried at 120 ℃ for 10 minutes in a glove box filled with N_2 atmosphere. An active layer, consisting of P3HT (Rieke Metals, average molecular weight: 50,000 g/mol, polydispersity index: 2.1, regioregularity: >90%) and PCBM (Nano-C) dissolved separately in 1,2-dichlorobenzene solution with a weight ratio of 1:0.8, was then spin-coated on top, followed by the drying stage, either under the normal condition (2 hours, N_2 atmosphere), or under AC electric field (~5.5-8.25*10^4 V/cm for one hour, followed by zero field for another hour, N_2 atmosphere). Finally, the pre-annealing was carried out at 120 °C for another 10 minutes. The sample structure thus becomes: ITO/PEDOT:PSS /P3HT:PCBM.

As shown in **Figure 5.1**, a direct comparison was made by the adjacent pixels with and without AC electric field on one single patterned substrate. The AC electric field was achieved by a bi-polar switch manually operated at a frequency of 10^{-3} Hz, and a DC power supply of 165 volts applied to a gap of 20-30 μm, which was obtained by the sample ITO substrate and another ITO glass sat on top [14]. The gap was well controlled, to avoid any damage to the active layer, caused by its direct contact with the upper ITO glass. The application of the ultra low frequency AC electric field, rather than DC, has its advantages. For the non-polar structures, AC field has been found to be much more effective, which was applied to similar systems found in, e.g. proton exchange membrane fuel cells [21, 22]. What they also found was, the lower the frequency, the better the performance.

The samples with and without AC electric field alignment were used for both AFM (Multimode Digital Instruments, tapping mode, with an n-type silicon tip from Nanosensors) and 2D XRD experiments (Bruker Smart 6000 CCD 3-circle D8 diffractometer, with a Cu rotating anode (Rigaku Ru200) parallel focused X-ray source of 1.5418 Å), performed at room temperature. In particular, XRD measurement was carried out, with the incident X-ray angle, the goniometer position, and the distance between the 2D detector and sample mount set to be 2 °, 90 ° and 15 cm, respectively.

The crystallinity was calculated by the 'external method' in the GADDS software (Bruker Analytical X-ray Systems Inc.). By determining the boundaries of the amorphous region and crystalline region, with the same 2θ limits and different χ range, the GADDS software calculates the crystallinity by employing specified areas of frame data.

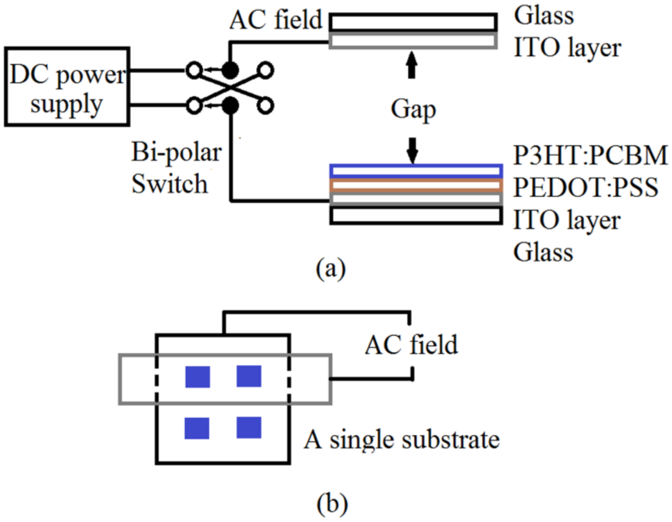

Figure 5.1 (a) Cross-sectional view of the AC electric field application. The top ITO glass was used as the "floating" electrode. (b) Top view of OPV devices with and without AC field alignment, on a single substrate during the drying stage.

The operational parameters for OPV devices with and without AC field alignment were measured by air mass 1.5 global illumination at 100 mW/cm^2 (SAN-EI Electric XEC-301S solar simulator, 300W Xe Lamp JIS Class AAA; beam size: 4 inch diameter). The completed devices with the vacuum deposited Ca(10 nm)/Ag(100 nm) bilayer cathode were used. 5 sets of samples were utilized for data analysis. Each set contains two kinds of devices, prepared with and without electric field.

3. Results and Discussion

The PEDOT:PSS pre-coated ITO glass substrate shows no peak, except for the two peaks appearing at 2θ of 30.2° and 30.6°, arising from the (003) and (12-1) lattice planes of ITO, respectively, which indicates substantial amorphous nature of the PEDOT:PSS film. Similar results were also obtained by different research groups [23, 24]. **Figure 5.2** presents the two-dimensional X-ray diffraction patterns on 150 nm thick P3HT/PCBM active layers, deposited on an ITO glass pre-coated with non-crystalline PEDOT:PSS, with (2a) and without (2b) AC electric field alignment. The 2θ angle increases radially from the center to the left, and the χ angle varies along each semi circle from 180 ° on the top to 360 ° at the bottom. Both frames show diffraction spots or rings, from the (100) lattice planes of P3HT at 2θ of 5.6°, and PCBM at 2θ of 21.4°, corresponding to the d-spacing of 16.1 Å and 4.2 Å, respectively. Very weak (200) signals of P3HT can be observed at 2θ of 11.2°. All the reflections of P3HT and PCBM have been labeled for clarity. For both **Figure 5.2a** and **Figure 5.2b**, the (100) reflections of P3HT are much stronger at the centre, with a χ spread of ~80°, suggesting that P3HT

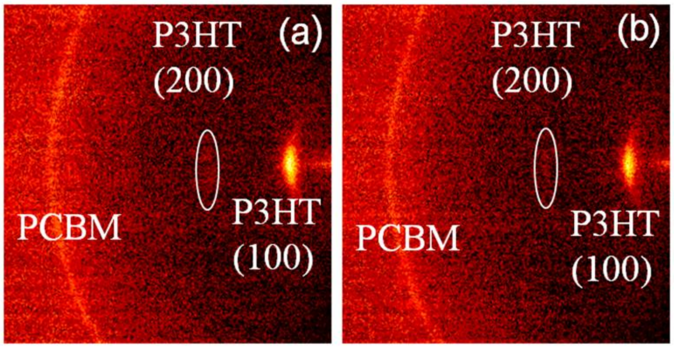

Figure 5.2 2D-XRD frames, obtained from the P3HT/PCBM samples with (a) and without (b) AC electric field alignment. All the reflections have been labeled for clarity. A ring was drawn to help highlight the P3HT (200) reflection.

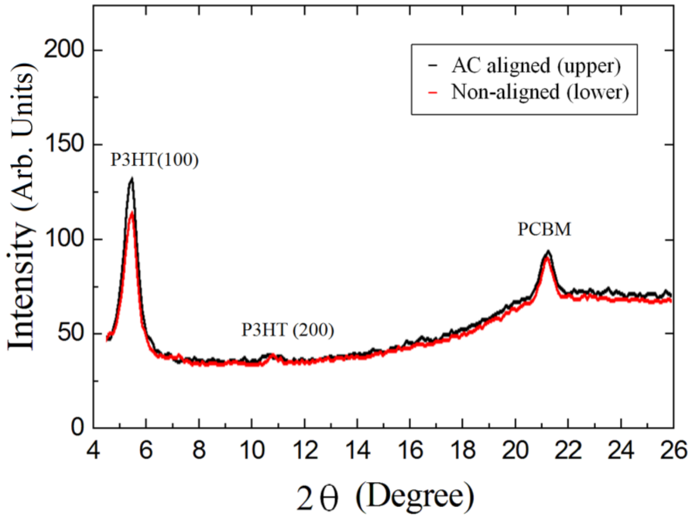

Figure 5.3 Diffraction intensity vs. 2θ plot, of the P3HT/PCBM samples with and without AC electric field alignment. The peak heights are 134±5 arb. units and 116±5 arb. units, for the samples with and without AC electric field alignment, respectively.

has a certain texture; the PCBM crystallizes randomly without a preferred orientation, however, as evidenced by its evenly distributed semi-circle shown in the frames.

To study the crystal information, the intensity vs. 2θ plot (**Figure 5.3**) was obtained by integrating χ from 180° to 360° for **Figure 5.2**. The (100) reflection of P3HT and that of PCBM are plotted, giving 2θ widths of 1.2° and 0.7°, respectively. They are almost the same, for the sample aligned with AC electric field, and the one without. Although the reflection intensities of the PCBM and all the peak positions remain the same for both samples with and without AC electric field, the (100) reflection of P3HT is found to be more intense for the sample subjected to AC electric field. Correspondingly, the P3HT crystallinity increased from 66.91%±2.33% to 73.45%±2.66%, calculated by GADDS software for 5 sets of the AC electric field aligned samples; whereas the average crystallite size stayed more or less the same at 15 nm, calculated by Debye-Scherrer formula [25].

The magnitude of the crystal size is comparable to the exciton diffusion length of ~ 10 nm in P3HT [26], as well as to the P3HT domain size, found in efficient OPV devices by TEM [27], implying efficient charge harvesting is possible in both devices with and without AC field alignment. Because of the similarity in the crystal size, the P3HT crystallinity increase can only be attributed to higher crystallite numbers, increased by the AC electric field alignment. This is consistent with what was found in the literature [8, 16-18], where the enhanced device performance can sometimes be explained by the increased P3HT crystallinity, which therefore constitutes part of the reason of why there is a 15% PCE increase in the AC electric field aligned device [14]. The detailed variations in crystallinity and crystal size may be somewhat different from the existing literature, which was mostly obtained by DC electric field, whereas an AC field has been employed here.

To analyze the orientation of P3HT in the active layer, its (100) pole figure was obtained by plotting the diffraction versus χ and φ, while fixing the 2θ at the peak of P3HT (100) reflection, while the φ angle varies along each circle, and χ increases along the radial direction in the (χ, φ) plane. For both pole figures with (**Figure 5.4a**) and without (**Figure 5.4b**) AC electric field alignment, the intensities have a centro-symmetrical shape, indicating that the P3HT crystallites have a preferred orientation, with the [100] axis parallel to the substrate normal.

However, this seemingly well-defined single peak in the pole figure, is surprisingly found to be made of two distinguishable peaks superimposed onto each other, as shown by the χ vs. intensity curves, plotted in **Figure 5.5**. Obviously, they have very different peak widths, signifying two distinguishable nanostructures, one of which is highly oriented along the substrate normal, with a full width at half-maximum (FWHM) of ~2 °, and the other a very random distribution, with a FWHM of ~20 °. It is evident that these two different nanostructures, both occupying a certain volume, do not coincide with each other in the same location in the real space- it would be impossible to form the respective crystalline structures otherwise- although they sit on top of each other in the reciprocal space. This is similar to a hypothetical sample, where both tetragonal and hexagonal crystals coexist, would produce two sets of corresponding diffraction peaks. But locally the two crystals should not be located at the same position in the real space.

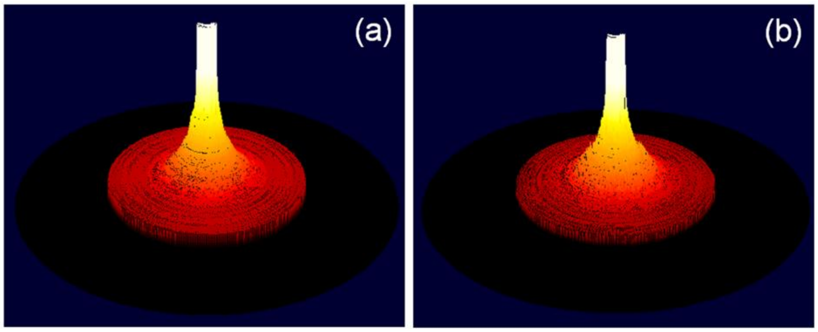

Figure 5.4 The pole figures for the (100) planes of P3HT, obtained from the P3HT/PCBM samples with (a) and without (b) AC electric field alignment.

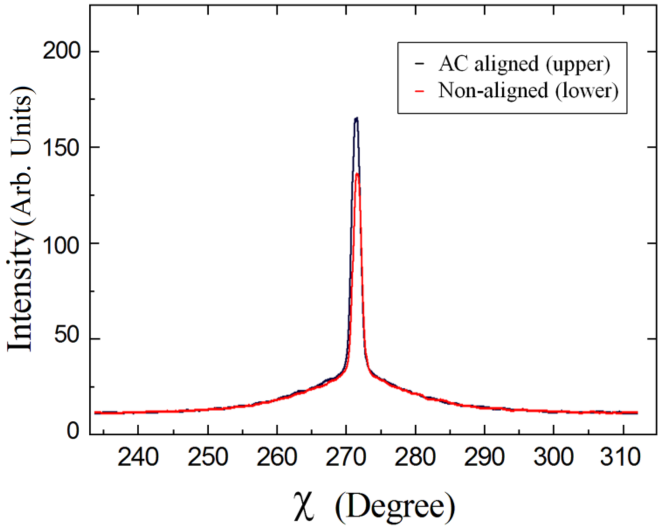

Figure 5.5 Diffraction intensity vs. χ plot, of the P3HT/PCBM samples with and without AC electric field alignment. The signals from two different regions form a sharp peak with a FWHM of ~2°, as well as a broad peak with a FWHM of ~20°, respectively. The peak heights are 167±6 arb. units and 137±5 arb. units for the samples with and without AC electric field alignment, respectively.

The question now becomes how these distinct nanostructures are distributed in the real space. Due to the centro-symmetrical pole figure, it is highly unlikely to have the two nanostructures occupying different areas along the substrate plane, although the beam spot of the X-ray used has a diameter of 500 microns, much larger than the size of the nanostructures. Therefore, the only possibility remaining, is to have them forming two separated layers along the substrate plane, with one on top of the other. Since a highly oriented P3HT layer is unlikely to grow from a random P3HT base, the layer having a narrow peak is very likely to be formed directly on the substrate, followed by a more random layer. As illustrated by **Figure 5.6**, the arrangement of P3HT thus becomes: on top of the smooth non-crystalline PEDOT:PSS film, the highly oriented P3HT layer is laid first, followed by the randomized P3HT layer. Although it is possible to fit our experimental results by the picture of polymer globules with crystalline cores surrounded by disordered amorphous periphery, as observed by O'Neil et al. [28, 29], it only offers a contrast between the crystals and disordered amorphous periphery. Our model is thus more likely, since it can be used to specify the regions with different crystallite orientations, e.g. the highly oriented P3HT crystallite region, and the randomly distributed P3HT crystallite region. The thickness ratio of the highly oriented P3HT layer and randomly distributed layer is estimated to be 1/3, obtained from the areas of both diffraction peaks following the χ vs. intensity curves (**Figure 5.5**). Compared with that of the non-aligned curve (**Figure 5.5**), the area of the sharp peak, representing the highly oriented P3HT layer, is larger under AC electric field, resulting in an increased thickness of the highly oriented layer by AC electric field.

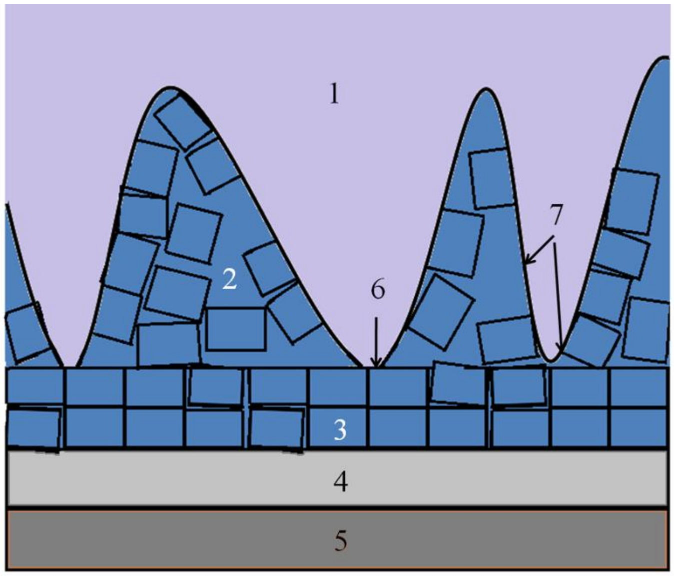

Figure 5.6 Schematic illustration of the dual nanostructure arrangements of P3HT. A highly oriented P3HT layer (3) is laid first, on top of the ITO substrate (5) pre-coated with PEDOT:PSS (4), followed by the randomized P3HT layer (2). The labels of 6 and 7 represent the diffusion pathways of PCBM (1) through the highly oriented P3HT, or the randomized P3HT, respectively.

Table 5.1 Summary of operational parameters for OPV devices with and without AC field alignment. The average and standard deviation values were calculated based on 5 sets of samples.

	Voc (V)	Jsc (mA/cm^2)	Fill Factor	PCE (%)	Rs (Ω cm^2)
Non-aligned	0.536 ±0.009	8.162 ±0.156	0.620 ±0.039	2.716 ±0.124	1.920 ±0.242
AC aligned	0.546 ±0.005	8.858 ±0.224	0.690 ±0.007	3.338 ±0.070	1.510 ±0.044

This proposed model was based purely on the diffraction results of P3HT without involving PCBM, and the location of PCBM is therefore rather arbitrary. Although the vertical phase separation of P3HT and PCBM in the blend film has been observed with various techniques [4, 5, 30, 31], there are opposite results towards the concentration profile of P3HT or PCBM near the metal electrode. Our XRD results indicate that there is a higher P3HT concentration adjacent to the PEDOT:PSS pre-coated ITO substrate, consistent with the work done by Kim et al. and Bavel et al. [30, 31]. In the meantime, our data indicates it is less likely to have the opposite picture in which PCBM dominates the region close to the substrate, due to the diffusion of PCBM molecules through the grain boundaries of P3HT crystallites, to the organic-PEDOT:PSS interface [5], forming the vertical phase segregation of the donor and acceptor materials in the blend film. After all, the resulting morphology of PCBM dominating the region close to the substrate and P3HT near the metal electrode, would not change the arrangement of the P3HT crystallites, since the onset of the diffusion of PCBM molecules is, apparently, linked to the polymer crystallization process.

The operational parameters for OPV devices with and without AC field alignment were summarized in **Table 5.1**. An increase of PCE to 3.338% was obtained for the AC electric field aligned device. The J_{sc} increased from 8.162 to 8.858 mA cm^{-2} by the AC electric field, whereas the open circuit voltage (V_{oc}) stayed almost the same level of 0.54 V. It is rather puzzling that, the scattering intensity of the highly oriented P3HT layer, represented by the sharp peak, has been enhanced under AC electric field alignment. This implies that the PCE increase was only caused by the highly oriented P3HT near the substrate, rather than by the more random part of P3HT, which is inconsistent with results from TEM [14] and AFM. Obviously, a more complete picture should also include what was observed by TEM and AFM, which were not picked up by XRD, due probably to the fact that the PCBM has always been randomly crystallized, and thus the randomness of the P3HT does not change much in the interfacial region. Both TEM and AFM indicate that the random part of P3HT is subjected to change during the AC field alignment; the TEM presents better dispersed PCBM and a more uniformed structure under AC field alignment [14], and AFM gives a different surface morphology, with mounds and valleys of smaller width, compared to that without AC field, as shown by **Figure 5.7**.

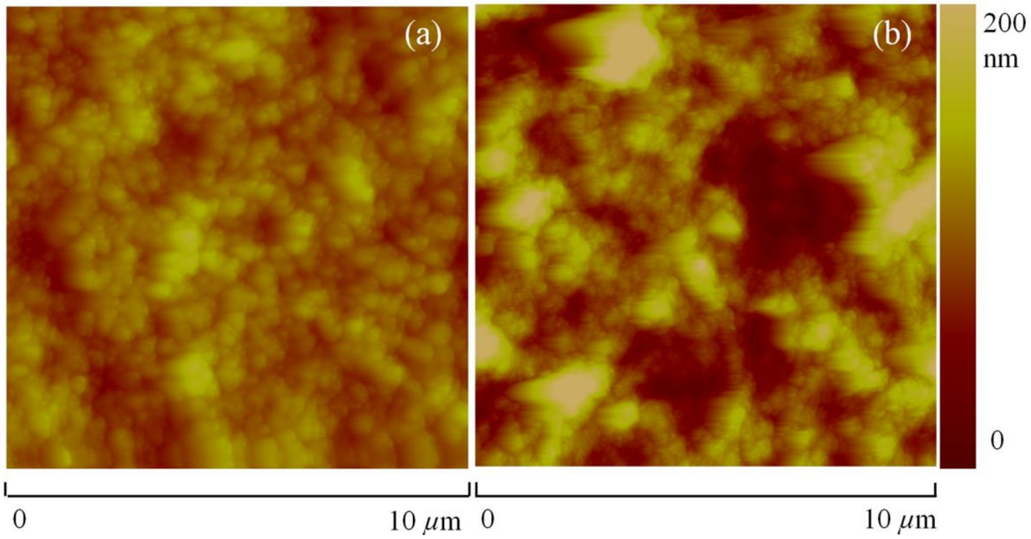

Figure 5.7 Effect of AC field alignment on the morphology of the OPV active layer. AFM height images of P3HT/PCBM films with (a) and without (b) AC field alignment show a 10 μm×10 μm surface area. The color scale for a and b is 0–200 nm.

Following the equivalent circuit analysis of OPV [32], which consists of an ideal diode, a current source, a parallel resistor and a series resistor, increase in R_p or decrease in R_s will both result in an enhanced device PCE. Therefore, in addition to the increased interfacial area in the BHJ [14], reflected by the results (**Figure 5.7**), the increased crystallinity and crystal numbers in the highly oriented P3HT layer may further enlarge the interfacial area with the PCBM closer to the substrate. In addition to the better conduction path between the metal cathode and active layer [14], the decrease of Rs as shown in Table I may also be caused by the increased crystallinity in the highly oriented P3HT layer, to enhance the intermolecular charge migration [18] and improve the conduction between the ITO substrate and active layer. Therefore, the device performance enhancement is also caused by the increased volume of the highly oriented P3HT layer, and a more complete explanation of the PCE can now be achieved.

4. Conclusions

To conclude, the XRD results show two distinguishable P3HT nanostructures distributed as two separated layers. One is highly oriented closer to the substrate, followed by a more randomized layer on top, forming the BHJ with PCBM, which were not observed by TEM or AFM. The finding helps to analyze the arrangements of P3HT and PCBM crystallites in the BHJ and those closer to the substrate, leading to a more complete understanding of how to enhance device performance. The highly oriented P3HT layer, although located near the substrate, played an important role in enhancing the device efficiency, by increasing Jsc and deceasing Rs.

Acknowledgments

The authors acknowledge the financial support of Natural Science and Engineering Research Council of Canada.

REFERENCES

[1] N.S. Sariciftci, H. Hoppe, J. Mater. Res. 19 (2004) 1924.

[2] T.L. Benanti, D. Venkataraman, Photosynth. Res. 87 (2006) 73.

[3] W. Ma, C. Yang, X. Gong, K. Lee, A.J. Heeger, Adv. Funct. Mater. 15 (2005) 1617.

[4] Z. Xu, L.-M. Chen, G. Yang, C.-H. Huang, J. Hou, Y. Wu, G. Li, C.-S. Hsu, Y. Yang, Adv. Funct. Mater. 19 (2009) 1227.

[5] M. Campoy-Quiles, T. Ferenczi, T. Agostinelli, P.G. Etchegoin, Y. Kim, T.D. Anthopoulos, P.N. Stavrinou, D.D.C. Bradley, J. Nelson, Nat. Mater. 7 (2008) 158.

[6] G. Yu, J. Gao, J.C. Hummelen, F. Wudl, A.J. Heeger, Science 270 (1995) 1789.

[7] Y. Kim, S.A. Choulis, J. Nelson, D.D.C. Bradley, S. Cook, J.R. Durrant, Appl. Phys. Lett. 86 (2005) 063502.

[8] G. Li, V. Shrotriya, J. Huang, Y. Yao, T. Moriarty, K. Emery, Y. Yang, Nat. Mater. 4 (2005) 864.

[9] H. Hoppe, N.S. Sariciftci, J. Mater. Chem. 16 (2006) 45.

[10] D. Chirvase, J. Parisi, J.C. Hummelen, V. Dyakonov, Nanotechnology 15 (2004) 1317.

[11] Y. Zhao, Z. Xie, Y. Qu, Y.a. Geng, L. Wang, Appl. Phys. Lett. 90 (2007) 043504.

[12] T.L. Lim, C.W. Chang, A.R. Inigo, Y.F. Huang, J.D. White, W. Fann, Chem. Phys. Lett. 432 (2006) 564.

[13] A.R. Inigo, C.C. Chang, W. Fann, J.D. White, Y.-S. HUANG, U.-S. Jeng, H.S. Sheu, K.-Y. Peng, S.-A. Chen, Adv. Mater. 17 (2005) 1835.

[14] C.X. Zhao, X. Wang, W. Zeng, Z.K. Chen, B.S. Ong, K. Wang, L. Deng, G. Xu, Appl. Phys. Lett. 99 (2011) 053305.

[15] H. Korner, A. Shiota, T.J. Bunning, C.K. Ober, Science 272 (1996) 252.

[16] H.-Y. Chen, H. Yang, G. Yang, S. S., R. Zadoyan, G. Li, Y. Yang, J. Phys. Chem. C. 113 (2009) 7946.

[17] C.W. Chu, H.C. Yang, W.J. Hou, J.S. Huang, G. Li, Y. Yang, Appl. Phys. Lett.92 (2008) 103306.

[18] T. Erb, U. Zhokhavets, G. Gobsh, S. Raleva, B. Stuhn, P. Schilinsky, C. Waldauf, C.J. Brabec, Adv. Funct. Mater. 15 (2005) 1193.

[19] E.D. Gomez, K.P. Barteau, H. Wang, M.F. Toney, Y.-L. Loo, Chem. Commun. 47 (2011) 436.

[20] K.A. Mohamad, N. Komatsu, K. Uesugi, H. Fukuda, Japanese Journal of Applied Physics 49 (2010) 04DK25.

[21] Z.-T. Wang, Y.-X. Wang, L. Xu, Q.-J. Gao, G.-Q. Wei, J. Lu, J. Power Sources 186 (2009) 293.

[22] E. Middelman, Fuel Cells Bulletin 2002 (2002) 9.

[23] C. Zhou, S. Wang, Q. Zhuang, Z. Han, Carbon 46 (2008) 1232.

[24] J. Li, J. Liu, C. Gao, J. Zhang, H. Sun, Int. J. Photoenergy 2009 (2009) 650509.

[25] B.D. Hall, D. Zanchet, D. Ugarte, J. Appl. Cryst. 33 (2000) 1335.

[26] D. Chen, A. Nakahara, D. Wei, D. Nordlund, T.P. Russell, Nano. Lett. 11 (2011) 561.

[27] W. Ma, C. Yang, A.J. Heeger, Adv. Mater. 19 (2007) 1387.

[28] K.D. O'Neil, O.A. Semenikhin, J. Phys. Chem. C. (2007) 14823.

[29] K.D. O'Neil, B. Shaw, O.A. Semenikhin, J. Phys. Chem. B 111 (2007) 9253.

[30] Y. Kim, J. Nelson, T. Zhang, S. Cook, J.R. Durrant, H. Kim, J. Park, M. Shin, S. Nam, M. Heeney, I. McCulloch, C.-S. Ha, D.D.C. Bradley, ACS Nano 3 (2009) 2557.

[31] S.S. van Bavel, E. Sourty, G. de With, J. Loos, Nano. Lett. 9 (2009) 507.

[32] J. Nelson, The Physics of Solar Cells, London : Imperial College Press, 2003.

Chapter 6. TRACKING THE DEGRADATION

6.1 INTRODUCTION

OPVs have been extensively studied for light-weight and low-cost solar cell applications. While their energy efficiency has been improved steadily, approaching the commercialization threshold of 10%, the poor stability of OPVs has long been recognized as the remaining obstacle, which is vital but not thoroughly investigated. The studies of degradation phenomena in OPVs, however, have been focused mainly on the individual components of OPV, although involving diverse characterization methods. Therefore, it becomes necessary to track simultaneous degradation of multiple interfaces, and to reveal the individual interface degradation without breaking the device.

6.2 PAPER 3: MULTI-INTERFACE DEGRADATION PROCESS (SUBMITTED)

Multiple-interface tracking of degradation process in organic photovoltaics

Cindy X. Zhao, Lucy L. Deng, Matthew Y. Ma, Joseph R. Kish, and Gu Xu*

Materials Science and Engineering, McMaster University, Hamilton, Ontario, L8S4L7, Canada

* xugu@mcmaster.ca, 1-905-525-9140 ext. 27341

The investigation of the stability in organic photovoltaics has been focused on individual components via localized and destructive analysis, which is limited to broken devices, instead of an operational OPV, and unable to obtain correlated information of degrading interfaces. DC biased AC impedance spectroscopy is employed here, to track multi-interface degradation without breaking the device. By varying DC bias, individual interface degradation is revealed via current density and capacitance versus voltage plots. It is found the degradation of p/n junction is mainly attributed to deteriorated morphology and oxidized polymers, whereas the semiconductor/metal interface changes by metal oxides as degradation products.

Organic Photovoltaics (OPVs) have been extensively studied for light-weight and low-cost solar cell applications [1,2]. While their energy efficiency has been improved steadily, approaching the commercialization threshold of 10% [3], the poor stability of OPVs has long been recognized as the remaining obstacle, which is vital to the commercialization but not thoroughly resolved [4]. For example, illumination and radiation have been discovered to induce degradation in OPVs [5,6], especially during the heating-cooling circles combined with humidity. Even when encapsulated and stored under darkness, the OPV devices still suffer from various forms of degradation[7]. These include indium diffusion [8], hole transport layer swelling [9], morphology changes [10,11], oxidation of organic semiconductors [12,13], carrier accumulation [14], and chemical degradation of metal electrodes [15,16]. Many of them are interrelated, and acting together on the irreversible deterioration in the light-absorption, exciton-generation, and charge-transporting properties [17].

The studies of degradation phenomena so far, however, have been focused mostly on the individual components of OPV, although involving diverse characterization methods. In particular, current density-voltage characteristic curve (J-V curve) has often been employed to evaluate the overall device degradation, but unable to observe the change of a single interface [4]. On the other hand, localized interface analysis, such as atomic force microscopy [17], scanning electron microscopy [18], only focuses on specified locations, which is limited to the broken devices, rather than an operational OPV, let alone the simultaneous monitoring of all degrading junctions and investigating their correlation. Therefore, the challenge remains, to simultaneously track the multiple interfaces of OPV degradation without breaking the device.

Here we present the investigation of multiple interface degradation in polymer/fullerene based OPVs, by DC biased AC impedance spectroscopy, under controlled environment, varying from vacuum to ambient. Transient techniques, such as impedance spectroscopy, charge extraction by linearly increasing voltage technique, have been used to determine the charge carrier concentration, mobility, lifetime and energy level in organic solar cells [19,20]. The oxidized active layer and metal oxidation between active layer/metal, were observed by impedance data from two sets of solar cells treated with various oxidant agents, which may provide the comparison between individual samples at a particular time [21]. In addition, the distinguishable semicircles in the impedance spectra were analyzed here, to directly obtain the separated interface information by this non-destructive method. The continuous degradation behavior is also monitored by the J-V curve of the p/n junction, isolated from the multiple interfaces, and interfacial capacitance versus voltage plot, obtained under scanned DC bias, which could not be extracted otherwise.

Poly(3-hexythlthiophene) (P3HT) and (6,6)-phenyl C_{61}-butyric acid methyl ester (PCBM) were purchased from 1-Material, and used as received. The bulk heterojunction (BHJ) device was prepared on the patterned ITO/glass substrate (15Ω cm^{-2}), which was pre-cleaned and treated with ozone plasma for 10 min before use. A 40 nm thick poly(3,4-ethylenedioxythiophene):poly(styrenesulfonate) layer (PEDOT:PSS, Sigma-

Aldrich) was spin-cast first, and dried at 120°C for 10 min in a glove box. The pre-dissolved P3HT and PCBM polymer blend in 1,2-dichlorobenzene solution (1:1 by weight, 20 mg mL^{-1}) was spin-coated directly on top of the PEDOT:PSS layer, with a thickness of 180-200 nm. A 100 nm thick Al electrode was thermally deposited through a shadow mask under a vacuum pressure of 10^{-9} atm, to define the active area of 5×5 mm^2. The overall device structure was thus: ITO/PEDOT:PSS/P3HT:PCBM/Al.

The DC biased AC impedance measurements (HP 4284A precision LCR meter) were carried out in the dark, and under selected vacuum pressures. The DC bias input varied from -0.6 to 0.6 V during the tests, and the AC oscillating amplitude was as low as 10 mV in order to maintain the linearity of the response. To avoid any possible influence of the ambient, the test under the vacuum pressure of 10^{-9} atm was done right after a device was fabricated, using pre-wired electric connections before electrode evaporation via the vacuum feed-through. The measurements continued with raising the vacuum pressure from 10^{-9} atm to 1 atm, by purposely admitting various amount of air into the vacuum chamber, as depicted in **Figure 6.1**.

The multiple interface degradation in the OPV device was investigated in-situ by the DC biased AC impedance spectroscopy, under controlled environment, which varies from vacuum to ambient. As shown in **Figure 6.2a and 2b**, the impedance data under each vacuum pressure were presented using Nyquist plot [22]. The fresh device under a pressure of 10^{-9} atm showed only one small semicircle along the real and negative imaginary impedance axes, revealing only a single p/n junction of the virgin OPV.

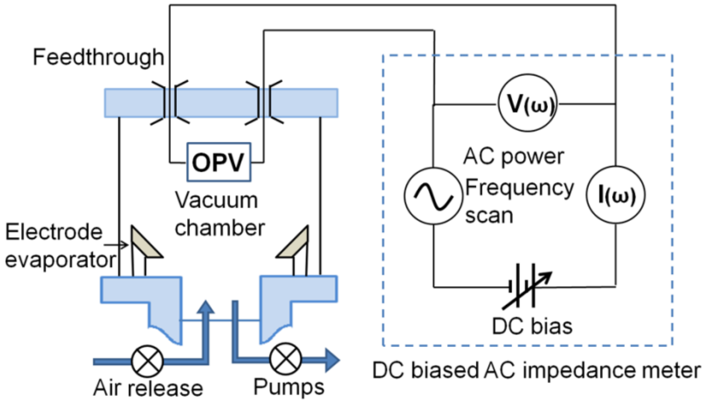

Figure 6.1 The experimental setup, involving a vacuum system for the electrode evaporation, as well as the “in situ” impedance measurement without breaking the device, performed under controlled environment, varying from vacuum to ambient.

In order to simulate the ppm level of oxygen in a typical glove box, the vacuum pressure was increased purposely to 10 $^{-5}$ atm. It was found that the intercept of the semicircle on the real impedance axis at high frequency end became larger, indicating an increase in the series resistance of the device under the exposure of oxygen, due possibly to the air encroached upon the PEDOT:PSS layer, thus worsened the electronic contact. From time-of-flight secondary ion mass spectrometry conducted by K. Norrman et al [23], oxygen was found to react mainly with PEDOT, at least with the sulfur functionality, and this hole transport layer suffered from a phase separation. As a consequence, PEDOT phase, which conducts the electrical current, becomes less shielded by PSS and more susceptible to oxygen, and the electron transport is therefore impeded. However, additional semicircle, signifying a new interface, began to appear at high frequency end in the

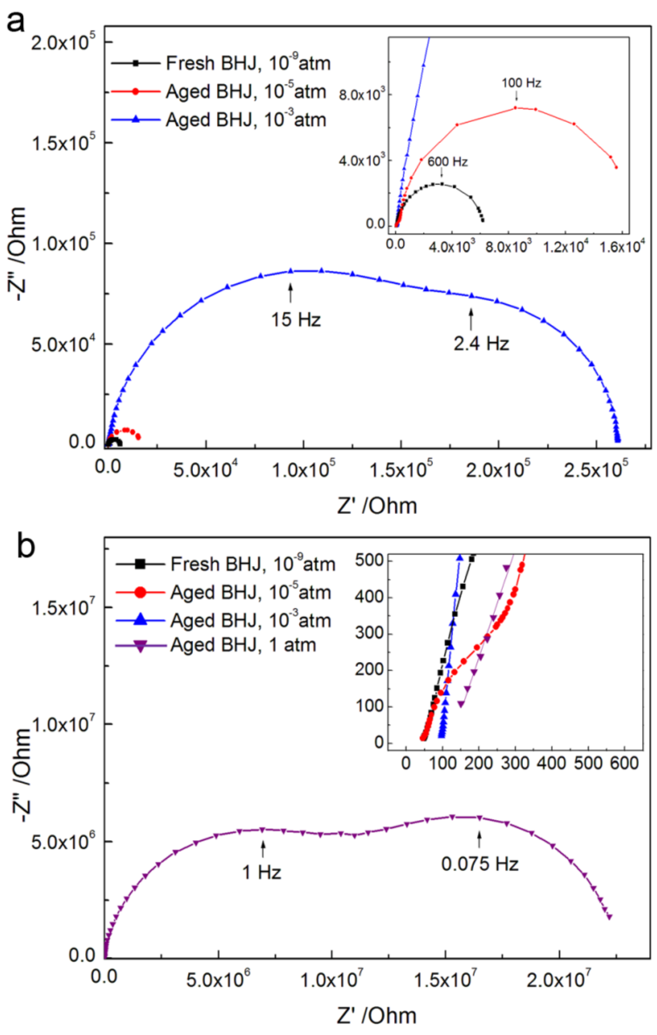

Figure 6.2 (a,b) Nyquist plot of the impedance data, averaged over 3-5 measurements, for zero bias voltage under the pressure of 10^{-9} atm to 1 atm in the dark. The OPV device gradually degraded with the rise of the vacuum pressure. The diameter and curve top frequency of semicircles under 10^{-9} and 10^{-5} atm were shown (2a, inset). The second semicircle was found to appear at high frequency end under 10^{-5} atm (2b, inset).

impedance spectra, accompanied by the increase in the semicircle radius from 10^3 to 10^4 Ω (**Figure 6.2a, 2b inset**). Upon the further increase of the pressure to 1 atm, this second semicircle became more evident, and eventually, the radius of each semicircle reached 10^7 Ω, when the device became malfunction. Individual interface in the aged devices was thus separated non-destructively by impedance spectra via distinguishable semicircles. In the meantime, the ambient degradation behavior was also observed by the increasing radius of each semicircle, and the drastic change of the complex plane spectra, in terms of the number of semicircles.

The semicircle in a Nyquist plot is usually characterized by a pair of a resistor and capacitor connected in parallel [22]. While the resistance, *R*, can be extracted from the diameter of the semicircle in the real axis, the capacitance, *C*, was calculated from the curve top frequency (Figure 2a), *f*, using $RC = (2\pi f)^{-1}$ [24]. Using the *R* and *C* obtained from each semicircle under scanned DC bias, the degradation behavior of each interface was investigated, in terms of both the interfacial capacitance versus voltage plot, and J-V curve of an isolated junction, under controlled environment.

For example, for the fresh OPV device, the capacitance-bias voltage (C-V) relation was plotted in **Figure 6.3**, showing the general pattern of a p/n junction for the electron donors and acceptors [25], where the forward bias side is dominated by the diffusion capacitance arising from the voltage lagging behind the current, and the reverse bias side by the junction capacitance due to the dipoles in the depletion zone [25,26]. For the aged device, there were two distinguishable semicircles, indicating two non-identical

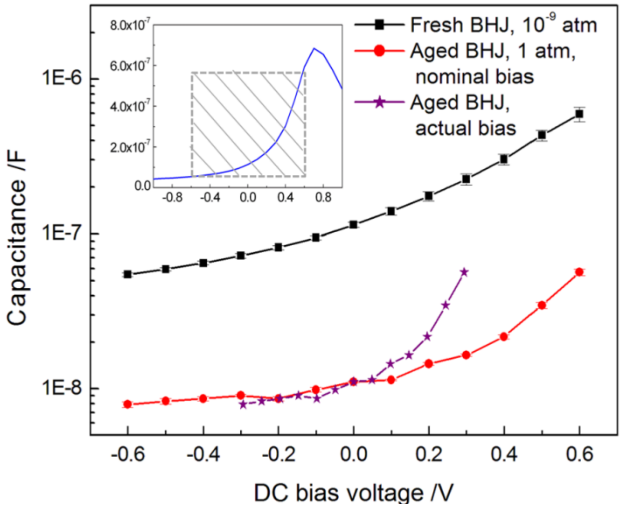

Figure 6.3 Capacitance versus bias voltage curves, obtained from the semicircle representing the P/N junction for both the fresh and aged devices. The capacitance was plotted under the DC bias of -0.6 to +0.6 V, necessary for the comparison (inset).

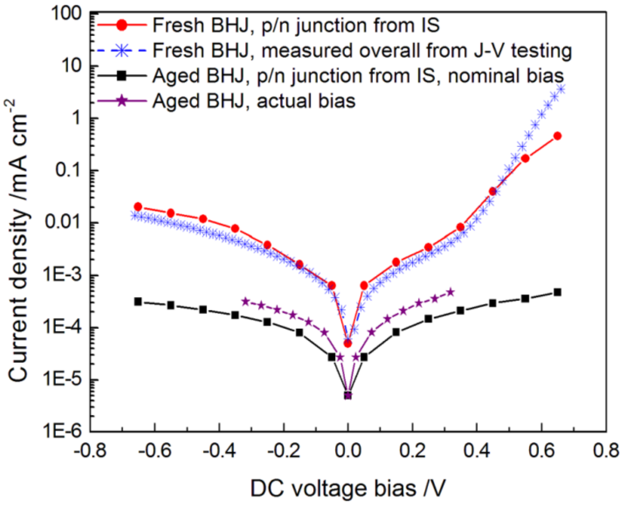

Figure 6.4 Current density versus bias voltage (J-V) curves, obtained from the semicircle representing the p/n junction, for both the fresh and aged devices, using impedance spectroscopy (IS). The extracted results are in good agreement with that obtained from the direct J-V testing of the whole device.

resistor and capacitor combinations. Only one of the capacitance values was found to follow a similar p/n junction pattern (**Figure 6.3**), although the bias voltage needed to be corrected to about ½, due to the voltage drop in the new interface (cf. actual bias vs. nominal bias in **Figure 6.3**). However, the capacitance was one order of magnitude smaller than that of the fresh device, as will be discussed further below. It implies that the p/n junction made of P3HT and PCBM still exists in the degraded OPV device, even though the related p/n interface was changed completely from the fresh device.

To figure out the causes for the above interface change, we also analyzed the J-V characteristics across the p/n junction in both fresh and aged devices in the dark, to rule out the further complication from illumination. This J-V is very different from the commonly obtained J-V curve, which only gives the information of all the interfaces combined. The individual interface information has to be separated from the overall response. Therefore, the R obtained from the semicircle representing the p/n junction was utilized to extract the current density under various DC bias via $dV/dJ=R(V)$. The method was first applied to the fresh device, where there was only one semicircle for the p/n junction. The extracted J-V was consistent with that obtained from the direct J-V test of the whole device (**Figure 6.4**), suggesting that the J-V curve isolation by the impedance spectra was indeed achieved. Therefore, for the aged device involving several interfaces and multiple semicircles, J-V of each interface can now be obtained by extracting the R from respective semicircle, and V has also been corrected for individual interface (cf. actual bias vs. nominal bias in **Figure 6.4**). The extracted applied voltage across the p/n junction gives an external electric field, which is distinguishable from the internal electric field testing between the p/n junction.[27] From the results, the fresh OPV showed good rectifying property by the resistance which was 100-1000 times smaller under forward bias than under reverse bias, whereas the rectifying behavior was non-evident in the aged device. Meanwhile, the resistance was approximately 100 times larger for the aged device at each bias voltage.

Together with the J-V curves, the capacitance results suggested that, a major part of the OPV degradation comes from the P3HT/PCBM junction. The decrease in capacitance may be related to the morphological changes of the photoactive layer in the nanoscale. Although the changes from the active layer, such as the domain size distribution and chemical composition, can be assessed by grazing incidence X-ray scattering measurement [28] and 1H spin diffusion NMR spectroscopy [29], the winding interface of p/n junction from this 3D structure could hardly be obtained, and special preparation methods have to be carried out to remove the electrodes. Here, from the capacitance drop, it can be deduced that the nanoscale interpenetrating morphology could no longer be maintained, and the interfacial area of p/n junction was expected to decrease, because both the junction and diffusion capacitances are proportional to the interfacial area [25]. It also provides additional information of overall morphological change, to the local observation of no obvious phase segregation upon exposure to air [30]. In the meantime, some of the degraded organic semiconductors were found to act as traps for holes or electrons [31], such as the oxidized PCBM which had deeper LUMO levels than pristine PCBM [5], all leading to the increased resistance in the degraded device.

Repeating the same analysis for the second semicircle appeared in the aged device, we obtained the plots of capacitance and resistance versus DC bias voltage (**Figure 6.5**). Different from the rectifying properties of a p/n junction, the extracted J-V curve was linear, and the resistance, which is the slope of the curve, stayed almost the same from nominal bias of -0.6 V to 0.6 V, both of which indicated that the second interface is purely resistive. However, it was quite a surprise that the capacitance showed a symmetrical shape centered at zero bias, with the values dropping by 75% under increased voltage in both directions.

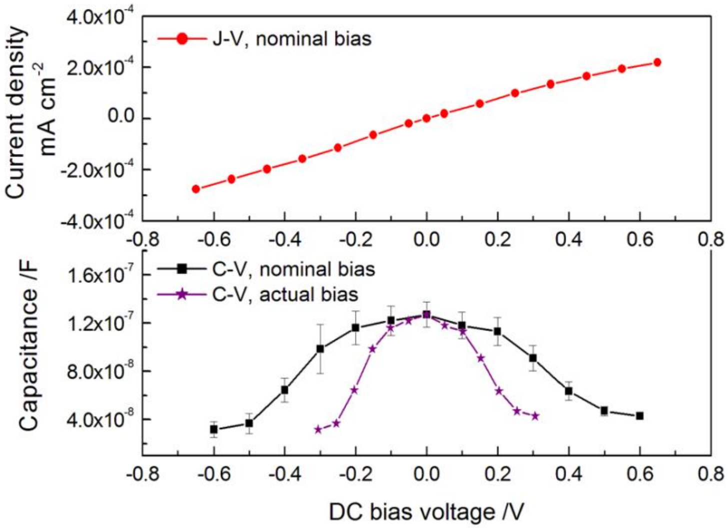

Figure 6.5 Current density versus bias voltage (upper) and capacitance versus bias voltage curves (lower), obtained from the second semicircle in the impedance spectrum of the aged device under 1 atm.

In order to understand the nature of the second interface, it is now necessary to figure out why and how the capacitance decreases by increasing the DC bias. Since this is no longer a part of the BHJ, only a parallel-plate capacitor is anticipated here. And the capacitance is determined by the nominal device area, separation and dielectric constant of the dielectric material in between. Because both the area and separation are fixed by the geometry, it is unlikely to have a change of 75% by applying DC voltage only. Therefore, the only possible reason for such a drop, must be the variation of the dielectric constant under applied DC voltage. On the other hand, the symmetrically decreasing dielectric constant-voltage curve could be found in ferroelectric materials, such as barium titanate [32], due to the permanent dipole moment drop caused by a strong electric field. This brings our attention to the degradation product of metal electrode used in the device, such as Al_2O_3, since Al electrode may react with the ambient to produce Al_2O_3, which changes the interface between the organic semiconductor and metal electrode [4]. The Al_2O_3 should be about 15 nm thick, estimated from the capacitance value. When nominal DC bias of ±0.6 V was applied, the electric field strength reaches approximately $2*10^7$ V m^{-1}. This DC electric field was strong enough to affect the induced dipole moment. Therefore, a part of the dipoles in Al_2O_3 may be unable to flip following the AC impedance test. Obviously, the impact becomes higher as the applied DC voltage increases, which explains why the dielectric constant, and thus the capacitance decrease with the DC voltage increase.

Therefore, the p/n semiconductor and semiconductor/metal interfaces in OPV devices were successfully separated by two distinguishable semicircles. One of the semicircles is linked to the p/n junction formed by P3HT:PCBM, and the other represented the interface between PCBM and metal electrode, involving the metal oxide in an aged device. The results confirmed that, more than one degradation process took place simultaneously at individual interfaces.

To conclude, multiple interface degradation in P3HT/PCBM based OPVs was investigated simultaneously, by DC biased AC impedance spectroscopy, under controlled environment, varying from vacuum to ambient. By the impedance spectra showing two distinguishable semicircles, the p/n semiconductor and semiconductor/metal interfaces in the OPV have been separated without breaking the device. The respective degradation behavior was also revealed by the J-V curve of the p/n junction, isolated from the multiple interfaces, and interfacial capacitance versus voltage plot, obtained under scanned DC bias. We completed for the 1st time here, the degradation study from the birth of a device, without breaking vacuum, all the way to the complete failure. This has led to the observations never reported before, which involve drastic changes of organic solar cells when we purposely admitted trace amount of air, to simulate the environment of a glove box. It is thus clear that the degradation starts at the initial stage even within a glove box. This precluded any similar assessment outside the vacuum by the contrast which has yet to be reported. The degradation of p/n interface was mainly attributed to the deteriorated active layer morphology and oxidized organic semiconductors, whereas the degradation product, a metal oxide, was found to change the interface between the organic semiconductor and metal electrode.

ACKNOWLEDGMENT

The authors acknowledge the financial support of Natural Science and Engineering Research Council of Canada.

REFERENCES

[1] N. S. Sariciftci, L. Smilowitz, A. J. Heeger, and F. Wudl, Science **258**, 1474 (1992).

[2] G. Yu, J. Gao, J. C. Hummelen, F. Wudl, and Alan J. Heeger, Science **270**, 1789 (1995).

[3] Z. He, C. Zhong, S. Su, M. Xu, H. Wu, and Y. Cao, Nat. Photon. **6**, 591 (2012).

[4] M. Jørgensen, K. Norrman, and F. C. Krebs, Sol. Energy Mater. Sol. Cells **92**, 686 (2008).

[5] M. O. Reese, A. M. Nardes, B. L. Rupert, R. E. Larsen, D. C. Olson, M. T. Lloyd, S. E. Shaheen, D. S. Ginley, G. Rumbles, and N. Kopidakis, Adv. Funct. Mater. **20**, 3476 (2010).

[6] A. Kumar, R. Devine, C. Mayberry, B. Lei, G. Li, and Y. Yang, Adv. Funct. Mater. **20**, 2729 (2010).

[7] X. Wang, C. X. Zhao, G. Xu, Z.-K. Chen, and F. Zhu, Sol. Energy Mater. Sol. Cells **104**, 1 (2012).

[8] F. C. Krebs and K. Norrman, Prog. Photovoltaics **15**, 697 (2007).

[9] K. Kawano, R. Pacios, D. Poplavskyy, J. Nelson, D. D. C. Bradley, and J. R. Durrant, Sol. Energy Mater. Sol. Cells **90**, 3520 (2006).

[10] S. Bertho, I. Haeldermans, A. Swinnen, W. Moons, T. Martens, L. Lutsen, D. Vanderzande, J. Manca, A. Senes, and A. Bonfiglio, Sol. Energy Mater. Sol. Cells **91**, 385 (2007).

[11] B. Paci, A. Generosi, V. Rossi Albertini, R. Generosi, P. Perfetti, R. de Bettignies, and C. Sentein, J. Phys. Chem. C. **112**, 9931 (2008).

[12] H. Neugebauer, C. Brabec, J. C. Hummelen, and N. S. Sariciftci, Sol. Energy Mater. Sol. Cells **61**, 35 (2000).

[13] C. L. Huisman, A. Goossens, and J. Schoonman, J. Phys. Chem. B **106**, 10578 (2002).

[14] K. Kawano and C. Adachi, Adv. Funct. Mater. **19**, 3934 (2009).

[15] M. Logdlund and J. L. Bredas, J. Chem. Phys. **101**, 4357 (1994).

[16] M. O. Reese, A. J. Morfa, M. S. White, N. Kopidakis, S. E. Shaheen, G. Rumbles, and D. S. Ginley, Sol. Energy Mater. Sol. Cells **92**, 746 (2008).

[17] A. Moujoud, S. H. Oh, J. J. Hye, and H. J. Kim, Sol. Energy Mater. Sol. Cells **95**, 1037 (2011).

[18] J. W. Jung, J. W. Jo, and W. H. Jo, Adv. Mater. **23**, 1782 (2011).

[19] G. Garcia-Belmonte, A. Munar, E. M. Barea, J. Bisquert, I. Ugarte, and R. Pacios, Org. Electron. **9**, 847 (2008).

[20] J. Lorrmann, B. H. Badada, O. Inganas, V. Dyakonov, and C. Deibel, J. Appl. Phys. **108**, 113705 (2010).

[21] A. Guerrero, P. P. Boix, L. F. Marchesi, T. Ripolles-Sanchis, E. C. Pereira, and G. Garcia-Belmonte, Sol. Energy Mater. Sol. Cells **100**, 185 (2012).

[22] J. R. Macdonald, *Impedance Spectroscopy-Emphasizing Solid Materials and Systems*. (Wiley-Interscience, New York, 1987).

[23] K. Norrman, M. V. Madsen, S. A. Gevorgyan, and F. C. Krebs, J. Am. Chem. Soc. **132**, 16883 (2010).

[24] J. W. Nilsson and S. A. Riedel, *Electric Circuits*, 8 ed. (Prentice Hall, New York, 2008).

[25] B. Streetman and S. K. Banerjee, *Solid state electronic devices*, 6 ed. (Pearson Prentice-Hall, 2009).

[26] S. Dimitrijev, *Principles of semiconductor devices*, 2 ed. (Oxford Univ. Press, New York, 2011).

[27] R. I. Gearba, T. Mills, J. Morris, R. Pindak, C. T. Black, and X. Zhu, Adv. Funct. Mater. **21**, 2666 (2011).

[28] E. Verploegen, R. Mondal, C. J. Bettinger, S. Sok, M. F. Toney, and Z. Bao, Adv. Funct. Mater. **20**, 3519 (2010).

[29] R. C. Nieuwendaal, H. W. Ro, D. S. Germack, R. J. Kline, M. F. Toney, C. K. Chan, A. Agrawal, D. Gundlach, D. L. VanderHart, and D. M. Delongchamp, Adv. Funct. Mater. **22**, 1255 (2012).

[30] M. T. Lloyd, D. C. Olson, P. Lu, E. Fang, D. L. Moore, M. S. White, M. O. Reese, D. S. Ginley, and J. W. P. Hsu, J. Mater. Chem. **19**, 7638 (2009).

[31] B. A. Gregg, Soft Matter 5, 2985 (2009).

[32] S. Roberts, Ph.D. Thesis, Massachusetts Institute of Technology, 1946.

Chapter 7. INVESTIGATING THE DEVICE PHYSICS

7.1 INTRODUCTION

As a promising new technology, OPV have been a focal point in recent years. The energy efficiency has been improved steadily to reach double digits, due largely to the synthesis of new organic semiconductors. The limiting step in organic photovoltaics has been changed from the exciton diffusion length in the bilayer heterojunctions, to the charge separation process in the BHJs. Therefore, it becomes one of the remaining challenges to explore the device physics, in order to search for better material systems of more efficient charge separation at the donor/acceptor interface, instead of empirical trial-and-error.

7.2 PAPER 4: SPACE CHARGES AND DIPOLES (SUBMITTED)

Space charges and dipoles in bilayer and bulk heterojunctions of organic photovoltaics

Cindy X. Zhao, Lucy L. Deng, and Gu Xu*

Materials Science and Engineering, McMaster University

1280 Main Street West, Hamilton, Ontario, L8S4L7, Canada

The dramatic contrast in device physics between the bilayer and bulk heterojunctions in organic photovoltaics has been investigated by capacitance measurements in vacuum, necessary for the accuracy. The donor/acceptor interface in the bilayer devices was confirmed to be larger than the nominal device area, due to the thermal annealing. In contrast, bulk heterojunctions produced higher overall capacitance, resulting in a puzzling space charge density, when the Schottky junction is considered only. The correct answer is obtained by separating the measured capacitance into two parallel components, one from the space charge of the Schottky junction, and the other from the dark dipoles formed spontaneously across the donor/acceptor interface.

(Received XX July 2013; published XX XX 2013)

As a promising new technology, organic photovoltaics (OPV) have been a focal point in recent years. The energy efficiency has been improved steadily to reach double digits, due largely to the synthesis of new chemicals[1]. Despite the development, a considerable gap still exists when compared with silicon based solar cells. One major cause of such a gap is the localized photo-induced exciton and much shorter diffusion length within OPVs, which is not easily overcome by the chemistry [2-5], thus reducing the "effective volume". This led to the development of bulk heterojunctions (BHJ) (**Figure 7.1A**), to increase the junction areas between electronic donors and acceptors (D/A) by an interpenetrating interface, so that excitons are never too far away from the junction [6-8]. The limiting step in BHJ devices has thus become the separation of the photo-generated excitons, when the electrons and holes must overcome the binding energy caused by the Coulombic attraction. Due to the smaller dielectric constant and shorter electron-hole distance in organic semiconductors, this binding energy is on the order of 1eV, hundred times larger than that of their inorganic counterparts, and much higher than the thermal energy of 0.025eV at room temperature [9]. Therefore, it becomes one of the remaining challenges to explore the device physics, in order to search for better material systems of more efficient charge separation at D/A interface, instead of empirical trial-and-error.

As the predecessor of BHJs, bilayer OPVs were first developed in 1986, and achieved a power conversion efficiency of about 1% [10]; however, these devices are exciton diffusion length limited, as mentioned above, and only a small fraction of excitons near the D/A interface can be separated. They are otherwise similar to a p/n junction with band bending between the D/A interface [11, 12], where the junction area can be tuned by morphological variation. In contrast, the charge separation process in BHJs remains controversial. While some experiments indicate a similar mechanism to the bilayer devices, where excitons generated in the bulk of polymers diffuse to the D/A interface, followed by electrons captured by the acceptor molecules and holes staying in the polymer donor [13]; others show an energy transfer from polymers to fullerenes, such that excitons created in the polymers are first transferred into fullerenes, and then holes returned into the polymers via D/A interface [14]. More dramatically, in a recent model the D/A interface in BHJ is treated as a single piece of p-doped semiconductor. In the early version of this model, the LUMO and HOMO levels of donor and acceptor are tilted due to the different work functions of metal electrodes. The resulting electric field across the blend drives the electrons and holes in the opposite directions [5]. Since the donor and acceptor materials are in fact separated from each other with an average domain size of 10 nm, this model is actually equivalent to the bilayer model on that scale. However, the model cannot explain the charge distribution in the polymer blend due to the tilted bands of a constant slope. In a more acceptable version, the BHJ devices behave like a Schottky junction, formed between the mixture of donor and acceptor, and the metal electrode. The band bending and space charges are proposed to be located near the electrode, thus the interfacial area is fixed to be the nominal area of the electrode. It was believed that, the quasi-free carriers near the metal electrode can strongly shield the Coulombic binding, thereby enhancing the charge separation [15].

At the first glance, the above model has difficulty explaining the D/A polymer blend as a single piece of polymer. Considering both the phase segregation in the opposite directions [8, 16-18], and the charges traveling only through the respective domains, the spatially separated D/A cannot simply be treated as a uniform mixture. In addition, it is a little uncertain about where the charges are produced, especially under the dark condition, in the absence of photo-oxidation process. Therefore, the question remains, whether the enlarged D/A interface formed by bicontinuous interpenetration, can still be regarded a p/n junction, or has to be treated as a single polymer blend. More recently, models involving dipoles were introduced, to explain the charge separation at the D/A interface [19]. The existence of dark dipoles has also been probed experimentally [20]. A partial charge separation occurring at the D/A interface in the dark would create an array of discrete dipoles distributed along the interface, which reduce the recombination rate of electron-hole pairs [20], and are speculated to be the source of the divergent dielectric constant at the interface [21]. However, it is not clear “how important it is to consider dipoles as discrete species equidistantly distributed along the D/A interface” [21]. Therefore, it is necessary to explore further the relationship among the existing models, and in particular to confirm location of space charges and the existence of the dipoles.

In this report, we try to verify the dramatic contrast in device physics between the bilayer and BHJ structures, and to explore the existence of space charges and dipoles in BHJ devices, through “in situ” capacitance measurements without breaking the vacuum after fabrication. In particular, we confirmed first the current understanding of bilayer devices, in which the D/A interface is the dominant junction, with its area variation reflected by the capacitance value. In contrast, we found the overall capacitance in the BHJ, which has a fixed nominal device area, is even larger than that from the bilayer devices. It results in a puzzling space charge density, if the Schottky junction is considered only. Finally, the puzzle is resolved by introducing the suggested spontaneous formation of the dipoles at the D/A interface, leading to the dielectric relaxation of the dipoles - overriding the p/n interface, which is found almost everywhere in a BHJ.

The OPVs were fabricated following the standard procedures for P3HT/$PC_{61}BM$ and for PTB7/$PC_{71}BM$ [1] , involving both annealed and non-annealed bilayer, and BHJ architectures (**Figure 7.1B**). The bilayer and BHJ devices became, ITO/PEDOT:PSS /P3HT(20 mg mL^{-1} in DCB)/$PC_{61}BM$ (20 mg mL^{-1} in DCM)/Al; ITO/PEDOT:PSS/P3HT :$PC_{61}BM$(1:1 by weight, 20 mg mL^{-1} in DCB)/Al; ITO/PEDOT:PSS/ PTB7(20 mg mL^{-1} in DCB)/$PC_{71}BM$(20 mg mL^{-1} in DCM)/Al; and ITO/PEDOT:PSS/ PTB7:$PC_{71}BM$(1:1.5 by weight, 25 mg mL^{-1} in a mixed solvent of DCB/DIO 97:3 by volume)/Al, respectively. The total thickness of the photoactive layers was 180-200 nm. A 100 nm thick Al electrode was thermally deposited through a shadow mask under a vacuum pressure of 10^{-9} atm, to define the device nominal area of 5×5 mm^2. The interfacial areas between electron donors and acceptors were studied in the dark, by a DC biased AC impedance analyzer (HP4284A), which allows for capacitance measurement via a frequency scan (20-10^6 Hz) under a bias voltage (**Figure 7.2A**). To avoid the possible influence of the ambient, which was indeed found to be the case, the measurement was done right after a

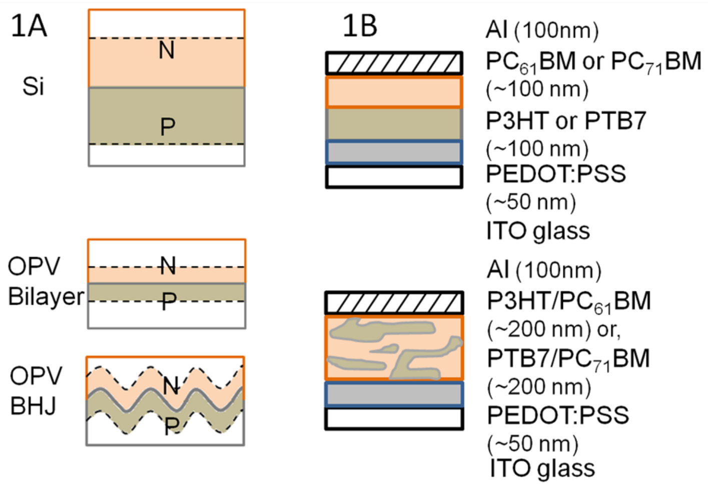

Figure 7.1 Comparison made between bilayer and BHJ structure of organic solar cells. (A) cross-sectional views of silicon solar cells, bilayer and BHJ OPVs, showing the "effective volume" is reduced in OPVs due to the shorter exciton diffusion length, but can be improved by interfacial area increase in a BHJ. (B) device structures of bilayer and BHJ OPVs, involving a number of layers of materials (from 1-Material Co.), with a nominal surface area of 5 x 5 mm^2.

device was fabricated, without breaking the vacuum, using pre-wired electric connections before electrode evaporation via vacuum feed-through (**Figure 7.2B**).

To verify the necessity of vacuum sealed capacitance measurements, we purposely admitted a small amount of air into the vacuum chamber, to raise the pressure from 10^{-9} to 10^{-5} atm, which simulates the "dry" environment (ppm level of O_2) of a typical glove box, usually employed in OPV fabrication and testing. Within an hour, the impedance data were found to be changed drastically for BHJs (**Figure 7.3**), as well as for bilayer devices. This precludes any similar assessment of junction areas outside the vacuum environment.

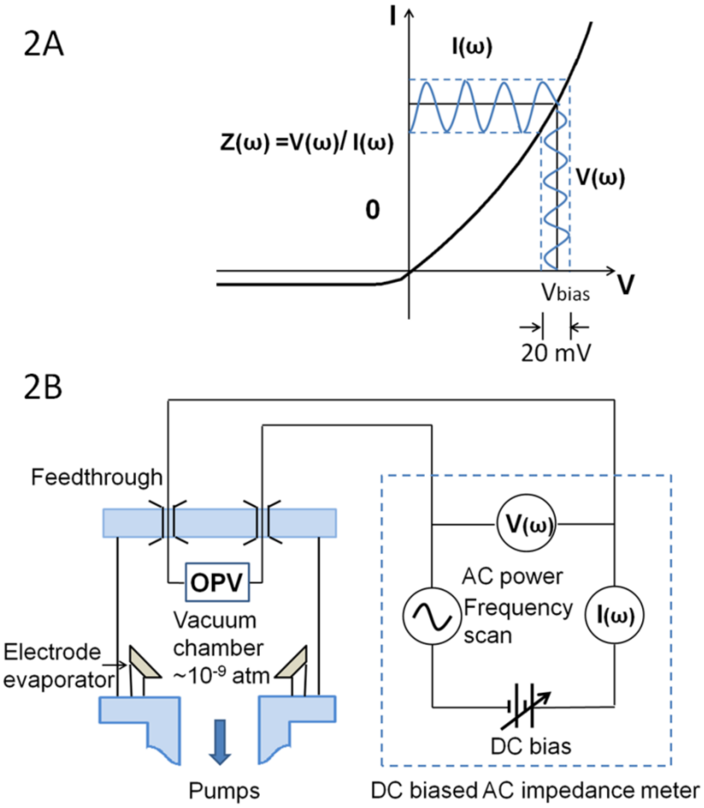

Figure 7.2 Interfacial areas of BHJ and bilayer OPVs, to be measured by DC biased AC impedance analyzer in vacuum environment. (A) DC biased AC impedance measurement, showing an AC voltage of about 20 mV oscillates in the vicinity of a DC bias, on the current-voltage curve of an OPV, where ω = 2π*frequency. (B) The experimental setup, involving a vacuum system for the electrode evaporation, as well as the "in situ" impedance measurement, performed without breaking the vacuum seal, found to be necessary to obtain reliable data.

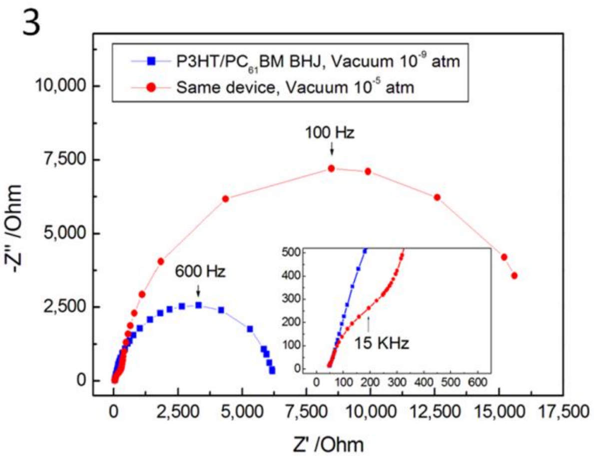

Figure 7.3 Dramatic changes in impedance data, within 1h after the introduction of trace amount of air, equivalent to that found in a dry glove box with ppm level of oxygen.

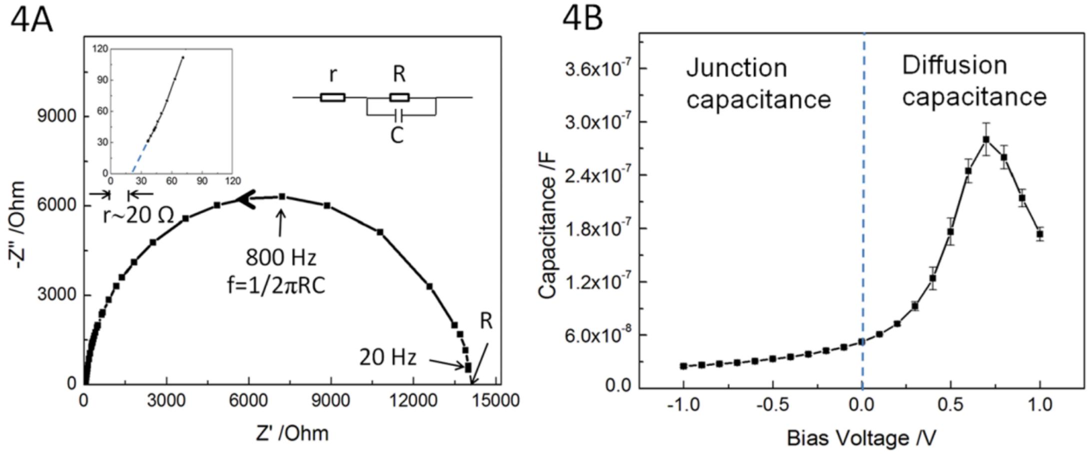

Figure 7.4 Capacitances obtained by the measured impedance data. (**A**) Nyquist plot of the impedance data, averaged over 3-5 measurements, for a particular bias voltage, which can be simulated by a resistor R and a capacitor C in parallel (**inset**). A smaller resistor responsible for the connection can also be found near the origin (**inset**). (**B**) Capacitance versus bias voltage of a bilayer device, showing the negative side related to the junction capacitor, and the positive side to the diffusion capacitor.

The impedance data under each bias voltage were presented by Nyquist plot [22], which shows unanimously a semicircle along the real and negative imaginary impedance axes, typical for a capacitor and resistor combination (**Figure 7.4A, inset**).While the resistance, R, can be extracted from the real axis, the capacitance, C, is obtained from the top frequency, f, using $RC = (2\pi f)^{-1}$ [23]. The capacitance versus bias voltage can thus be plotted (**Figure 7.4B**).

The curves obtained from the bilayer structures look similar to a general pattern of a p/n junction with band bending between D/A interface [24], which is in good agreement with the current understanding of bilayer OPVs showing the space charge built-up around the heterojunction [25]. Since the positive bias side is dominated by the diffusion capacitance arising from the voltage lagging behind the current, and the negative bias side by the junction capacitance caused by the space charges in the depletion zone [24, 26], we are able to track the junction area variation, by plotting the capacitance values of both non-annealed and annealed bilayer devices under negative bias voltages (**Figure 7.5**).

To obtain the junction areas between D/A interface, we have to estimate first the charge densities. The capacitance data (C) under each bias voltage (V) were analyzed by C^{-2} versus V plot, where the values of built-in voltage (V_{bi}) can be determined by the voltage corresponding to the maximum of capacitance equals the flat-band condition. The charge densities (N) of P3HT/PC$_{61}$BM and PTB7/PC$_{71}$BM can be obtained from depletion zone width (d) as a function of bias. When the bias (V) is set to the more negative values, the d will become larger, until it is similar to the device thickness, where

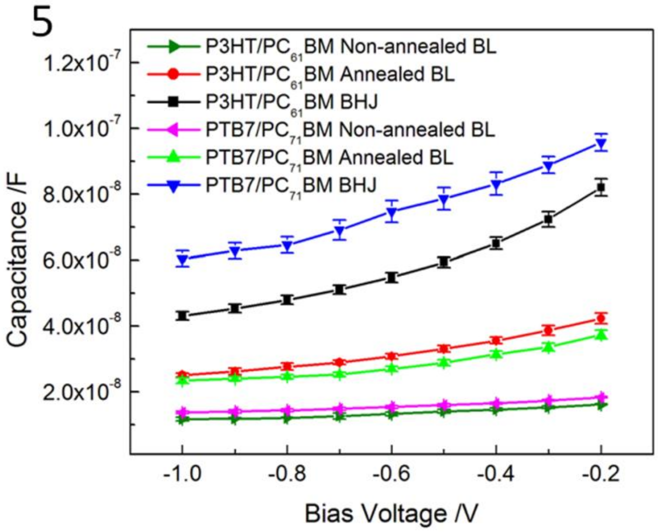

Figure 7.5 Capacitances of various bilayer (BL) and BHJ devices, obtained by the measured impedance data.

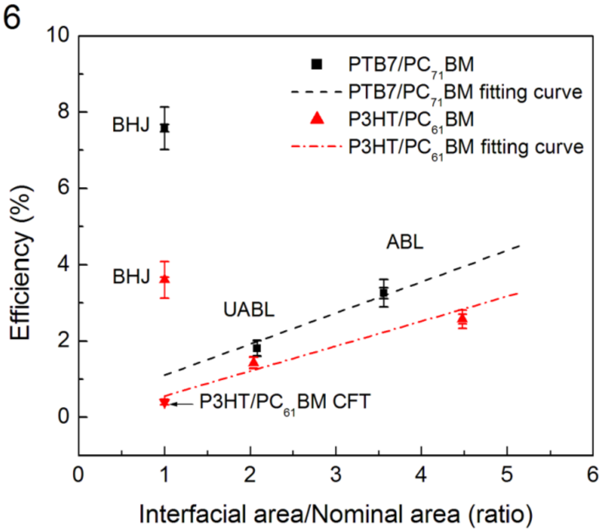

Figure 7.6 A summary curve for the energy efficiency improvement of OPVs, versus their junction area increases, using the axes normalized by the nominal area of the devices, 0.25cm^2, where NABL stands for non-annealed bilayer devices, and ABL for annealed bilayer, respectively.

the capacitance no longer follows $(V_{bi}-V)^{-1/2}$. In other words, whenever we find the capacitance-bias voltage deviating away from the $(V_{bi}-V)^{-1/2}$, d must be approaching the device thickness (about 180 nm). In our case, this happens around V = -3.0 volts for non-annealed bilayer P3HT/PC_{61}BM devices, as was also found by others [27]. For a p/n junction [24],

$$d = [2\varepsilon_0\varepsilon_r(V_{bi}-V)(N_d^{-1}+N_a^{-1})/q]^{1/2} = [2\varepsilon_0\varepsilon_r(V_{bi}-V)/qN]^{1/2} \quad \textbf{(1)}$$

where $N^{-1} \equiv N_d^{-1}+ N_a^{-1}$, with q being the elementary charge, N_a the acceptor charge density, N_d the donor charge density, ε_0 the vacuum dielectric constant, and ε_r the relative dielectric constant (e.g., $\varepsilon_r = 3.0$ for P3HT/PC_{61}BM [28], and 3.5 for PTB7/PC_{71}BM [29]). Thus N is found to be $3.7*10^{+16}cm^{-3}$. The same method can be applied to the bilayer PTB7 system, where charge density N is found to be about $4.8*10^{+16}$ cm^{-3}. Employing the charge density, the junction area (A) between D/A interface in bilayer structures can now be calculated by [24]:

$$A=Cd/\varepsilon_0\varepsilon_r=C[2(V_{bi}-V)/ \varepsilon_0\varepsilon_r qN]^{1/2} \quad \textbf{(2)}$$

In addition, a second method was applied to further confirm the above results, where the interfacial area was estimated to be $[2/ (\Delta\, \varepsilon_0\varepsilon_r qN)]^{1/2}$ [24], with Δ being the absolute value of the slope in the C^{-2} vs. V curve at $V< V_{bi}$. And results were found to be consistent with one another. Compared with the obtained junction areas for D/A interface, the energy efficiency, and I-V characteristics (**Table 7.1**), the junction areas of bilayer structures, after thermal annealing, were found to increase from 0.578 to 0.829 cm^2, and 0.482 to 0.884 cm^2 in P3HT and PTB7 systems, which are matched by similar increases in energy

Table 7.1 List of open-circuit voltage, short-circuit current, fill-factor and energy efficiency of each OPV device, measured outside the vacuum chamber, using a regular I-V setup and AM1.5G solar simulator. The capacitances were taken at -1 volt bias to reduce the influence of other factors. The built-in voltages (V$_{bi}$) and absolute interfacial areas were calculated from the C^{-2} vs. V plots. All the data were averaged over about 5 devices.

	Voc (V)	Jsc (mAcm^{-2})	Fill Factor	PCE (%)	Capacitance (F)	V$_{bi}$ (V)	Interfacial Area[a] (cm^2)
P3HT/PC$_{61}$BM Non-annealed BL	0.50 ±0.010	5.65 ±0.187	0.51 ±0.020	1.43 ±0.147	1.14E^{-8} ±5.80E^{-10}	0.52 ±0.02	0.51 ±0.04
P3HT/PC$_{61}$BM Annealed BL	0.53 ±0.009	8.43 ±0.155	0.58 ±0.039	2.58 ±0.124	2.51E^{-8} ±6.17E^{-10}	0.53 ±0.02	1.12 ±0.06
P3HT/PC$_{61}$BM BHJ	0.55 ±0.005	9.62 ±0.234	0.68 ±0.007	3.61 ±0.070	4.30E^{-8} ±1.26E^{-9}	0.55 ±0.01	0.25
PTB7/PC$_{71}$BM Non-annealed BL	0.66 ±0.012	5.05 ±0.247	0.54 ±0.037	1.81 ±0.214	1.36E^{-8} ±3.63E^{-10}	0.66 ±0.01	0.52 ±0.05
PTB7/PC$_{71}$BM Annealed BL	0.68 ±0.006	7.71 ±0.208	0.61 ±0.015	3.26 ±0.143	2.34E^{-8} ±8.58E^{-10}	0.69 ±0.02	0.89 ±0.09
PTB7/PC$_{71}$BM BHJ	0.73 ±0.003	14.99 ±0.270	0.70 ±0.008	7.58 ±0.095	6.04E^{-8} ±2.43E^{-10}	0.72 ±0.02	0.25

[a] Nominal area of the devices =0.25 cm^2

efficiency of 1.7 and 1.8 times, respectively. The bilayer devices are having 2-3.5 times the interfacial areas of the nominal electrode area, depending on the degree of annealing, confirming that it is indeed difficult to obtain a perfect bilayer device [30]. It can be concluded that in both material systems, thermal annealing can enlarge the D/A interface by inter-diffusion at elevated temperature [31]. This interfacial area calculation method was also verified by the efficiency and area data, from a well-defined bilayer solar cell prepared by the contact film-transfer method [30]. The efficiency data falls onto the fitting curve of interfacial area ratio versus efficiency (**Figure 7.6**), when the interfacial area is about the same as the nominal electrode area.

In the case of BHJs, however, the model based on the Schottky junction formed between a mixture and metal electrode seems more popular [28], where the junction area equals the nominal area of the electrodes. To compare with the bilayer devices, the junction capacitance data at negative bias voltage were also plotted in the same figure, which show higher values. Following equation (2), where the left side becomes the nominal area, the charge densities were calculated to be $2.1*10^{+18}$ cm^{-3} and $4.0*10^{+18}$ cm^{-3} for P3HT and PTB7 BHJs, respectively. They are two orders of magnitude higher than that of the bilayer devices. This is intriguing, because they are made by the same materials, and the power conversion efficiencies (**Table 7.1**) of the bilayer and BHJs structures are within the same order of magnitude, typical for P3HT and PTB7 based devices. This is also puzzling, since such a high value of charge densities would lead to a very small depletion zone width, which can hardly be accommodated by the BHJ structures in reality: unlike the bilayer structures, the band bending and the space charges in a BHJ are supposed to be located near the metal electrode, and almost no space charge is allowed at the D/A interface. Although a weak band bending between donor and acceptor may still be possible, as described by C. Deibel et al [25], indicating that the space charge may exist locally near the D/A interface. However, by then the junction area would be much larger than the assumed the nominal area of the metal electrode.

To resolve the puzzle, it is helpful to re-examine all the assumptions involved so far. Obviously, a higher space charge density (or a smaller d) is not the only possibility to raise the capacitance, which may also be contributed by other factors. Besides the space charges, the interfacial dipoles proposed recently [19] may also increase the overall capacitance. Models involving dipoles were first introduced to explain the charge separation at the D/A interface [19]. The existence of dark dipoles has also been probed experimentally [20], with the negative charges of the dipoles situated on the acceptor side of the interface and the positive charges of dipoles on the polymer chain nearest to the interface. A partial charge separation occurring at the D/A interface in the dark will create an array of these discrete dipoles distributed along the interface, which reduce the recombination rate of electron-hole pairs [20]. These dipoles can be the origin of a much larger dielectric constant, resulting in a higher capacitance value, due to the dielectric relaxation, where dipoles can be reoriented and/or deformed by an AC bias. Although the reported values of dielectric constant are about 2-4, they were measured from bulk organic semiconductors, and are not necessarily valid in the vicinity of the interface between two organic materials. In fact, in some extreme cases, the dielectric constant in a mixture of two materials may diverge in the vicinity of the interface [32-34].

Therefore, the measured capacitance of a BHJ seems to be contributed by two parallel components, one from the space charge of the proposed Schottky junction between the semiconductor and metal electrode, and the other from the dipoles presumably formed spontaneously across the D/A interface. To estimate the values of each, we followed the same strategy used above for the bilayer devices, to first obtain the depletion zone widths of the BHJs, which were found to be 126nm and 124nm for P3HT and PTB7 devices, respectively. The corresponding capacitance values, which are attributed to the space charges of the Schottky barriers, viz., ε_0*(bulk ε_r)*(nominal area)*(depletion zone width)$^{-1}$, were calculated to be $5.27*10^{-9}$ and $6.24*10^{-9}$ F for P3HT and PTB7 devices, respectively. The balances are, evidently, attributed to the dipole relaxation, which are actually 7.2 and 8.6 times larger ($3.77*10^{-8}$ and $5.38*10^{-8}$ F), than that of the junction capacitances of the two types. Finally, much more reasonable values of space charge densities are obtained from the junction capacitances alone, using equation (2), which are $3.5*10^{+16}$ cm^{-3}, and $4.3*10^{+16}$ cm^{-3} for the two types, respectively, almost identical to those reported before. For the dielectric constant of the organic semiconductors, it remains to be about 3 for the bulk, except for the D/A interface, where it is possible to reach much higher values, which is responsible for the balance capacitance discussed here. The imaginary part of this dielectric constant, related to the loss tangent of the dipolar relaxation, will be combined into the real part of the overall impedance: $Z = [j\omega C+R^{-1}]^{-1}$ [22], where ω is the angular frequency of an AC field, and R represents the DC resistance of the device, which is dominanting due to its smaller values ($\approx 10^{+4}$ ohm) than that from the dielectric loss. It may be debatable to ascribe their coverage of the entire thickness rather than within the depletion zone, due to the spontaneous formation of dark dipoles overriding the developed interface of the BHJs, which are found everywhere within the BHJ structure by the 3D interpenetrating D/A network. Nevertheless, a high dielectric constant in the vicinity of the internal D/A interface helps to eliminate the huge Coulombic energy barrier in the charge separation process.

To summarize, by “in situ” impedance measurements without breaking the vacuum for the needed accuracy, we verified the dramatic contrast in device physics between the bilayer and BHJ structures. We confirmed the current understanding of bilayer devices, in which the D/A interface is the dominant junction, with its area variation reflected by the capacitance data. In contrast, we found the overall capacitance in the BHJ, which has a fixed nominal device area, results in a puzzling space charge density. To resolve the puzzle we must partition the capacitance into two parallel components, one from the space charge of the proposed Schottky junction between the semiconductor and metal electrode, and the other from the dipoles assumed to be formed spontaneously across the D/A interface. The two capacitance values can be estimated, with the dipole contribution found to be much larger. As a result, a higher capacitance, and the resulting puzzling charge density, obtained from BHJs can now be explained by the dielectric relaxation of the dipoles - overriding the p/n interface of the BHJ, which exists almost everywhere within the BHJ structure.

Acknowledgements

The authors acknowledge the financial support of Natural Science and Engineering Research Council of Canada. They are also grateful to Dr. Beng Ong, Dr. Zhikuan Chen, Dr. Xizu Wang and Dr. Wenjin Zeng of the Institute of Materials Research and Engineering of Singapore for their kind discussion.

* *Corresponding author:* E-mail: xugu@mcmaster.ca

REFERENCES

[1] Z. He, C. Zhong, S. Su, M. Xu, H. Wu, and Y. Cao, Nat. Photon. **6**, 591 (2012).

[2] A. Haugeneder *et al.*, Phys. Rev. B **59**, 15346 (1999).

[3] D. E. Markov, E. Amsterdam, P. W. M. Blom, A. B. Sieval, and J. C. Hummelen, J. Phys. Chem. A **109**, 5266 (2005).

[4] P. W. M. Blom, V. D. Mihailetchi, L. Jan Anton Koster, and D. E. Markov, Adv. Mater. **19**, 1551 (2007).

[5] N. S. Sariciftci and H. Hoppe, J. Mater. Res. **19**, 1924 (2004).

[6] G. Yu, J. Gao, J. C. Hummelen, F. Wudl, and A. J. Heeger, Science **270**, 1789 (1995).

[7] T. L. Benanti and D. Venkataraman, Photosynth. Res. **87**, 73 (2006).

[8] Z. Xu, L.-M. Chen, G. Yang, C.-H. Huang, J. Hou, Y. Wu, G. Li, C.-S. Hsu, and Y. Yang, Adv. Funct. Mater. **19**, 1227 (2009).

[9] E. Silinsch and V. Capek, *Organic Molecular Crystals* (AIP Press, New York, 1994).

[10] C. W. Tang, Appl. Phys. Lett. **48**, 183 (1986).

[11] D. Cheyns, J. Poortmans, P. Heremans, C. Deibel, S. Verlaak, B. P. Rand, and J. Genoe, Phys. Rev. B **77**, 165332 (2008).

[12] Q. Sun, G. Dong, D. Li, L. Duan, L. Wang, and Y. Qiu, Org. Electron. **13**, 3276 (2012).

[13] L. W. Barbour, R. D. Pensack, M. Hegadorn, S. Arzhantsev, and J. B. Asbury, J. Phys. Chem. C. **112**, 3926 (2008).

[14] M. T. Lloyd, Y.-F. Lim, and G. G. Malliaras, Appl. Phys. Lett. **92**, 143308 (2008).

[15] J. Bisquert and G. Garcia-Belmonte, J. Phys. Chem. Lett. **2**, 1950 (2011).

[16] M. Campoy-Quiles, T. Ferenczi, T. Agostinelli, P. G. Etchegoin, Y. Kim, T. D. Anthopoulos, P. N. Stavrinou, D. D. C. Bradley, and J. Nelson, Nat. Mater. **7**, 158 (2008).

[17] Y. Kim *et al.*, ACS Nano **3**, 2557 (2009).

[18] S. S. van Bavel, E. Sourty, G. de With, and J. Loos, Nano. Lett. **9**, 507 (2009).

[19] V. I. Arkhipov, P. Heremans, and H. Bassler, Appl. Phys. Lett. **82**, 4605 (2003).

[20] H. Aarnio, P. Sehati, S. Braun, M. Nyman, M. P. de Jong, M. Fahlman, and R. Österbacka, Adv. Energy Mater. **1**, 792 (2011).

[21] S. D. Baranovskii, M. Wiemer, A. V. Nenashev, F. Jansson, and F. Gebhard, J. Phys. Chem. Lett. **3**, 1214 (2012).

[22] J. R. Macdonald, *Impedance Spectroscopy-Emphasizing Solid Materials and Systems* (Wiley-Interscience, New York, 1987).

[23] J. W. Nilsson and S. A. Riedel, *Electric Circuits* (Prentice Hall, New York, 2008), 8 edn.

[24] B. Streetman and S. K. Banerjee, *Solid state electronic devices* (Pearson Prentice-Hall, 2009), 6 edn.

[25] C. Deibel and V. Dyakonov, Rep. Prog. Phys. **73**, 096401 (2010).

[26] S. Dimitrijev, *Principles of semiconductor devices* (Oxford Univ. Press, New York, 2011), 2 edn.

[27] A. Takshi, A. Dimopoulos, and J. D. Madden, Appl. Phys. Lett. **91**, 083513 (2007).

[28] G. Garcia-Belmonte, A. Munar, E. M. Barea, J. Bisquert, I. Ugarte, and R. Pacios, Org. Electron. **9**, 847 (2008).

[29] H. Zhou, Y. Zhang, J. Seifter, S. D. Collins, C. Luo, G. C. Bazan, T.-Q. Nguyen, and A. J. Heeger, Adv. Mater. (2013).

[30] A. Tada, Y. Geng, Q. Wei, K. Hashimoto, and K. Tajima, Nat. Mater. **10**, 450 (2011).

[31] J. S. Moon, C. J. Takacs, Y. Sun, and A. J. Heeger, Nano. Lett. **11**, 1036 (2011).

[32] V. E. Dubrov, M. E. Levinstein, and M. S. Shur, Sov. Phys. JETP **43**, 1050 (1976).

[33] A. L. Efros and B. I. Shklovskii, Phys. Status Solidi B **76**, 475 (1976).

[34] Y. C. Chou and T.-S. Jaw, Solid State Commun. **1988**, 753 (1988).

Chapter 8. SUMMARY

As a promising new technology, organic photovoltaics (OPVs) have been a hot research topic for the last 10 years. Despite the rapid development, a considerable gap still exists, compared with the inorganic solar cells with average efficiencies of 15% and lifespan of about 20 years. To meet the remaining challenges of low efficiency and short lifetime, the objectives of the research, as well as my Ph.D. study of the last three years have been; a) to further improve the power conversion efficiency of OPVs, b) to elucidate the mechanisms of the improvement, c) to understand the degradation behavior of OPVs, and d) to clarify the controversy of various device physics models developed in the literature. Up to four research publications were completed, which are listed as follows:

a). In an attempt to improve the device performance to meet the commercialization threshold, the ultra-low frequency AC field was first employed, and the resulting devices showed 15% increase in device efficiency, attributed to the optimized morphology and enlarged p/n interface. The method can be incorporated with the commonly used treatments in the fabrication process, which offers an alternative to further enhance the OPV device efficiency.

b). In order to understand the underlying reasons for the efficiency increase, the nanostructure changes in OPVs by AC electric field alignment were investigated using

2D X-ray diffraction. Two distinguishable nanostructures of the polymers were found, in the form of the highly oriented layer and the randomly distributed part, which provided a complete understanding of the OPVs under the AC field alignment. The 3D nanostructures of polymers were not observed by TEM or AFM, although the TEM and AFM are regarded as the most powerful tools in the thin film studies.

c). "In situ" impedance measurements were employed, to track simultaneous degradation of multiple interfaces, and to reveal the individual interface degradation without breaking the device. I completed for the first time here, the degradation study from the birth of a device in vacuum, all the way to the complete failure. This has led to the observations never reported before, which involved drastic changes of OPVs when the trace amount of air was purposely admitted, to simulate the environment of a glove box. It was thus clear that the degradation starts at the initial stage even within a glove box. This precluded any similar assessment outside the vacuum.

d). To clarify the controversy of various device physics models, the dramatic contrast between the bilayer and BHJ devices was investigated by capacitance measurements in vacuum, necessary for the accuracy. The existing models of the BHJs had difficulty explaining the higher overall capacitance, compared with that measured from the bilayer devices. The resulting puzzling charge density was resolved by separating the measured capacitance into two parallel components, one from the space charge of the proposed Schottky junction, and the other from the dark dipoles presumably formed spontaneously across the donor/acceptor interface, which exists almost everywhere within the BHJ structure.

To conclude, during the last 3 years a certain amount of new achievement has been made by my research, including but not limited to: employed the AC electric field for the first time in OPVs, to align the p/n materials for better power conversion efficiency; elucidated the mechanisms for the improvement by the nanostructure assessment; completed for the first time, the simultaneous multiple-interface degradation study from the birth of a device in vacuum, all the way to the complete failure; and more important, clarified the controversy of bilayer and BHJ models, and resolved the higher capacitance in BHJs than that from the bilayer, by introducing the dark dipoles across the donor/acceptor interface.